Mechanics and Dynamics of Cell Adhesion : Experimental Study of the Osteoclasts

Shiqiong Hu

N° d'ordre: 594
N° attribué par la bibliothèque: 2010ENSL594

THESIS

to obtain the degree:

Ph.D of Université de Lyon - École Normale Supérieure de Lyon

Speciality : **Physics**

Laboratoire de Physique
École Doctorale de Physique et d'Astrophysique de Lyon

presented and defended publically on October 29th 2010 by

Shiqiong HU

Mechanics and Dynamics of Cell Adhesion: Experimental Study of the Osteoclasts

---

under the direction of :
Jean-Christophe Géminard, Shude Chen, Xianghui Wang

After recommandation of:

Marc Block	Professor, Institut A. Bonniot, Grenoble	Reviewer
Zoher Guéroui	Chargé de Recherche CNRS, ENS Paris	Reviewer

In front of the jury composed of:

Marc Block	Professor, Institut A. Bonniot, Grenoble	Reviewer
Jean-Christophe Géminard	Chargé de Recherche CNRS, ENS Lyon	PhD advisor
Zoher Guéroui	Chargé de recherche CNRS, ENS Paris	Reviewer
Pierre Jurdic	Directeur de recherche INSERM, ENS Lyon	Examiner
Gladys Massiera	Maître de Conférences, Univ. Montpellier II	Examiner
Xianghui Wang	Assistant Professor, ECNU, Shanghai	PhD advisor

Acknowledgments

I thank you, all the people both in France and China,
who gave me all kind of help and friendship.

I thank you, all the jury members.

I thank you, Jean-Christophe. I was so lucky to study with you,
you taught me such a big thing as science, and at the same time,
you always took care of all the small things and me.
I could not find the sentences to express all what I want to say.
Thank you for everything, Jean-Christophe!

I thank you, Chen Shude, Wang Xianghui and colleagues in Shanghai.
You gave me all the help and feeling as if I were at home.

I thank you, Pierre and all the colleagues from your biology group:
Irma, Romain, Chantal, Marlène, Murty, Elodie, Dan and Anne.
I got biological knowledge, support, and many discussions from you,
moreover I am deeply touched you adopted me in your warm team.

I thank you, all the colleagues in the physics lab of ENS Lyon,
in particular, I thank you, Valérie.
From the scientific discussions, to never-ending manuscript
and rehearsal corrections, from Arles to China, from science to life,
you let me know how to be shining.
I thank you, my very very very good friend, Xiao Tiao!

I thank you, Thierry, Thibaut, Cécile, Mica, Claudia,
Samantha, Germán, Cendrine, Eric, Christophe, Michel,
Patrick, Stéphane, Ramón, Baptiste, Emmanuelle, Olivier,
Nadine, Julie, Denise, Paul, Catherine, Ciccino, Raffaella...

I thank you, my parents and my husband, Ming.
Thank you for staying with me.

Merci à tous !

Contents

List of Figures

Abbreviation

AFM	atomic force microscope
APS	ammonium persulfate
DAPI	diamidino phenylindole
DMEM	Dulbecco's modified eagle's medium
DMSO	dimethyl sulfoxide
ECM	extracellular matrix
EDTA	ethylene diamine tetraacetic acid
F-actin	actin filaments
FACScan	fluorescence-activated cell sorter scan
FBS	fetal bovine serum
FITC	fluorescein isothiocyanate
FRAP	fluorescent recovery after photobleaching
GFP	green fluorescent protein
ITO	indium tin oxide
M-CSF	macrophage colony stimulating factor
MEM	minimum essential medium
PBS	phosphate buffered solution
PFA	paraformaldehyde
RANK-L	receptor activator of nuclear factor B-ligand
RIE	reactive ion etching
rpm	revolutions per minute
SEM	scan electron microscopy
TEMED	tetramethylethylenediamine
TIRF	total internal reflection
WASP	Wiskott-Aldrich syndrome protein
WIP	WASP Interacting Protein
ZrO_2	zirconium oxide
3D	three-dimensional

Chapter 1

Introduction

Contents

1.1 Foreword

In this study, we focus on one of the major components of an eukaryotic cell[1]: Actin. This protein plays an important role in many cellular processes. In particular, it maintains the cell shape and, by constant destructuration and restructuration, enables cell motility. In spite of a large number of studies, many questions remain about the structure, dynamics and role of actin. In this thesis, we will focus on the dynamics of actin-rich structures, the podosomes, present in one type of bone cells: the osteoclasts.

This work is the result of a co-supervision between Laboratoire de Physique, Ecole Normale Supérieure (ENS) de Lyon and State Key Laboratory of Precision Spectroscopy, East China Normal University (ECNU) of Shanghai. It was based on a continuous collaboration with Pierre JURDIC, from Institut de Génomique Fonctionnelle de Lyon (IGFL), who provided knowledge and support in the biological field. Almost all the biological experiments were performed at IGFL, Ecole Normale Supérieure de Lyon.

In this introductory chapter, we first describe the cell structure and processes involved in the cell motility (section 1.2). In the second section (1.3), we present the cell adhesion structures. Finally (section 1.4), we introduce the osteoclasts, and explain the importance of the actin organization in such cells.

1.2 Cell structure and motility

1.2.1 Cytoskeleton

The cytoskeleton can be defined as the cell scaffold, which enables to maintain the cell shape. It plays an essential role in various biological processes, such as intracellular transport, cellular division, and cell motility. The cytoskeleton is made of three main components: microtubules, intermediate filaments and actin filaments. Microtubules are the largest cytoskeleton structures (hollow cylinders of $\sim$23 nm diameter), and are involved, in particular, in intracellular transport; intermediate filaments ($\sim$10 nm diameter) provide structural support for the cell; actin filaments, the smallest structures ($\sim$7 nm diameter), are the major components of the cytoskeleton (Lodish, 2008), and account for the cell mechanical stability and motility (Trepat et al., 2008; Stossel, 1993).

Actin filaments and microtubules are dynamical structures, which continuously polymerize and depolymerize (Inoue & Sato, 1967; Lauffenburger & Horwitz, 1996; Kueh & Mitchison, 2009), rapidly remodeling the cytoskeleton (Pollard & Earnshaw, 2004). This dynamics is responsible, for example, for the membrane deformation during

[1]Eukaryotic cells are characterised by the presence of one or several nuclei, contrary to prokaryotic cells, which have no nucleus.

cell motility (Pollard & Borisy, 2003; Liu et al., 2008), cytoplasmic organization and cell division (Kueh & Mitchison, 2009). During its life, a cell has to withstand large forces imposed by the surrounding medium or its own motion, and, at the same time, has to limit its deformation and protect its inner contents (S. Wang et al., 2010). In an eukaryotic cell, previous studies have shown that actin filaments, assembled in a network in the cytoskeleton, support most of the external load, and are able to maintain the cell shape (Janmey & McCulloch, 2007). The actin network mechanical properties are complex, but their knowledge is important to understand the cell physiology (Shin et al., 2004; Bausch & Kroy, 2006; Ingber, 2006; Wagner et al., 2006; Janmey & McCulloch, 2007; Schmoller et al., 2009; Taeyoon et al., 2009). As we will see below (section 1.2.2), the actin network can be described as a polymer entanglement. Its study is therefore interesting not only in biophysics, but also in physics, where many studies focused on the complex mechanical properties of polymer networks (Head et al., 2003; Wilhelm & Frey, 2003; Heussinger et al., 2007; Huisman et al., 2007; Astroem et al., 2008; Conti & MacKintosh, 2009).

1.2.2 Actin filaments

Actin is one of the most abundant, and maybe one of the most intensively studied proteins in eukaryotic cells. As mentioned above, they play diverse roles in the cells, in particular, provide mechanical support for the cell, determine the cell shape, and enable cell motility. In muscle cells, actin filaments play an essential role: they are linked by myosin proteins which enable the filaments to slide past each other, leading to muscle contraction (Hofmann & de Lanerolle, 2006). For a long time, it has been believed that actin exists only in muscle cells, and out of the nucleus (see the reviews by Huxley (1973); Pollard and Weihing (1974); Tilney (1975); Schleicher and Jockusch (2008)). Its presence has been first reported in 1966 in non-muscle cells (Hatano & Oosawa, 1966b, 1966a), and a few years later, in the nucleus (Lane, 1969; Hofmann & de Lanerolle, 2006).

Actin is a globular, small protein (43 kDa), named G-actin when found as a monomer. Interestingly, its structure does not vary much from one species to another. Actin polymerises to form double-helical actin filaments (F-actin), whose diameter is $\sim$7 nm. Actin filaments are polarized with one fast growing end ('barbed' or 'plus' end) and one slow growing end ('pointed' or 'minus' end) (Small et al., 1978; Nicholson-Dykstra et al., 2005).

In steady state, actin monomers (G-actin) and actin filaments (F-actin) coexist (Oosawa & Asakura, 1975), and actin subunits (monomers, dimers, or large subunits) continuously attach and detach at the filament ends. Subunits add faster to the 'barbed' end than to the 'pointed' end. The initial stage of polymerization is slow, but after trimer formation, the filaments grow more rapidly (Pollard et al., 2000), at constant rate (Pollard, 1986; Kuhn & Pollard, 2005). The polymerization rate depends also on the local concentration of actin.

Actin polymerization is regulated by a number of actin-binding proteins (Pollard & Borisy, 2003). Among them, the gelsolin, an actin severing agent, has been proven to be essential for the actin polymerization regulation (Chellaiah et al., 2000; Akisaka et al., 2001; Kotadiya et al., 2008). Different models attempt to describe the complex dynamics of the polymerization process (see for example Brooks and Carlsson (2009, 2010)). In the chapter 4, we will present a model which accounts for the role of gelsolin in the internal dynamics of a particular actin structure: the podosome (section 1.3.2).

1.2.3 Cell motility

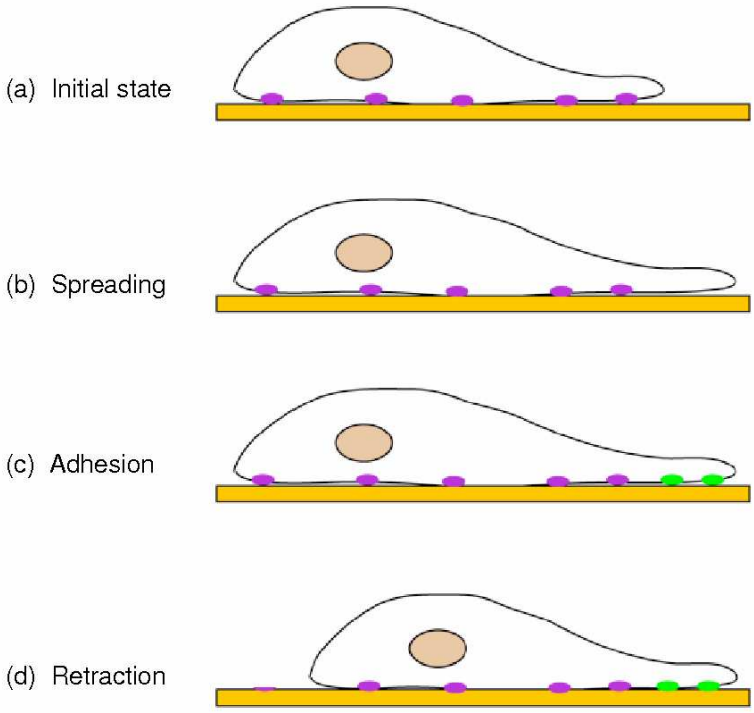

Figure 1.1: Sketch of the cell migration process. (a): Initial state. (b): Cell spreading. (c): Adhesion of the spreading region. (d): Cell retraction from the rear. Old and new adhesion structures are represented in purple and green, respectively (figure from Chabadel (2007)).

The cell migration process can be decomposed in three successive steps (figure 1.1). In a first step, from a initial state at which it adheres to the substrate (figure 1.1 a), the cell spreads in one direction by forming a protrusion (figure 1.1 b). This spreading region then is fixed on the substrate via the creation of new adhesion structures (figure 1.1 c). Subsequently, the cell retracts from the rear, thus migrating towards the spreading region (figure 1.1 d). The protrusion generated at the cell front region requires two processes: the membrane deformation, and the reorganization of the cytoskeleton. This latter is produced by actin filaments polymerization, which pushes the membrane forward (Y. Wang, 1985). Even if it is commonly believed that actin polymerization is the driving force for cell motility (Berro et al., 2007), it is not clear yet

which of these two processes happens first (Loitto et al., 2002; Bereiter-Hahn, 2005). In a recent study, Yang et al. (2009) suggested that the membrane deforms by its own mechanisms, and growing actin filaments just fill the space created by the protrusion, in order to stabilize it, but this scenario has not been confirmed yet. However, it is certain that actin structures play an essential role in cell motility.

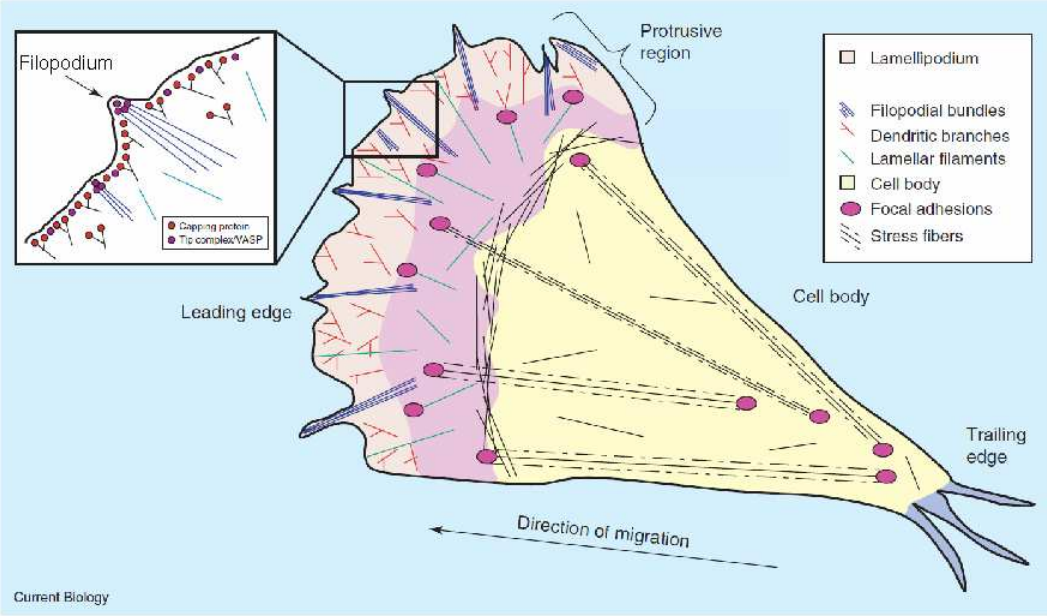

Figure 1.2: Sketch of actin organization in a motile fibroblast. Lamellipodia and filopodia are located in the front region of the migrating cell. Stress fibers, inside the cell body, extend from the leading edge to the trailing edge. Inset: expanded region of the leading edge (from Nicholson-Dykstra et al. (2005)).

In a migrating cell, the actin is generally localized in two regions: at the cell front, where it organizes into lamellipodia and filopodia, and inside the cell bulk, into stress fibers. Figure 1.2 displays the sketch of these actin structures for the example of a fibroblast[2]. Lamellipodia are leaf-like structures, composed of actin filaments oriented in the cell migration direction (Small, 1988). These filaments form a quasi two-dimensional actin mesh, and are highly dynamic: cell migration occurs by their polymerization which pushes the membrane forward (Y. Wang, 1985; Alberts et al., 2002). Contrary to large lamellipodia, filopodia are thin and cylinder. They correspond to actin filaments spreading beyond the lamellipodia frontier and thus forming a protrusion (Small et al., 2002). Stress fibers are bundles of actin filaments assembled by actin-myosin interactions, and forming high order structures. Each end of a stress fiber is connected to a focal adhesion (section 1.3.1). This connection makes it possible to transmit forces between the substrate and the cytoskeleton, which is very important for many cellular functions.

[2]A fibroblast is a type of cell which creates connective tissues. They play an important role in healing wounds.

1.3 Cell adhesion

1.3.1 Adhesion structures

Cell adhesion is essential for many important cellular processes, such as tissue organization and differentiation, embryonic development and, as we have seen in the previous section, cell migration (figure 1.1). Distinct types of adhesions structures between cells and the extracellular matrix (ECM) have been identified (Zamir & Geiger, 2001; Linder, 2007). They can be divided into two main groups: focal adhesion-related structures and invadosomes.

Focal adhesion-related structures

Focal adhesion-related structures include two main types of structures: focal complexes and focal adhesions (figure 1.3). Initially, during cell migration, focal complexes (0.5 to 1 μm dot-like contacts) are formed along the lamellipodia (figure 1.3 a). These complexes are not directly linked to stress fibers. They can mature into large and stable focal adhesions (3 to 10 μm, figure 1.3 a). Focal adhesions are protein complexes, mainly composed of actin filaments, integrin, and some other proteins like vinculin, paxillin and talin (Block et al., 2008). It connects the actin cytoskeleton to the extracellular matrix through β1 and β3 integrins, in particular. The detail molecular composition of focal adhesions is sketched in figure 1.3 b. Focal adhesions are linked to stress fibers (figure 1.2).

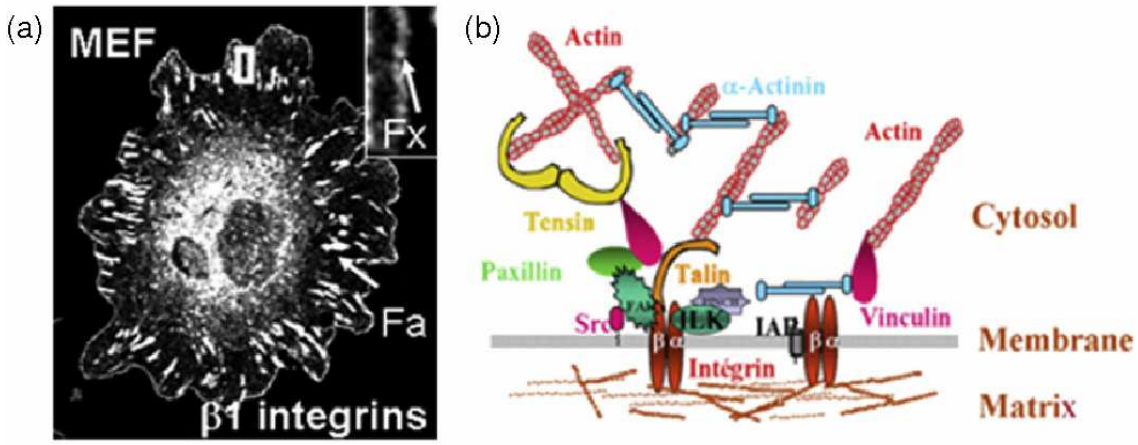

Figure 1.3: Focal adhesion-related structures (figure from Block et al. (2008)). (a): Image of a MEF cell (Mouse Embryonic Fibroblast) displaying focal complexes (Fx) and focal adhesions (Fa). The cell was stained to visualize β1 integrin, the major component of both Fx and Fa. (b): Schematic representation of the molecular composition of focal adhesion.

Focal adhesion are used as anchor by the cell, which can push or pull itself over

the extracellular matrix. During the cell migration, a given focal adhesion gets closer and closer to the cell trailing edge. Once at the trailing edge, it will be dissolved in order for the cell to continue its motion.

Invadosomes

The general name of invadosomes regroups two other structures which enable contact between the cell and the extracellular matrix: podosomes and invadopodia (Linder, 2009). Contrary to focal adhesion-related structures, both are actin-rich structures, composed of dot-like accumulations of actin filaments (F-actin). Because podosomes are one of the main topics studied in this thesis, we describe them in detail in the next section.

1.3.2 Podosomes

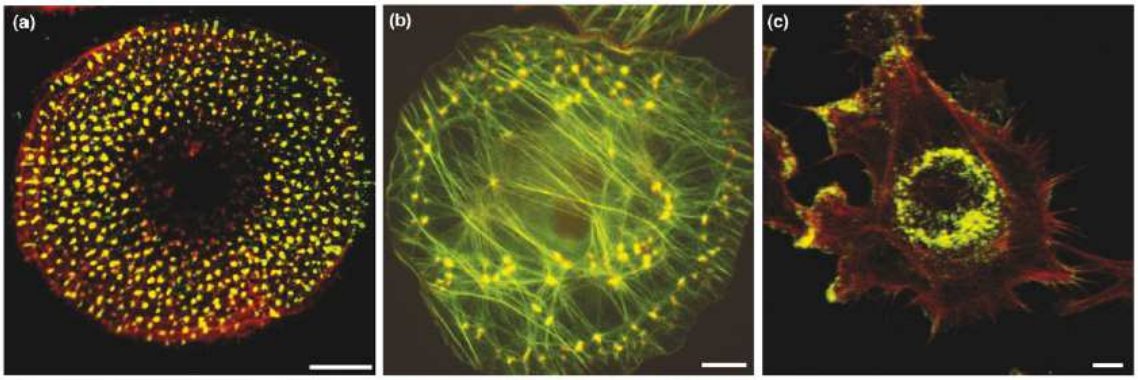

Figure 1.4: Podosomes can be found in different cell types, such as primary human macrophage (a), vascular smooth muscle cell (b) or human umbilical vein endothelial cell (c) [actin in red, (a) WASP in green, (b,c) α-actinin in green]. Scale bars = 10 μm (figure from Linder (2007)).

Structure and molecular composition

Podosomes have been found in monocytic cells such as macrophages, dendritic cells and osteoclasts, and recently also in smooth muscle cells and endothelial cells (Linder et al., 1999; Pfaff & Jurdic, 2001; Linder & Kopp, 2005) (figure 1.4). Since their first description in 1980 (David-Pfeuty & Singer, 1980), their structure and molecular composition has been mostly identified (Destaing et al., 2003; Chabadel et al., 2007). Podosomes have been proven to consist of a dense actin-rich core surrounded by an actin cloud (Pfaff & Jurdic, 2001; Destaing et al., 2003). The actin core is of $\sim 0.5\mu$m in diameter and $\sim 1\mu$m in height.

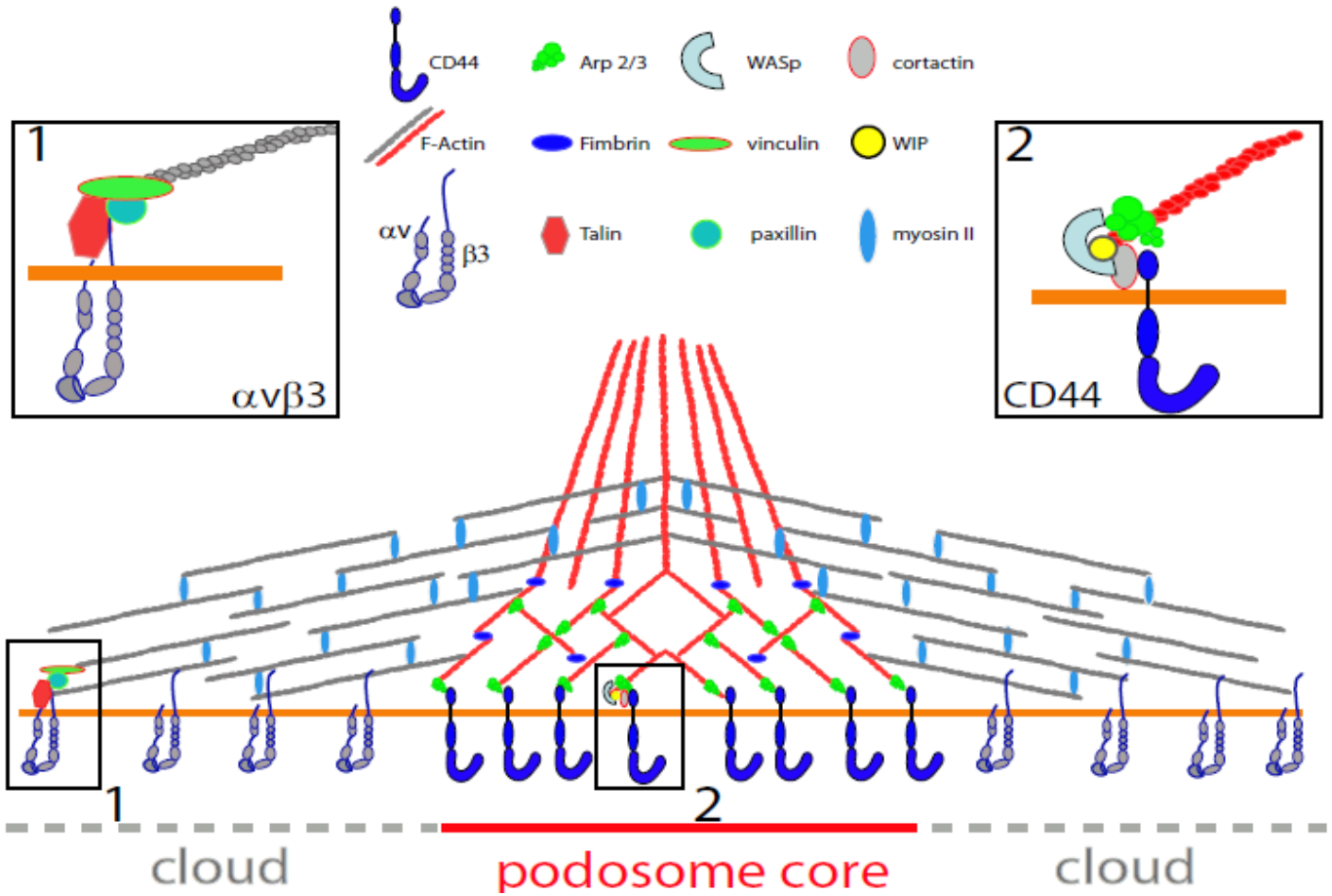

Figure 1.5: Structure and molecular composition of a podosome (Chabadel et al., 2007). The podosome is formed by a dense actin-rich core surrounded by an actin cloud. It is structured and adheres to the extracellular matrix, through the cell membrane (orange line), by proteins (top image) which differ from the core to the cloud. The proteins responsible for the adhesion process are mainly $\alpha v\beta 1$ integrin for the cloud (Inset 1) and CD44 for the core (Inset 2).

Figure 1.5 displays a sketch of the proposed structure and composition of a podosome. Podosomes share with focal adhesions several proteins such as integrins (Zambonin-Zallone et al., 1989; Helfrich et al., 1996; Nakamura et al., 1999), vinculin, paxillin and talin (P. Marchisio et al., 1988; DeFife et al., 1999). However, podosomes clearly differ from focal adhesions or focal complexes in the structural organization of these various proteins. Instead of a cluster of integrins linked to actin stress fibers, podosomes are formed of a diffuse membrane domain of integrins (figure 1.5, inset 1), and associated proteins surrounding a dense actin core (figure 1.5, inset 2) (Pfaff & Jurdic, 2001; Chabadel et al., 2007). The mechanisms that regulate this structure are not known at present but probably involve actin regulators that are specifically found in podosomes. These actin regulators includes Arp2/3, cortactin Wiskott-Aldrich syndrome protein (WASP) and WASP Interacting Protein (WIP), which localize directly underneath the podosome (Gavazzi et al., 1989; Linder, 2007); or gelsolin, an actin-severing agent essential for podosome regulation (Chellaiah et al., 2000).

Function of podosomes

The functions of podosomes are widely investigated (Linder & Aepfelbacher, 2003; Saltel et al., 2004; Linder & Kopp, 2005; Block et al., 2008), but still remain an open question. The main functions of podosomes are considered to be cell adhesion and matrix degradation. Total internal reflection (TIRF) microscopy showed that podosomes are enriched in adhesion mediating integrins (figure 1.5) and form only at the substrate-attached cell side (Linder & Aepfelbacher, 2003). It is possible that podosomes have a role in cell adhesion, as they have been observed to establish close contact to the substratum. Many evidences also showed that the podosomes have the ability to degrade matrix or mineralized bone (Destaing et al., 2003; Saltel et al., 2004). Podosomes are surmised to have a role in cell migration and invasion, to establish localized anchorage, to stabilize site of cell protrusion and to enable directional movement (Linder & Kopp, 2005). However, there is no direct evidence that this surmise is correct and the functions of the podosomes still remain unknown (Block et al., 2008).

Comparison between podosomes and invadopodia

Invadopodia were initially discovered in 1989 (Chen, 1989), and since then have been identified in many metastatic tumor cells (Linder & Aepfelbacher, 2003; Linder, 2007). Like podosomes, invadopodia are dot-like adhesion structures composed by an actin core, associated with regulatory proteins such as cortactin, Arp2/3 and WASP.

Podosomes are typically formed in monocytic cells (macrophages, dendritic cells and osteoclasts), endothelial cells and smooth muscle cells, whereas invadopodia are mostly found in cancer cells. Typically, podosomes have a diameter of approximately 1 μm and a height of about 0.5 μm, whereas the size of invadopodia can be up to 8 μm $\times$ 5 μm in size. Cells form numerous (often more than 100) podosomes but, in many

	Podosomes	Invadopodia
Common features		
Appearance	Dot-like	
Localization	Substrate-attached cell side	
Composition	F-actin	
	Actin regulators [cortactin, (N-)WASP, Arp2/3]	
	Plaque proteins (talin, paxillin, vinculin)	
	Phosphotyrosine	
Differences		
Cell type	Monocytic cells	Carcinoma cells
	Endothelial cells	
	Smooth muscle cells	
	Src-transformed fibroblasts	
Number	20–100 $cell^{-1}$	1–10 $cell^{-1}$
Size	Max. 1 $\mu m \times 0.4 \mu m$	Max. 8 $\mu m \times 5 \mu m$
Persistence	2–12 min	Up to 1 h
ECM degradation[a]	+	+++

[a]The ability of each structure to degrade the matrix is indicated by the number of + signs.

Figure 1.6: Table of comparison between podosomes and invadopodia (from Linder (2007)).

cases, only a few invadopodia (between 1 and 10). Podosomes and invadopodia also differ markedly in their dynamics: podosomes are highly dynamic, with a lifetime of several minutes, whereas invadopodia are more stable and can persist for over 1 hour. Both podosomes and invadopodia can degrade components of the extracellular matrix. However, matrix degradation by podosomes tends to be shallow and widespread, whereas invadopodia show deeper and more focused degradation (Linder, 2007). The common features as well as important differences are summarized in table 1.6.

1.4 Actin organization in osteoclasts

In this thesis, we focused on the study of podosomes in osteoclasts. Osteoclasts are large, multinucleate bone cells, involved in bone resorption (see section 1.4.2). Podosomes exhibit a highly dynamic behavior in osteoclasts, which has not been fully understood yet. In this section, we present a short review of the actin organization (in particular, podosomes) in osteoclasts.

1.4.1 The bone tissue

Bone is a highly specialized form of connective tissue that provides mechanical support for both a tissue and an organ system within higher vertebrates. As such, its basic functions include locomotion, protection, and mineral homeostasis[3] (Downey & Siegel, 2006). The bone morphology can be either cancellous (spongy) or cortical (compact). It can perform multiple mechanical and metabolic functions. In spite of its strength and apparent rigidity, this tissue exhibits a significant flexibility and a constant dynamics. Its constant remodeling includes bone repair and adaptation to the stresses applied on the skeleton (Marks, Jr. & Popoff, 1988; Downey & Siegel, 2006; Wright et al., 2009).

Bone homeostasis is necessary for many process: normal skeletal maturation, bone growth and remodeling. Any imbalance between bone formation and bone resorption causes bone abnormalities, including osteopetrosis (due to decreased bone resorption), osteosclerosis (due to increased bone formation) and osteoporosis (due to increase in bone resorption) (Miyamoto & Suda, 2003; Boyle et al., 2003).

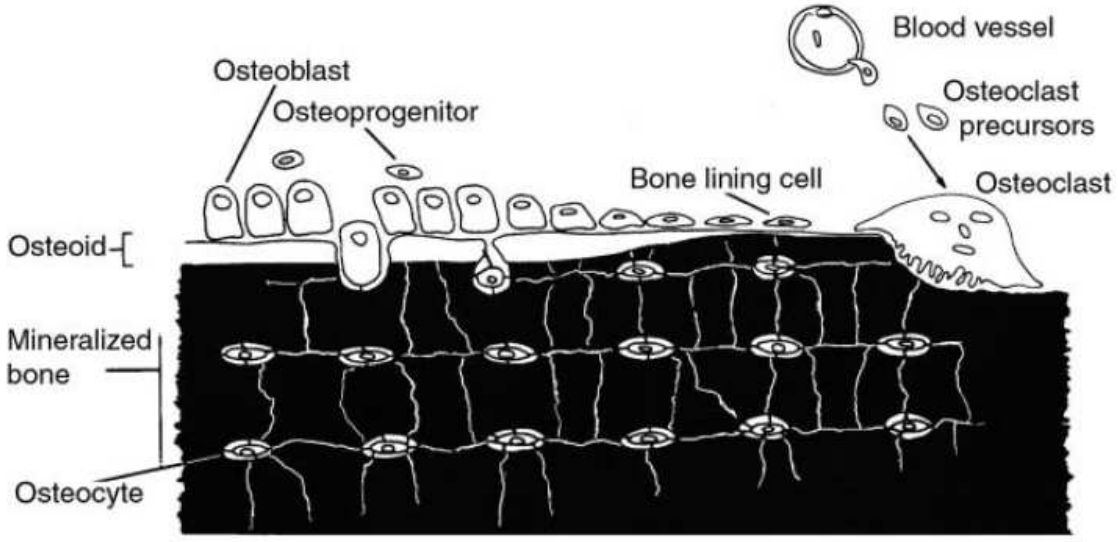

Figure 1.7: Sketch of bone composition (Marks, Jr. & Popoff, 1988). The bone matrix consists in an organic matrix (osteoid), which is ultimately mineralized. The four different types of bone cells are represented: osteoblasts, osteoclasts, bone lining cells and osteocytes (see text).

Bone is composed of two main constituents: the extracellular matrix and the cells (figure 1.7). The extracellular matrix consists in an organic matrix (mainly Type I collagen), named osteoid, which is ultimately mineralized by calcium apatite crystals (He & George, 2004; Saltel et al., 2004).

The four different types of bone cells are: osteoblasts, osteoclasts and bone lin-

[3]Ability of an organism or cell to maintain internal equilibrium by adjusting its physiological processes.

ing cells, which are located on the bone surface, and osteocytes, which permeate the mineralized interior. Osteoblasts, lining cells, and osteocytes are derived from local mesenchymal cells called osteoprogenitor cells. Both osteocytes and bone lining cells are a form of osteoblasts, which are responsible for the formation of new material replacing the old one. On the other hand, osteoclasts are responsible for bone resorption. They are produced from the fusion of monocyte precursors (Walsh et al., 2006). The constant demineralization and resorption of old bone material by osteoclasts, and deposition of new bone by osteoblasts makes it possible for the bone to maintain its multiple mechanical and metabolic functions. They are described in detail in section 1.4.2.

1.4.2 The osteoclasts

Osteoclasts were discovered and some of their morphological features first described by Kölliker (1873). Mature osteoclasts are very large, multinucleate cells, with a diameter of about 50-100 μm (Z. Li et al., 2006). The main function of osteoclasts is to resorb mineralized bone.

Osteoclasts precursors (monocyte cells) are present in hematopoietic tissues[4] such as spleen, marrow and peripheral blood. In vitro, osteoclasts can be developed from the hematopoietic cells of the monocyte-macrophage lineage (Teitelbaum, 2000; Roodman, 1999). These precursor cells are proliferative, and can increase in numbers in response to hematopoietic growth factors. In order to obstain osteoclasts, the precursor cells have to be differentiated[5]. Several cytokines[6] and growth factors are known to affect the differentiation pathway of the osteoclasts. It is now known that two hematopoietic factors are both necessary and sufficient for osteoclastogenesis (Shevde et al., 2000; Boyle et al., 2003): the polypeptide growth factor 'macrophage colony stimulating factor' (M-CSF) and the cytokine 'receptor activator of nuclear factor B-ligand' (RANK-L) (figure 1.8).

1.4.3 Actin organization

When osteoclasts contact the bone or a mineralized matrix (substrate), the resorption process starts. The efficiency of this resorption process depends on the adhesion of the cell to the underlying substrate. In order to do so, the osteoclasts developed a special actin structure, so-called sealing zone.

[4]Related to the formation of blood or blood cells.
[5]Differentiation is the process by which a less specialized cell becomes a more specialized cell type.
[6]Any of various proteins, that carry signals between cells.

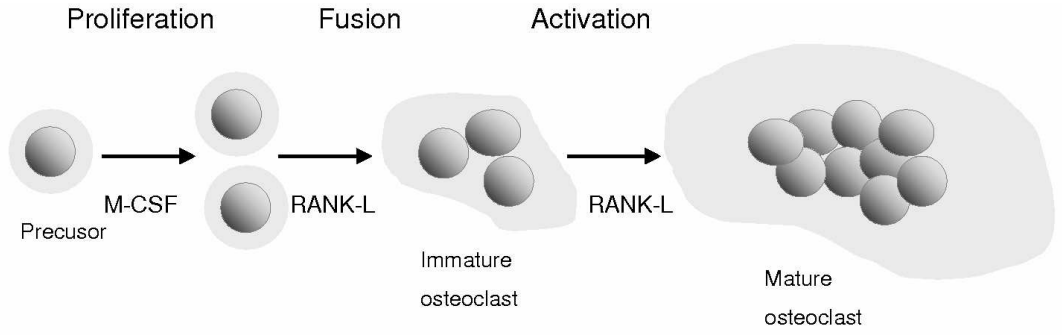

Figure 1.8: Osteoclast differentiation in presence of the growth factor (M-CSF) and cytokine (RANK-L). See text for details (figure adapted from Roodman (2006)).

On mineralized substrates: Sealing zone

When an osteoclast reaches the resorptive site, it becomes polarised, with an apical membrane at the contact with bone and a basolateral membrane at its opposite (Mulari, Vaaraniemi, & Vaananen, 2003). It forms the sealing zone, a large circular band of actin that provides a tight attachment to the bone and seals off the resorption pit (Vaananen et al., 2000; Saltel et al., 2004; Jurdic et al., 2006; Luxenburg et al., 2007). Figure 1.9 indicates a scheme of a bone-resorbing osteoclast. The sealing zone delineates the ruffled border, an active membrane domain, where protons and proteases are secreted in order to dissolve mineral by acidification and degrade extracellular matrix proteins (Mulari, Zhao, et al., 2003). Transcytosis[7] of degraded materials occurs from the basal to the apical membranes (Nesbitt & Horton, 1997; Salo et al., 1997).

On non-mineralized substrates: Podosomes

Surprisingly, osteoclasts do not form the same type of actin structure when they are seeded on a substrate that they cannot resorb (non-mineralized substrate, e.g., glass or plastic). In this case, they do not organize in a sealing zone, but in podosomes structures. These structures are highly dynamic, and mainly depend on the differentiation stages (from small to mature osteoclasts). During early differentiation, podosomes assemble and form clusters (figures 1.10 a and 1.10 b, left). Later, clusters transform into rings (figures 1.10 a, center). These rings expand to form larger rings, by the continuous assembly of new podosomes at their outer ridge and the dissassembly and inhibition of formation on the inner ridge. The rapid ring expansion is of $\sim 2\ \mu$m min^{-1}, relatively constant between osteoclasts (Destaing et al., 2003). Finally, podosomes reach the final characteristic structure of a mature osteoclast: a belt (figure 1.10) (Pfaff & Jurdic, 2001; Destaing et al., 2003).

[7]Transcytosis is the process by which various macromolecules are transported across the interior of a cell.

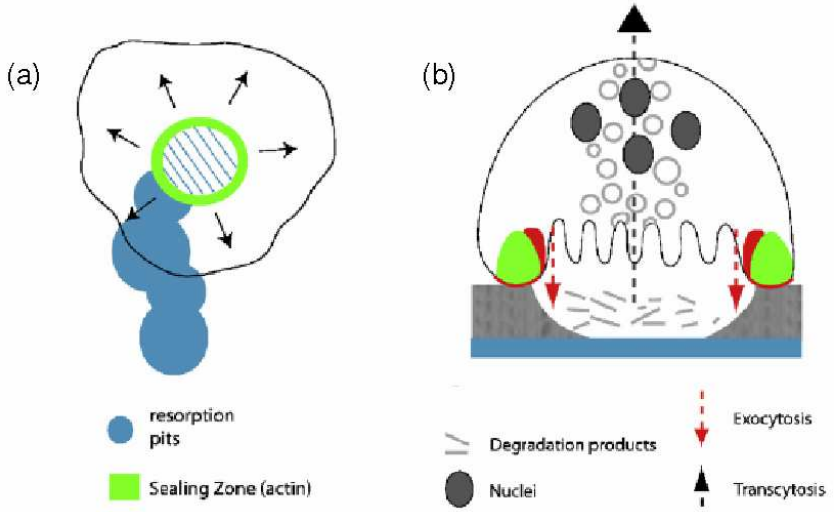

Figure 1.9: Osteoclast bone resorption activity (from Saltel et al. (2008)). (a): The sealing zone delimitates a new resorption pit. After the matrix resorption, osteoclast spread over the substrate. (b): Polarization of a bone-resorbing osteoclasts: matrix degradation products are transported across the interior of a cell (transcytosis).

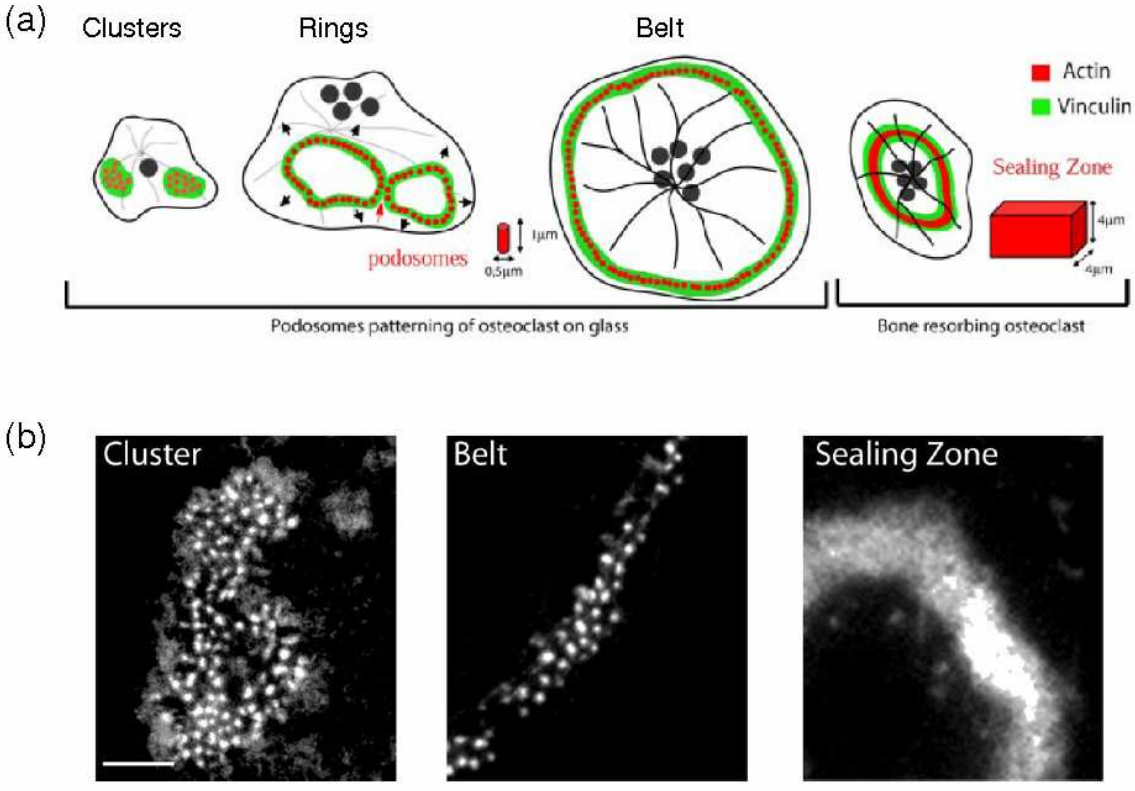

Figure 1.10: (a): Different actin organizations in podosomes and sealing zone. (b): Fluorescence images of actin in a cluster, belt and sealing zone. Clusters correspond to the early stage of differentiation, while a belt is characteristic of a mature osteoclast. When osteoclasts adhere on a mineralized matrix, they form a sealing zone necessary for bone resorption. Figures from Saltel et al. (2004) and Jurdic et al. (2006).

Relationship between podosomes and sealing zone

There are obvious differences between podosomes and sealing zone. Osteoclasts form a sealing zone on a mineralized substrate only, while podosomes are formed on different kind of non-mineralized substrates (glass, plastic, etc.). A podosome is about 1 μm height and 0.5 μm diameter (figure 1.10 a); vinculin is present in its actin cloud (figure 1.5), and spreads around the podosomes core in clusters, rings, or belt (figure 1.10 a). The sealing zone consists of a large band of actin of about 4 μm high and 4 μm wide, surrounded by a double ring of vinculin. Vinculin visualization by fluorescence makes it possible to easily distinguish between a belt and a sealing zone. Indeed, in this latter, the double vinculin rings are clearly separated. Figure 1.10 summarizes the characteristics of podosomes and sealing zone.

On a dynamic point of view, the characteristic recovery time of actin in both structures is about 30 seconds (Saltel et al., 2004). Normalizing by the size of each structure indicates that the actin dynamics in the sealing zone is about 40 times faster than in podosomes (Jurdic et al., 2006).

However, the analogy in shape and molecular composition between podosome belts and sealing zones led to the idea that the sealing zone could be formed by fusion of podosomes (Lakkakorpi & Vaananen, 1991, 1996). A recent experiment based on high-resolution scan electron microscopy (SEM) observation revealed that the basic structural unit of the sealing zone is the same as the individual podosome (figure 1.11). In the sealing zone, the basic units are only denser and more interconnected (Luxenburg et al., 2007). This experimental evidence, as well as later confirmation, seems to have resolved a long-standing question (Gimona et al., 2008; Saltel et al., 2008).

1.5 Open questions and contents of the manuscript

Cell adhesion and migration processes, and in particular, the dynamics of actin organization in osteoclasts, has focused more and more studies during the last decades. Even if the knowledge of such systems has increased considerably, as shown in this introduction chapter, many questions remain open. In particular, the functions of podosomes are not well defined. It is clear that they are involved in matrix degradation. However, their precise role in cell adhesion and migration is still under debate. The goal of this work is to bring some answers on the structure, dynamics and function of podosomes in osteoclasts.

In a first part (chapter 2), we start by the characterization of the cells we are studying (osteoclasts). The osteoclasts are large, multinucleate cells. In order to quantify their unusual flat shape, we study the relationship between the osteoclasts size and their number of nuclei, for different types of substrates. We then focus on the actin organization (clusters, rings or belt) and investigate its relationship with cell size.

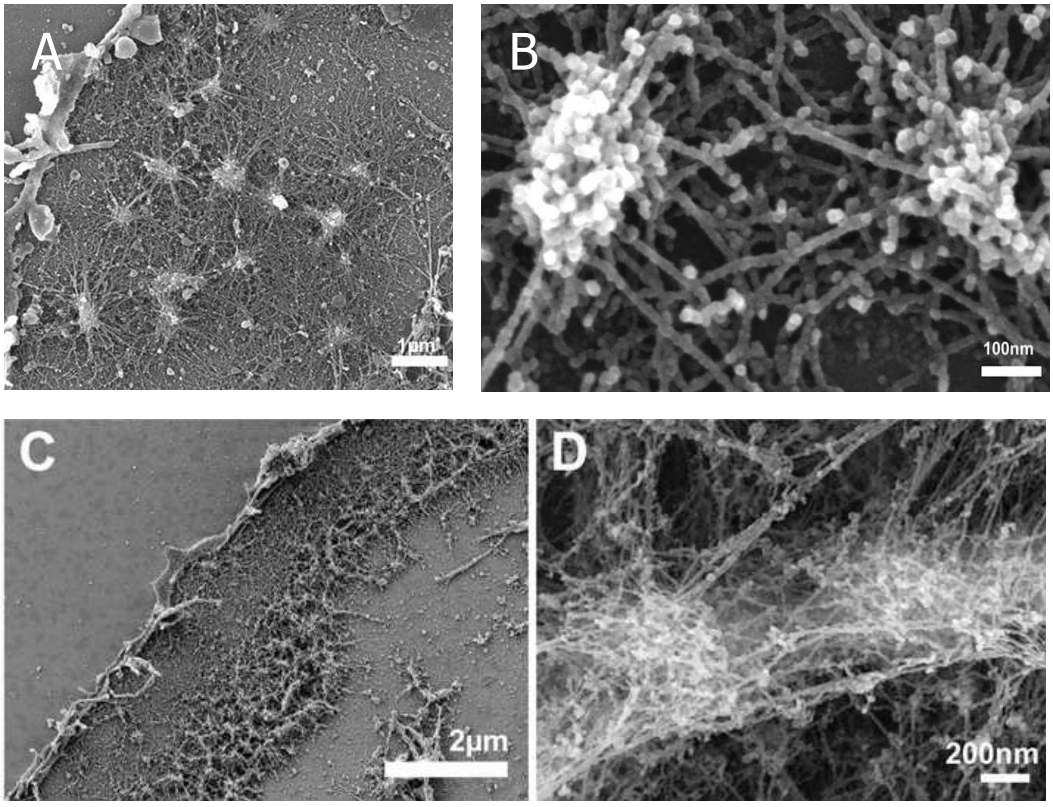

Figure 1.11: Observation of podosomes and sealing zone in osteoclasts with high-resolution scan electron microscopy (Luxenburg et al., 2007). (a): Overview of a podosome cluster. (b): Zoom on two podosomes inside a cluster. (c): Overview of a sealing zone. (d): Zoom on two neighboring subunits of a sealing zone.

In a second part (chapter 3), we follow the podosomes dynamics during different processes: cell early adhesion, retraction, and motion. Because podosomes do not seem to play a direct role in cell adhesion, but are strongly involved in cell spreading, we then focus on cell migration. We use soft gel substrates to get, at short time, information on the force applied by the cell on the substrate. At longer time, we analyse and quantify the cell migration.

In a last part (chapter 4), we develop a model describing the internal dynamics of a single podosome. We improved previous models by accounting for the role of gelsolin, an actin severing agent.

Because podosomes are mainly formed by actin, in the first series of experiments (chapter 2), we use actin stained fluorescence to image the podosomes in osteoclasts. This technique, however, requires to fix the cells[8]. It is therefore not applicable for the study of podosomes dynamics during cell motion. In the second series of experiments, we use cells expressing an actin green fluorescent protein to investigate the podosomes

[8]Cell fixation consists in their rapid killing and preservation, in order to retain as nearly as possible the same characteristics they had when living.

dynamics in live cells.

Chapter 2

Kinetic measurements at the cell scale

Contents

Hu S. et al., An example of anomalous coarsening-kinetics: The osteoclasts, *in preparation* (2010).

The study of the osteoclast adhesion process requires information on the role played by the physical (rigidity, rugosity, ...) or chemical properties of the substrate in the adhesion process. First, we performed kinetic measurements at the cell scale, by investigating the evolution of the typical number of nuclei and cell surface-area as a function of time for cells attaching to rigid substrates presenting different chemical properties (plastic, ITO, pure glass) (section 2.2).

Subsequently, since osteoclasts are formed by fusion of precursors, we wondered whether the dynamic podosome organization was dependent on the kinetics of differentiation time, or on the number of fusion events (section 2.3). This latter can be estimated by the number of nuclei K, present in one osteoclast. We therefore defined quantities that account for the distribution of the actin within the cell, which corresponds to podosome organization, and studied the correlation between the actin distribution in the cell and the number of nuclei.

2.1 Experimental protocols

As we detailed in section 1.4.2, osteoclasts are large multinucleated bone-resorbing cells. They commonly form by fusion of monocyte / macrophage or dendritic precursor cells in the presence of essential cytokines, macrophage colony stimulating factor (M-CSF) and receptor activator of nuclear factor B-ligand (RANK-L) (Burgess et al., 1999; Shevde et al., 2000; Boyle et al., 2003).

Here, the mouse monocyte/macrophage RAW 264.7 cell line (in brief: the RAW cells) is used as precursor of osteoclasts, and they are differentiated to osteoclasts in the presence of RANK-L only (Shevde et al., 2000). The RAW cells were purchased from American Type Culture Collection (ATCC, USA) and grown as indicated by the supplier and described in the section 2.1.3.

2.1.1 Cytokines and media

The cytokines and media which are used for the experiments are described below. α-minimum essential medium (αMEM), Dulbecco's modified eagle's medium (DMEM), Dimethyl sulfoxide (DMSO), phosphate buffered solution (PBS) and ethylene diamine tetraacetic acid (EDTA) were purchased from Invitrogen. Fetal bovine serum (FBS) was from Bio West. We then compound them as described below to culture or operate the cells.

- Soluble recombinant RANK-L was produced in our laboratory from Pichia yeast (Destaing et al., 2003).
- Culture medium: complete DMEM medium (DMEM + 10% fetal bovine serum (FBS) + 1% glutamine + 1% penicillin).

- Differentiation medium: complete αMEM medium (αMEM + 10% FBS + 1% glutamine + 1% penicillin) + 35 ng/mL RANK-L.
- Freezing medium: DMEM + 10% DMSO + 50% FBS + 1% glutamine + 1% penicillin.

2.1.2 Substrates

In order to decipher the role played by the chemical properties of the substrate in the osteoclasts adhesion process, we used three type of rigid substrates presenting different chemical properties: plastic dish, indium tin oxide's glass (ITO glass) and pure glass.

- Plastic substrate: 35 mm diameter cell culture dish.

- ITO glass substrate: 10 mm×10 mm square sample.

- Glass substrate: 10 mm×10 mm square glass slide.

On the day before seeding the cells, we immerse the ITO glass and pure glass into 70% ethanol for 30 min to sterilize them. We then remove the ethanol and dry the substrates by air into the hood overnight. Finally, the glass plates are placed into the wells of a 12-well plate.

2.1.3 Cell culture and differentiation

Usual culture

The usual procedure of culture of the RAW cells is detailed in the following points. Note that during the normal culture, one use the culture medium, described in the section 2.1.1.

- Thaw the RAW cells in water bath at 37°C, but do not thaw completely, leave some ice in the tube. Then transfer the cells into a tube with 10 mL pre-cold culture medium. Centrifuge the tube at 1200 rpm for 4 min at 4°C. Then aspirate the suspension, and add 2 mL fresh culture medium in the tube, gently pipette up and down to create an homogeneous cell suspension.

- Remove a volume of cell suspension (typically 10 μL), and dilute with trypan blue solution (typically 90 μL), gently mix the dilution of cells. Then put 20 μL of this dilution on an hemocytometer[1], count the number of cells in this dilution, and calculate the number of cells in the tube volume. Dilute the cell suspension with fresh

[1]The hemocytometer consists of a thick glass slide with a chamber of well-known depth. The glass slide is engraved with equally spaced perpendicular lines which form a precise grid. We can thus count the number of cells in a specific volume.

culture medium to seed cells with density which is about 100 cells/mm^2 in the plastic culture dish, then place the dish into the incubator with 5% CO_2 at 37°C. Note that the medium has to be changed every two days.

- Usually after two or three days' amplification (growth of the cell population), detach and transfer the cells with a density of 100 cells/mm^2 in a new culture dish. For detaching RAW cells, just flush cells gently with the pipette.

When we have enough RAW cells, we can start to differentiate them to osteoclasts as explained in the following procedure. Note that one can freeze and keep cell sources with a density around 1×10^7 cells/mL at -80 °C in the fridge. We use a special medium for freezing (freezing medium, see section 2.1.1).

Cell differentiation

The RAW cells are then differentiated to RAW osteoclasts as explained in the following procedure. During the differentiation process, the differentiation medium (section 2.1.1) has to be used for the RAW cells.

- Seed the cells with a density 100 cells/mm^2 on the substrates. Put cells in the 5% CO_2 , 37°C incubator to start the differentiation process. The day when differentiation starts is considered day 0.

- Change the medium at the 3rd day for the first time, then change the medium every day.

- From the 3rd day to the 6th day, every half a day, fix the cells in one sample for every type of substrates with 4% paraformaldehyde (PFA). The fixing process consists in the following procedure: rinse the samples with PBS twice to remove the medium, fix the cells with 4% PFA 10 min at room temperature, rinse them with PBS 3 times to remove PFA, and keep the samples in the PBS to store at 4°C.

2.1.4 Immunofluorescence

All the samples are then treated with immunofluorescence process, in order to visualise the actin and the nuclei in the cell. We first explain how to mark the actin cytoskeleton and the nuclei with fluorescent probes, then in section 2.1.5 we explain how to observe in the microscope.

Actin and nuclei were stained by fluorescent molecular probes: Phalloidin Alexa 488 (Invitrogen) and Hoechst 33258 (Kodak) respectively. Fluorescent phallotoxins stain F-actin at nanomolar concentrations are extremely water soluble, and thus provide convenient probes for labeling, identifying, and quantifying-actin in tissue sections, cell cultures, or cell-free experiments. Phalloidin is one of a group of toxins from the

dead Amanita phalloides known as phallotoxins. Phalloidin binds specifically at the interface between F-actin subunits, locking adjacent subunits together (Visegrady et al., 2005). For the Phalloidin Alexa 488, approximate fluorescence excitation (Ex) is 495 nm and emission maximum (Em) is 518 nm (Cooper, 1987). The Hoechst stains are part of a family of fluorescent stains for labelling DNA which are commonly used to visualize nuclei. The dyes are excited by ultraviolet light at around 350 nm, and blue fluorescence light around an emission maximum at 461 nm (Hawley & Hawley, 2004). The immunofluorescence labelling procedure applied to the above samples (fixed cells) is detailed below.

- In order to permeabilize cell membrane, thus to permit fluorescent molecular probes to enter into the cells in the following step, treat cells by 0.2% Triton X-100 with PBS for 7 min at room temperature.

- Rinse cells 3 times with PBS and keep them in PBS.

- F-actin are stained by Phalloidin Alexa 488 (green), 1/50 in PBS + 4% FBS for 1h at room temperature. Nuclei are stained by Hoechst 1/1000 in PBS + 4% FBS for 1h at room temperature. Both F-actin and nuclei are stained simultaneously in the dark to protect from photobleaching.

- After 1h incubation, 2 quick rinses in PBS, then 3 rinses in PBS for 5 min.

- Mount the samples by inverting the cells onto 15 μL FLUOR SAVE (to prevent photobleaching) on glass coverslip: put a 14mm diameter coverslip on the top of plastic dish as the region of sample of plastic; for the ITO glass and pure glass, put a 24 mm$\times$ 60 mm coverslip on the top, in order to keep the cells between the coverslip and the sample.

The cells are now ready for our analysis, and we observe them under a microscope Axioplan 2 imaging (Zeiss) (section 2.1.5).

2.1.5 Fluorescence microscopy

After performing the immunofluorescence process, now we observe the actin and the nuclei in the cell. An Axioplan 2 Imaging fluorescence microscope (Zeiss) was used to visualise the actin cytoskeleton and the nuclei of fluorescence stained osteoclasts on the different substrates[2].

The number of nuclei in every cell on each sample was counted in the microscope with a 20$\times$ objective (Plan Neofluar 20$\times$/0.5). We first used a FITC filter which images actin cytoskeleton to check the position of one cell (Figure 2.1 a), then we switched to a DAPI filter to image and count the number of nuclei within this cell (Figure 2.1 b). The image processing is done by ImageJ software (Abramoff et al., 2004). We count

[2]We performed these experiments at PLATIM (PLAteau Technique Imagerie/Microcopie), IFR 128 BioSciences Gerland - Lyon Sud.

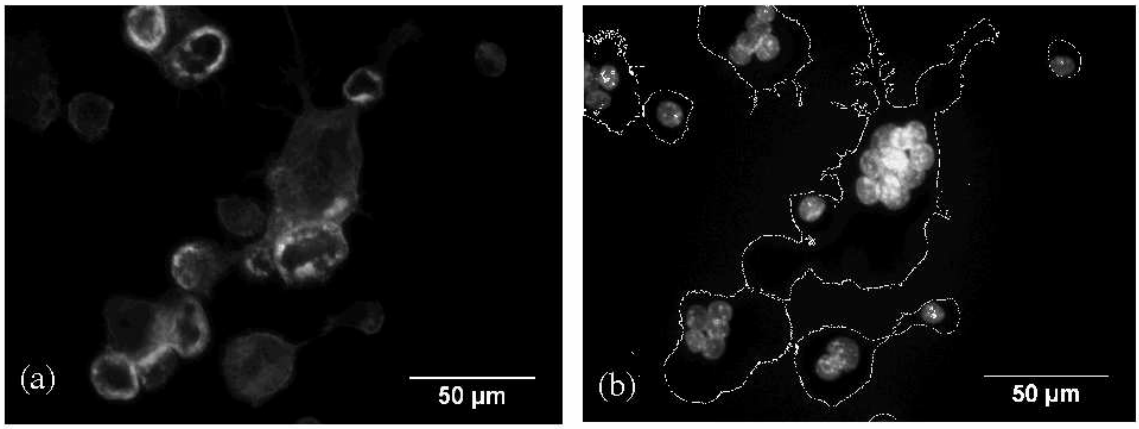

Figure 2.1: Osteoclasts in the fluorescence microscope. (a): Cells are visible thanks to the fluorescence associated with F-actin stained with Phalloidin Alexa 488. (b): Nuclei are revealed by Hoechst. The white lines which mark the contour of the cells are obtained from ImageJ software (Abramoff et al., 2004).

and record the data manually, from the 3rd day to the 6th day, every half a day. We get 7 time points for each substrate, so in total 21 samples. We then use a data analysis software (Igor Pro, WaveMetrics Inc) to infer the histogram of number of nuclei in one cell from these data, for each given time. The results are presented in the following section.

2.2 Kinetic measurements

2.2.1 Typical number of nuclei K^*

In figure 2.2, we display the histogram of number of nuclei, K, in one cell on the glass substrate from the 3rd day to the 6th day. For each time step, we observe that the number of nuclei K in the cell is widely distributed, but there is always a large amount of small cells, even if they just occupy a small part of substrate's surface. Even if the successive fusions of the cells lead to an increase of the average number of nuclei per cell with time, $< K >$ (figure 2.2, inset), this quantity is not really characteristic of the 'typical' cell. Indeed, the calculation includes all the small cells, which bias $< K >$ toward small values. This lead us to develop a method to characterize the typical number of nuclei.

Instead of displaying the histogram of number of nuclei (H) (figure 2.2), we display the histogram multiplied by the number of nuclei ($H \times K$) (figure 2.3). This distribution gives a probability for a precursor mononuclear cell to be in a osteoclast with a given number of nuclei. From this distribution of probability, we define the typical number of nuclei as the median value of the distribution, K^*, as shown in figure 2.3 (inset). On the ITO glass and plastic substrates, the number of nuclei K in the cell is also widely distributed at each time step. We display the distributions of probability in

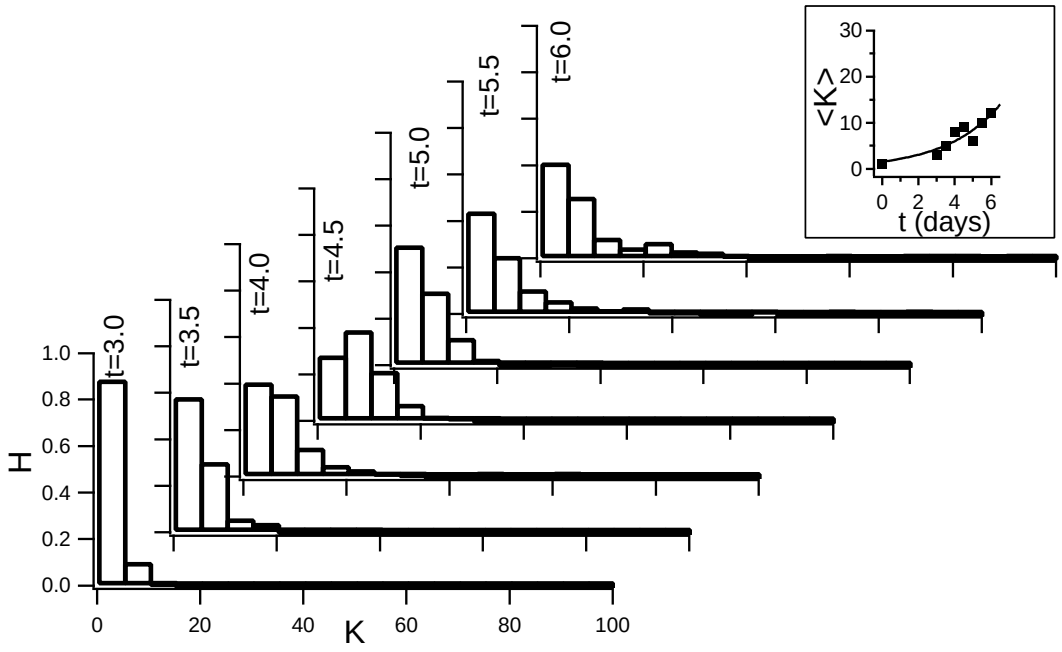

Figure 2.2: Normalized distribution of the number of nuclei K in a cell on the glass substrate. For each time step, the number of nuclei K in a cell is widely distributed. Time t is indicated in days. Inset: the average number of nuclei per cell, $< K >$ vs. time t. We fit the data (black line) by an exponential $< K >= Ae^{\beta t}$ (β is 0.3).

figures 2.4 and 2.5, and get the typical number of nuclei, K^*, for the ITO glass and plastic substrates (figures 2.4 and 2.5, inset), respectively.

We fit K^* by an exponential $K^* = Ae^{\beta t}$, and we observe that K^* increases almost exponentially with time (straight fitting lines in figure 2.6, inset). The growth rate depending slightly on the properties of the substrate: fusions are faster on glass than on plastic, the ITO deposit being an intermediate case (Figure 2.6). Note that for each substrate, at longer time (typically, $t \geq 5$ days), we observe a partition of the distribution. In addition to the group of small cells, a second group of large cells appear. This behavior can be explained by a simple fusion model (see section 2.2.3), and will be discussed in more details at the end of this chapter (section 2.4).

2.2.2 Typical cell surface area A

Once determined the typical number of nuclei K^*, one can easily determine the corresponding typical "cell size".

To do so, we measure the average surface area, A, of several cells (typically 10) having a number of nuclei in the range $[K^*/2,\ 3K^*/2]$. We observe that A also increases almost exponentially with time, the growth rate depending also on the properties of the substrate (figure 2.7). The increase of the surface area is the fastest for the glass substrate, the slowest for the plastic substrate and takes an intermediate value for the

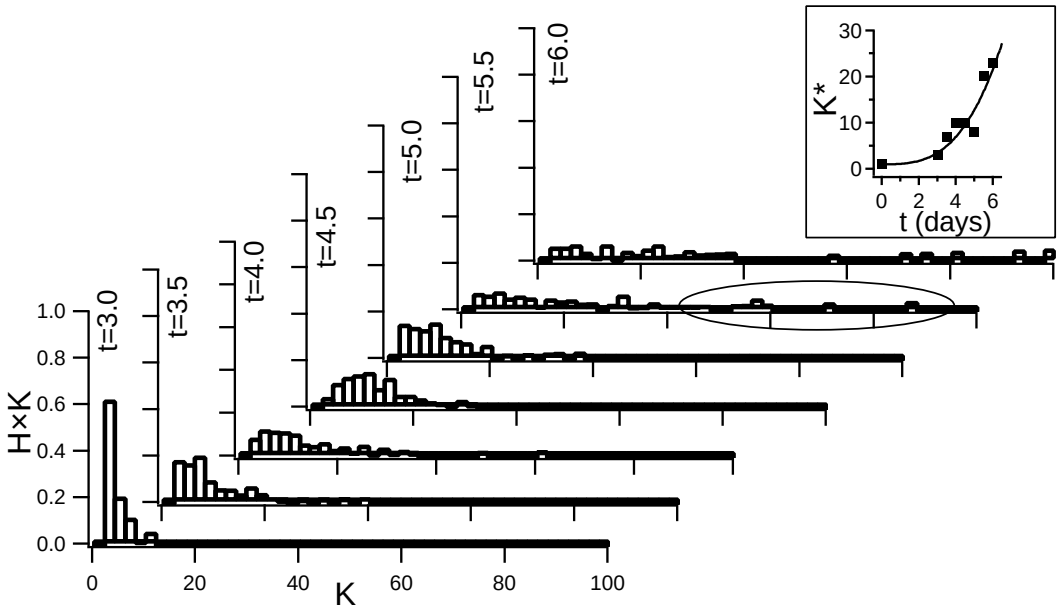

Figure 2.3: Normalized distribution of the probability $H \times K$ for a precursor mononuclear cell to be in an osteoclast with a given number of nuclei K (glass substrate). Time t is indicated in days. Inset: median value K^* of this distribution, considered as the typical number of nuclei in one cell, at time t. Data are fitted by an exponential $K^* = Ae^{\beta t}$ (black line, β is 0.6). Note that at longer time ($t \geq 5.5$ days), we observe a partition of the distribution: a group of small cells and a group of large cells (black circle).

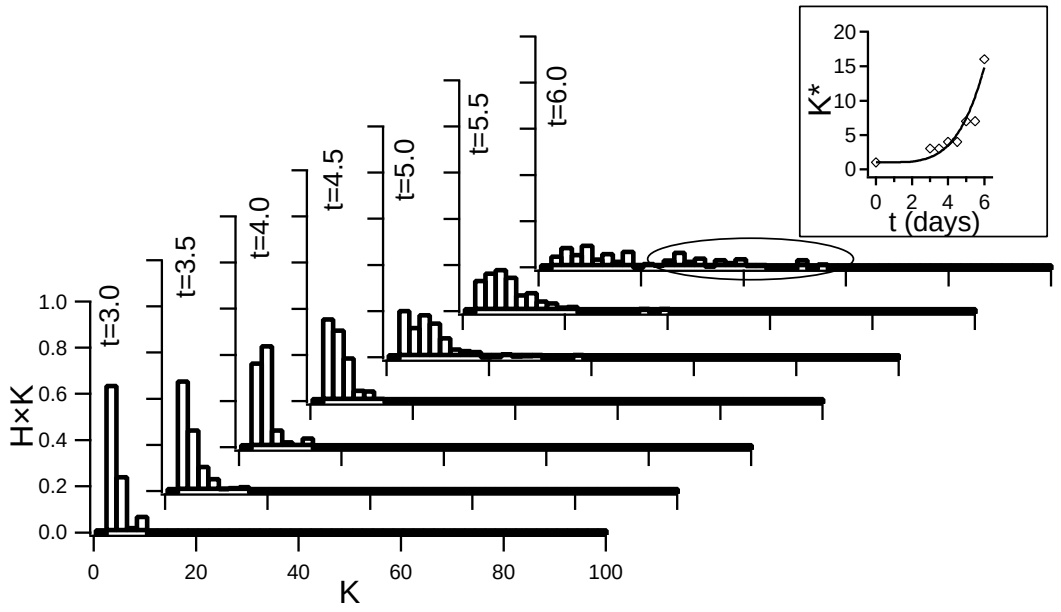

Figure 2.4: Normalized distribution of probability $H \times K$ for a precursor mononuclear cell to be in a osteoclast with a given number of nuclei K (ITO glass substrate). Inset: median value K^* of this distribution, considered as the typical number of nuclei in one cell, at time t. Data are fitted by an exponential $K^* = Ae^{\beta t}$ (black line, β is 0.8). Note that at longer time ($t \geq 6$ days), we observe a partition of the distribution: a group of small cells and a group of large cells (black circle).

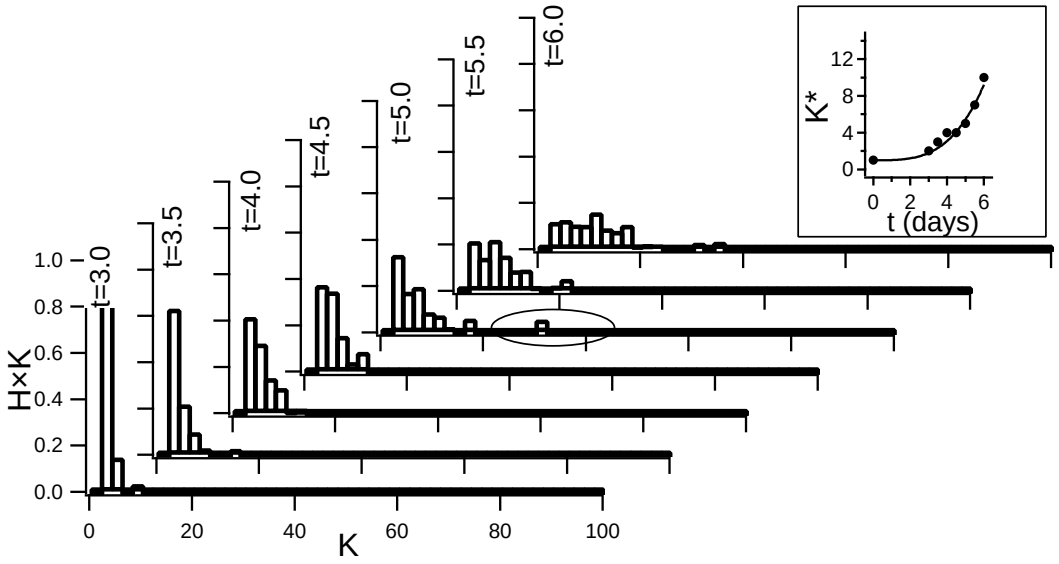

Figure 2.5: Normalized distribution of probability $H \times K$ for a precursor mononuclear cell to be in a osteoclast with a given number of nuclei K (plastic substrate). Inset: median value K^* of this distribution, considered as the typical number of nuclei in one cell, at time t. Data are fitted by an exponential $K^* = Ae^{\beta t}$ (black line, β is 0.5). Note that at longer time ($t \geq 5.5$ days), we observe a partition of the distribution (a group of small cells and a group of large cells). Note that at longer time ($t \geq 5$ days), we observe a partition of the distribution: a group of small cells and a group of large cells (black circle).

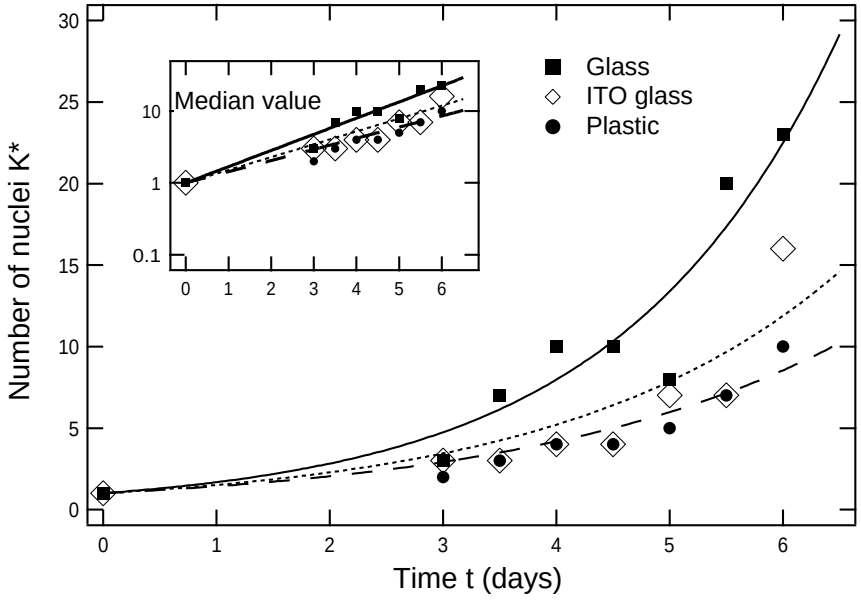

Figure 2.6: Evolution of the typical number of nuclei per cell K^* for different chemical properties of the substrate. Data are fitted by an exponential $K^* = Ae^{\beta t}$ (black lines). For glass substrate, β is 0.6; for ITO glass substrate, β is 0.8; and for plastic substrate, β is 0.5. Inset: $Log(K^*)$ vs. t, black lines are the same exponential fits.

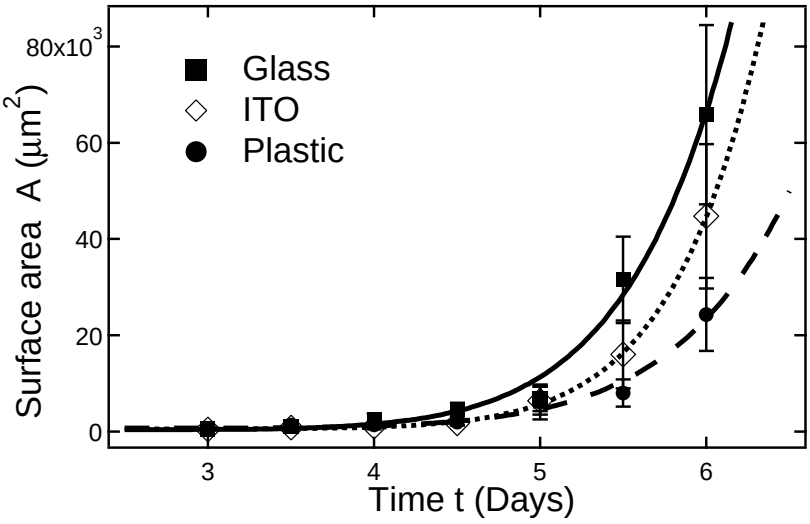

Figure 2.7: Evolution of the typical cell surface area A for different chemical properties of the substrate. A increases almost exponentially with time t, with a growth rate depending slightly on the properties of the substrate.

ITO deposit. Interestingly, the evolution of the surface area is similar to the evolution of K^*. We compare them in the next section.

2.2.3 Analysis

In this section we consider the relation between the typical cell surface area A and the number of nuclei K in the cell (figure 2.8). The experimental data indicate, in spite of a large scatter, that $A \propto K^\alpha$ where the exponent α is larger than the unity, close to 2. Interestingly, this exponent does not depend on the chemical properties of the three substrates used for these experiments.

We remind here that in the case of two liquid droplets, the surface area in the base plane would increase slower than the volume of the droplet, the process being compatible with $\alpha = 2/3$, thus smaller than the unity. To understand the unusual value of the exponent ($\alpha = 2$) which is obtained from the experiment, here, we account theoretically for the temporal evolution of the cell population.

Fusion model

We consider the concentration per unit surface, $C_k(t)$, of the cells containing k nuclei and the corresponding surface area A_k. Assuming that the temporal evolution of the population is induced by a natural growth of the cells, we account for the cell growth by writing that surface areas, A_k, are functions of time. Moreover, we observed that $A_k \propto k^2$, so that we express the surface areas, $A_k \propto k^\alpha$ where α is one parameter of

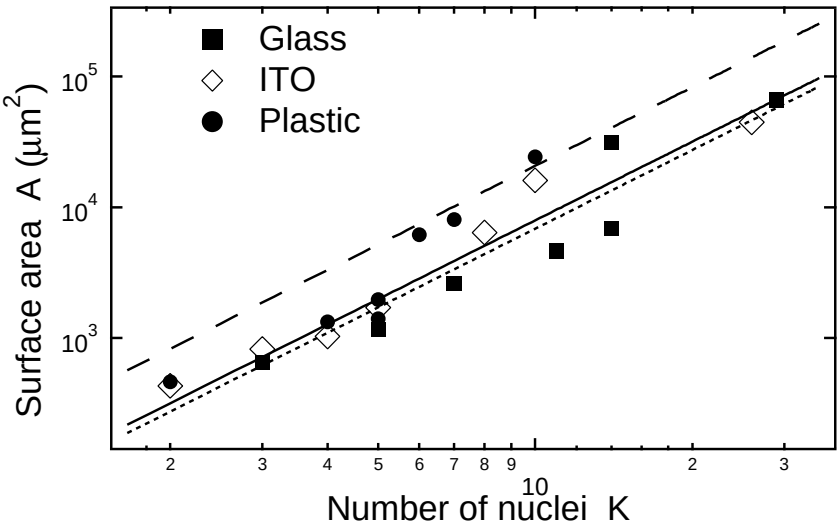

Figure 2.8: Surface area A vs. number of nuclei K. The surface area A of the cell increases almost quadratically with the number of nuclei per cell, K. Data are fitted by a power law $A = K^{\alpha}$ (exponent α is 2).

the problem which value will be discussed later. Considering that cells containing k nuclei are formed by the fusion of two cells, one containing i nuclei and the other $(k-i)$ nuclei, and disappear when they fuse with any other cell, we can write:

$$\frac{\partial C(k,t)}{\partial t} = P[\sum_{i=1}^{k-1} i^{\alpha}(k-i)^{\alpha}C(i,t)C(k-i,t) - C(k,t)k^{\alpha}\sum_{i=1}^{\infty} i^{\alpha}C(i,t) - k^{2\alpha}C^{2}(k,t)] \quad (2.1)$$

The last term of equation 2.1 takes into account the fact that, when $i = k$ in the second term, not only one but two cells with k nuclei disappear by fusion. The parameter P has the dimension of a diffusion coefficient ($\mathrm{m^2 s^{-1}}$).

This very simple model does not aim at describing quantitatively the experimental results. It does not take into account, for example, the growth of the cell population due to cell division (see discussion in section 2.4). The goal here is to investigate the role of the exponent α on the cell population distribution.

Solution

We discuss, here, the temporal evolution of the normalized cell population $C(k,t)$ for different values of the exponent α. The fusion rate between cells has to increase when the cell surface area A increases, and when the cell density C on the substrate increases. In this model, we thus estimate $P \sim A_1 C_0$, where A_1 is the surface area of a mononuclear cell, and C_0 the initial cell density (see section 2.1.3). By considering a typical mononuclear cell diameter of about 10 μm, and $C_0 = 100$ cells/$\mathrm{m^2}$, we fix for our model $P = 0.01$ $\mathrm{m^2 s^{-1}}$. In the following, time t denotes the timestep of calculation.

The theoretical solutions of equation 2.1 with $\alpha = 2/3$ and $\alpha = 2$ are displayed

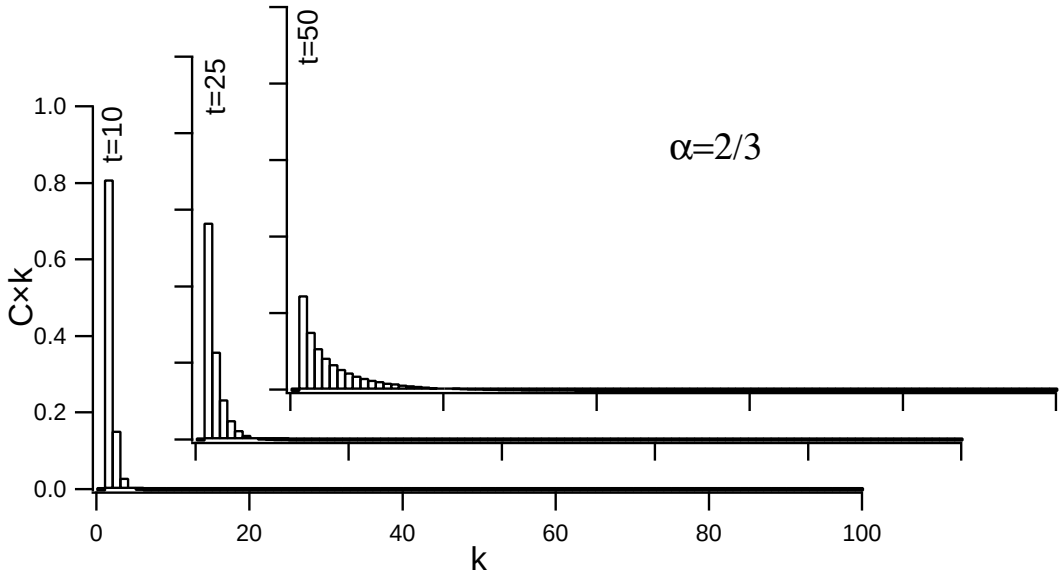

Figure 2.9: Normalized cell population $C(k,t)$ with a given number of nuclei k, for $\alpha = 2/3$. Time t indicated here corresponds to the calculation timestep. The distribution keeps a similar tendency when time increases. Note that for convenience and comparison, we represent here $C \times k$ (see section 2.2.1).

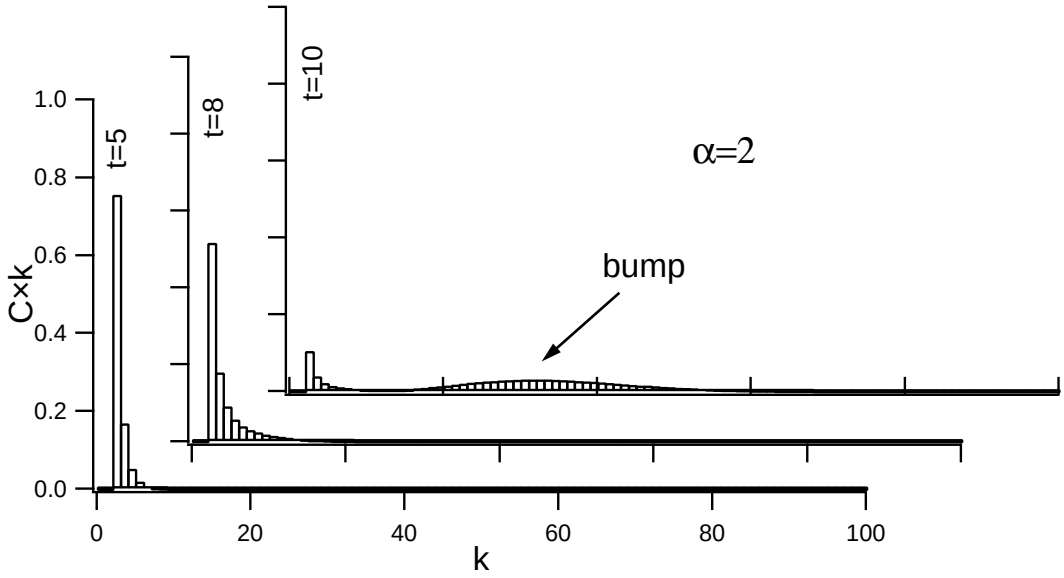

Figure 2.10: Normalized cell population $C(k,t)$ with a given number of nuclei k, for $\alpha = 2$. Time t indicated here corresponds to the calculation timestep. At longer time (for $t \geq 10$), note the partition of the cell population (bump centered at $k = 30$ for $t = 10$). Note that for convenience and comparison, we represent here $C \times k$ (see section 2.2.1).

in figures 2.9 and 2.10, respectively. $\alpha = 2/3$ corresponds to the fusion of two virtual spherical cells. In this case (figure 2.9), the number of nuclei k increases slowly when time increases, and the cell population distribution $C(k,t)$ keeps a similar decreasing tendency through time. For $\alpha = 2$, the number of nuclei k increases quicker with time than for the former value of α (figure 2.10). Moreover, for longer times ($t \geq$10), the

cell population distribution exhibits a bump. For example, at $t = 10$, the secondary maximum in the cell population distribution corresponds to cells with about 30 nuclei. This simple model demonstrates that the unusual value of the exponent ($\alpha = 2$) which is obtained from the experiments is responsible for the partition of the cell population. On the one hand, we observe a group of small cells (small number of nuclei), containing the initial population of mononuclear cells, whose number decreases with time; on the other hand, at longer times, a group of large cells appear.

2.3 Quantifying the actin distribution in the cell

The results from the above section show that the evolution of the cell population only depends slightly on the chemical properties of the substrates used for our experiments. They exhibit, however, the same relationship between the cell surface area A and the number of nuclei K: $A \propto K^2$. Moreover, we observe in the fluorescence image, for all the different substrates, that the podosomes present the same organization dynamics. Through time, they assemble sucessively in clusters, rings, and belt. This podosomes dynamics does not depend on the chemical properties of plastic, ITO and glass substrates. In a series of complementary experiments, detailed in appendix A, we will investigate the effect of the surface topography on the podosomes organization.

In this section, we investigate the podosomes organization dynamics on the flat substrates presented in section 2.1. In particular, we determine if it is dependent on the time after differentiation or on the number of fusions experienced by the cells. Because podosomes are mainly formed by actin, we visualize their organization by the fluorescence stained of F-actin (see section 2.1.5).

We present below the results of the actin distribution in the cell. As we pointed out above, the actin organization is independent of the chemical properties of the substrates used for our experiments. Therefore, in the following, we will present the results associated with a glass substrate only. We shall define various indicators that shall permit to account, with a single numeric value, for the distribution of the actin inside the cell.

2.3.1 Distribution of actin within the cell

First, one can wonder if the actin is homogeneously distributed inside the cell or localizes in specific regions. In order to account for the homogeneity of the actin distribution in the cell, we define the parameter η as follows :

$$\eta = \frac{N_- - N_+}{N_- + N_+} \tag{2.2}$$

where N_+ (respective N_-) denotes, in one cell image, the number of pixels above (resp. below) the mean intensity. From the actin fluorescence image, we extract with ImageJ

software (Abramoff et al., 2004) the image of one cell. We then use Igor software (Igor Pro, WaveMetrics Inc) to compute N_+ and N_-, and estimate η. Theoretically, $\eta = 0$ for an homogeneous distribution of the actin in the cell, whereas $\eta = 1$ if the actin concentrates in one pixel. Thus η is a parameter quantifying the overall actin distribution. As seen from the figure 2.11, η can distinguish the different actin organizations: clusters or belt. For clusters, the value is $\eta \sim 0.1$, and for belt the value is $\eta \sim 0.4$.

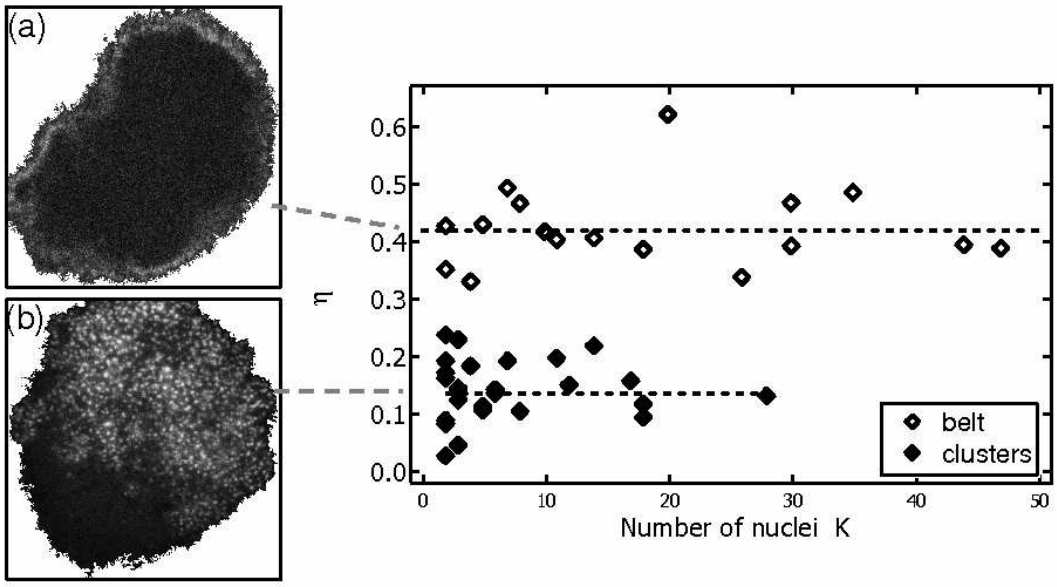

Figure 2.11: Parameter η vs. number of nuclei K. η makes it possible to distinguish the different actin organizations: clusters ($\eta \sim 0.1$) or belt ($\eta \sim 0.4$). Insert (a) and (b) are the images of actin organising in belt or clusters, respectively. η does not depend on the number of nuclei.

In spite of two well-defined different values of η for clusters and belt organization, we do not observe a transition in η when the number of nuclei increases. Belt organization has been reported previously in literature as a characteristics of mature osteoclasts (Burgess et al., 1999; Destaing et al., 2003). For large osteoclasts ($K \geq 30$), we observe indeed belt only (figure 2.11). However, smaller osteoclasts ($K \leq 30$) display either clusters or belt for similar number of nuclei. Moreover, for a given actin organization (clusters or belt), η does not depend on the number of nuclei (i.e. on the cell size). It means that the sole measurement of η cannot help to distinguish between small and mature osteoclasts. A more general conclusion is that the number of nuclei (or number of fusions) cannot provide information on the actin distribution in the cell.

2.3.2 Actin spatial organization in the cell

The parameter η tells us if the actin is concentrated or not, but it does not indicate what is the spatial organization of the actin in the cell (cluster, one or several rings, belt). In order to quantify the actin spatial organization in one cell, we do as following.

In a similar way than the technique presented above, we extract with ImageJ software the image of one cell from the actin fluorescence image. From image analysis (Igor Pro software), we calculate D, the average distance for the actin position from the center, and R, the radius from the center to the cell boundary for a given angle θ (see figures 2.12 (a) and (b)). We then define a second parameter:

$$\zeta = 2\left(< \frac{D}{R} > -\frac{1}{2}\right) \tag{2.3}$$

Theoretically, $\zeta = 0$ for an homogeneous distribution of the actin in the cell, whereas for $\zeta = 1$, the actin concentrates at the boundary. The graph in figure 2.12 displays the experimental results. For clusters, we find $\zeta \sim 0.3$, and for belt $\zeta \sim 0.8$. The parameter ζ does not depend on the number of nuclei. The same conclusion as for parameter η (section 2.3.1) therefore applies: the measurement of ζ cannot help to distinguish between small and mature osteoclasts.

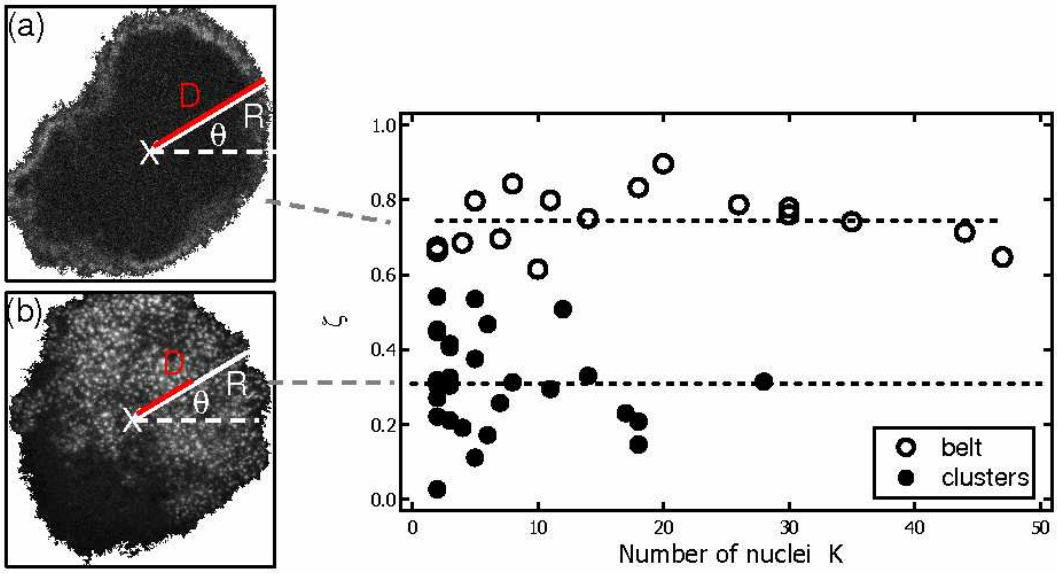

Figure 2.12: Parameter ζ vs. number of nuclei K. The parameter ζ makes it possible to distinguish the different actin organizations: clusters ($\zeta \sim 0.3$) or belt ($\zeta \sim 0.8$). Inset (a) and (b) show the definition of D and R on the images of actin organising in belt or clusters. We find that ζ does not depend on the number of nuclei.

2.4 Discussion

In the first part (section 2.2), we investigated the temporal evolution of a cell population. We focused on the distribution of the number of nuclei K in a cell on different substrates. During the osteoclasts differentiation process, the small cells (small K) grow by fusion with each other. Therefore, their distribution decreases in amplitude and widens with time (section 2.2.1). Interestingly, at long times, we observed a partition of the cell population: a group of large cells (typically, $K \gtrsim 30$) appears. The

time at which this secondary group appears seems to depend slightly on the substrate properties: it happens earlier on the plastic substrate (at the 5^{th} day, see figure 2.5), and later on the ITO glass substrate (at the 6^{th} day, see figure 2.4); the glass substrate is the intermediate case (at the 5.5^{th} day, see figure 2.3). This dependence on the substrate properties is different from the one we found for the evolution of the typical number of nuclei per cell with time. In that case, the cell fusions are faster on glass than on plastic, the ITO deposit being an intermediate case (figure 2.6). We cannot at this point explain this difference. Let us note, however, that the determination of the time at which the large cells group appears is difficult. It does not only depend on the accuracy of the measurements presented here, but it can also depend on the cell culture conditions, in particular, the serum and cytokine batch.

The apparition of a large cells group ('bump' in the distribution) at long times can be accounted for by a simple fusion model (section 2.2.3). It is due to the unusual value of the exponent $\alpha = 2$ in the relationship between the cell surface area A and the number of nuclei K: $A \propto K^{\alpha}$. We remind that the fusion of two spherical droplets would give $A \propto K^{\alpha}$ with $\alpha = 2/3$. The model solution for this exponent value does not exhibit any 'bump', and we observe a general decreasing tendency in the distribution. This model is very simplistic, and has obvious limitations. We considered only the growth of cells by fusion, from an initial mononuclear cell population. In particular, in the real case, the increase of the cell population by cell division is much quicker than the cell diffusion (and subsequent fusion and growth) on the substrate. However, in spite of this strong limitation, the model is able to predict qualitatively the apparition of a large cells group at long times, in the case of $A \propto K^2$.

The experimental value of the exponent $\alpha = 2$ indicates that the cells exhibit a flat morphology. Previous experimental results on osteoclasts showed that their shape can change according to their functional state, varying from flat to spindle morphology (Grano et al., 1996). More recently, it has been observed that on glass substrates, osteoclasts present a flat shape (Saltel et al., 2004). To our knowledge, no quantitative analysis has been made up to now to describe precisely the osteoclasts morphology. However, this question is important, as it has been demonstrated that the cell function and mechanical properties are closely related to their shape (Bacabac et al., 2008). Our experimental results provide a quantitative relationship between the osteoclasts size (number of nuclei) and surface area, thus demonstrating their flat shape on glass substrates. Note that this demonstration stands true for other kind of substrates (plastic, ITO), which follow the same relationship (figure 2.8).

In the second part (section 2.3), we defined two parameters to quantify, on the one hand, the actin distribution in the cell (parameter η) and on the other hand, the actin spatial organization (parameter ζ). The estimation of these two parameters for our experiments show two important results. First, for $K \leq 30$, two cells with the same number of nuclei can exhibit very different actin organization (clusters or belt). This result goes against the common idea that belt organization is the characteristics of mature osteoclasts (Burgess et al., 1999; Destaing et al., 2003). Second, the parameters η and ζ do not depend on the number of nuclei (i.e., on the cell size). Therefore, the number of nuclei in a cell cannot provide information on the actin (i.e., podosomes)

organization – which always evolves from clusters to rings and belt. In other words, the number of fusion is not a good 'clock' to account for the podosomes dynamics.

Chapter 3

Podosomes dynamics and function during the osteoclast adhesion

Contents

Hu S., Planus E., Place C., Wang X., Albiges-Rizo C., Jurdic P. & Géminard J.-C., Podosomes drive osteoclast migration, *to be submitted to J. Cell Biol.* (2010).

In this section, we report a series of experiments performed in order to decipher the role played by the podosomes during adhesion and motility processes of the osteoclasts. On the one hand, we report observations of the podosomal structures at short timescale: in the first experiments, we describe the spatial organization of the podosomes during the early adhesion, retraction, movement process, and we report the evolution of the 3D shape of an osteoclast in relation with the organization of the podosomes in the contact region between the cell membrane and the substrate; in a second experiment, we investigate the force applied by the osteoclast onto the substrate. On the other hand, we report a study of the migration process of a single osteoclast at long time scale, and investigate how the motion of the cell is related to the collective organization of the actin.

In order to investigate the podosomes dynamics in osteoclasts, we need to observe actin fluorescence in live cells. We therefore use RAW cells expressing an actin green fluorescent protein (actin-GFP). These actin-GFP RAW cells are differentiated in actin-GFP osteoclasts. We then follow the actin (i.e. podosomes) dynamics by time-lapse imaging. The experimental protocols are detailed below.

3.1 Experimental protocols

We use the monocytic cell line actin-GFP RAW cells, which makes it possible to observe the actin in live cells. In order to generate the actin-GFP cells, the RAW cells were transfected in our laboratory with FuGENE 6 following manufacturer's recommendations (Roche Diagnostics, IN). The cells are then selected by FACScan (fluorescence-activated cell sorter scan) method in order to obtain a large percentage of positive actin-GFP cells (more than 30%)[1]. The actin-GFP RAW cells are then differentiated into actin-GFP osteoclasts in presence of M-CSF and RANK-L. Note that the RAW osteoclasts used in the experiments presented in the previous chapter were differentiated in presence of RANK-L only (section 2.1). The procedure of normal culture of actin-GFP RAW cells is similar to the one described in section 2.1.3 for RAW cells, and we will not detailed here.

3.1.1 Actin-GFP RAW cells differentiation

For the differentiation procedure of actin-GFP RAW cells, we use the differentiation medium: complete αMEM medium (αMEM + 10% FBS + 1% glutamine+ 1% penicillin) + 35 ng/mL RANK-L + 0.1% M-CSF. The source of M-CSF was supernatant from Sf9 insect cells expressing murine M-CSF from a baculorvirus vector (Z. Wang

[1]FACScan instrument analyses and separates the positive actin-GFP RAW cells (emitting fluorescence signal) from the non-emitting RAW cells. The individual cells in droplets are passed through a laser beam; the droplet is deflected into one of two collection vessels depending on the fluorescence emission.

et al., 1993). Both RANK-L and M-CSF were produced in our laboratory. We then follow the protocol:

- Seed the cells with a density 50 cells/mm^2 in a 12 wells plate, then put them in the 5% CO_2, 37°C incubator to start the differentiation process.

- Change the medium every two days during 6 days.

3.1.2 Detachment and seeding of actin-GFP osteoclasts

Usually after 6 days, small actin-GFP osteoclasts (nuclei number ranges from 5 to 10) are obtained, and after 7 days or 8 days large osteoclasts (nuclei number is more then 10) are obtained. Considering it is not possible to detach very large osteoclasts, we detach the small actin-GFP osteoclasts after 6 days, then seed the osteoclasts on the glass coverslip-bottom dish (MatTeK, US) or on the polyacrylamide gel coated bottom dish to observe the live cells. In order to detach actin-GFP osteoclasts, we use the following procedure:

- Rinse the cells 2 times with 37°C PBS.

- Apply PBS + 0.25 mM EDTA once immediately, to remove non-differentiated monocytic RAW cells.

- Add again 1 mL PBS + 0.25 mM EDTA into each well, and leave the cells in 37°C for 5 min. The fact that EDTA binds metal ions such as calcium ions will remove calcium ions from integrin. Integrin becomes non-activated without calcium ions, which induces cells detachment from the substrate.

- In order to stop EDTA effect, put 1 mL of αMEM medium containing 10% fetal bovine serum (FBS) into each well. EDTA thus binds with FBS rather than with calcium ions. Then flush the cells and change the cells to a new tube.

- Centifuge the tube at 1200 rpm, 20°C during 4 min.

- Count the cells and seed the cells with density of 100 cells/mm^2 on the glass-bottom dish or on the polyacrylamide gel coated bottom dish.

3.1.3 Time-lapse microscopy

In order to visualize the actin in live cells, we use a spinning disk confocal (Yokogawa CUS22) which is installed on a inverted microscope (Leica DMI 4000) in an incubating chamber at 37°C with 5% CO_2 and humidity. Images are obtained with an excitation wavelength 491 nm diode laser (Roper Scientific) through an emission filter which is a bandpass 525-550 nm (Semrock), and recorded with QuantEM camera (Photometrics).

We also use another time-lapse microscope to observe live cells: an inverted confocal microscopy (Axiovert 100M LSM510, Zeiss) with a heating stage (37°C). Images of actin are obtained with an excitation wavelength 488 nm (Argon laser) in a horizontal plane. By scanning the cell along the vertical (z–axis), we can reconstruct its three-dimensional (3D) shape (section 3.2.4).

All the measurements performed with the spinning disk and confocal microscope were done at PLATIM[2].

3.2 Podosomes dynamics

In order to understand podosome dynamics, we report in this section observations of podosomes during different events: early cell adhesion, retraction and movement. In addition, we present the results of 3D imaging, which brings new information on the contact region between the cell membrane and the substrate.

3.2.1 Early osteoclast adhesion

Firstly, we investigate the podosomes dynamics during early osteoclast adhesion. Actin-GFP osteoclasts are detached and then seeded on a glass coverslip-bottom dish. Attachment and spreading during the early adhesion are recorded with spinning disk confocal microscope (section 3.1.3), as soon as osteoclasts are seeded on the dish. Image acquisition is performed every 10 seconds, during 1 hour. Figure 3.1 displays the overlap of green fluorescence image (actin) and Nomarski differential interference contrast optics image (the global view of the cells, in grey). The first event during cell adhesion is the formation of an actin cloud (figure 3.1 a), whereas actin cores appear later when osteoclasts start spreading (figures 3.1 b and 3.1 c). We notice that the podosomes appear in the region in which the cell spreads. These observations reveal that a reorganization of the actin results from or drives the spreading process.

It is interesting to know if we observe a similar, inverse podosomes dynamics during osteoclast detachment. In order to do so, we performed the following experiment.

3.2.2 Osteoclast retraction

In a second step, we perform experiments to investigate the dynamics of podosomes during the cell retraction, which precedes the osteoclast detachment. The cell detachment is induced by addition of EDTA in the medium. Actin-GFP osteoclasts are seeded on a glass coverslip-bottom dish in a incubator at 37°C with 5% CO_2 for 4 hours. Then the osteoclasts are washed quickly by PBS 2 times and put in the spinning disk confocal

[2]PLAteau Technique Imagerie/Microcopie, IFR 128 BioSciences Gerland - Lyon Sud.

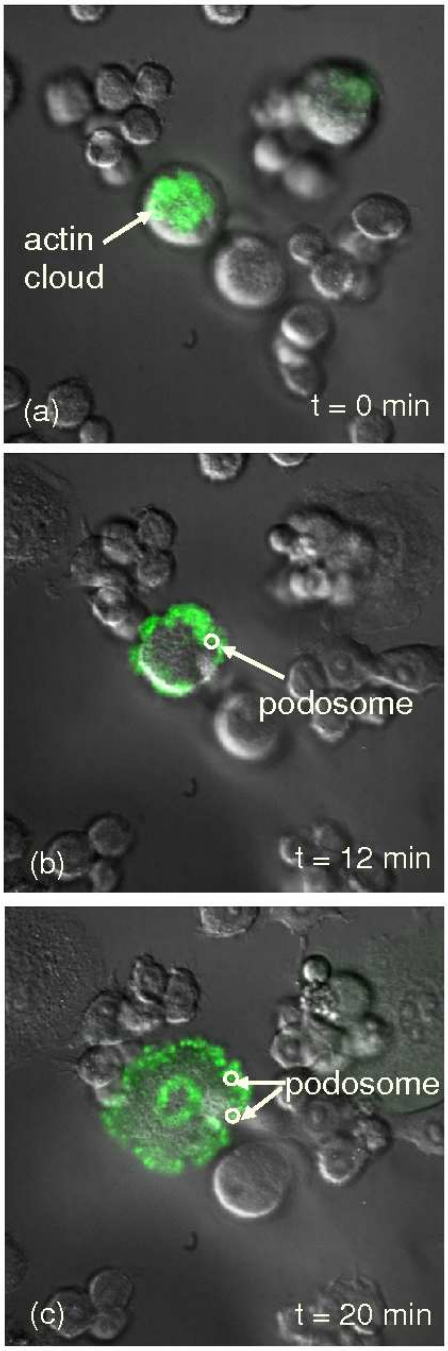

Figure 3.1: Podosome dynamics during early osteoclast adhesion. (a): An actin cloud appears in rounded cells. (b): After 12 min, actin cores (podosomes) appear while the cell starts spreading. (c): After 20 min, the podosomes are organized in large dynamical rings. Actin is revealed by fluorescence microscopy (in green), whereas images of the whole cell are obtained in the Nomarski-differential-contrast mode (in grey).

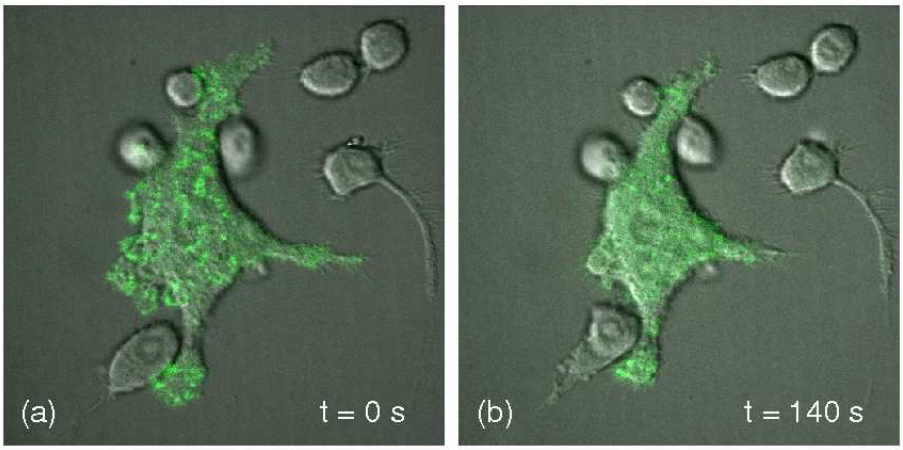

Figure 3.2: Podosome dynamics during osteoclast retraction. (a): At t=0, podosomes form several rings. (b): At t=140 s after the addition of EDTA in the medium, there are no more podosomes, but the cell still adheres to the substrate. Actin is revealed by fluorescence microscopy (in green), whereas images of the whole cell is obtained in the Nomarski-differential-contrast mode (in grey).

microscope. The images are obtained every 2 seconds, during 6 minutes. Previous to the detachment (at t=0), podosomes form several rings (figure 3.2 a). After addition of EDTA, podosomes rapidly disappear. After 140 s there are no more podosomes (figure 3.2 b). Note however that, even if the podosomes rapidly dissociate and the cell retracts, the cell still adheres to the substrate.

3.2.3 Osteoclast movement

Furthermore, we observe the podosomes dynamics during random osteoclast movement. Actin-GFP osteoclasts are seeded on a glass coverslip-bottom dish in a incubator at 37°C with 5% CO_2 for 4 hours. We then place the dish in the spinning disk confocal microscope (section 3.1.3) to observe osteoclast movement. The images are obtained every 2 seconds, during 30 minutes. We observe that during osteoclast movement, podosomes appear at the periphery of the spreading area, whereas they disappear from the retracting regions. Figures 3.3 a and 3.3 b are two instants (t=12 min and t=27 min, respectively) extracted from a cell movement. We observe that podosomes are present in the spreading regions whereas they are absent from the retracting regions.

3.2.4 Osteoclast 3D imaging

In addition, we observe, through 3D imaging, the deformation of actin-GFP osteoclasts on a glass coverslip in an inverted confocal microscope (Axiovert 100M LSM510, Zeiss) (section 3.1.3). We scan and obtain a series of green fluorescence images every 1 μm in the horizontal plane over a height which is slightly larger than the height

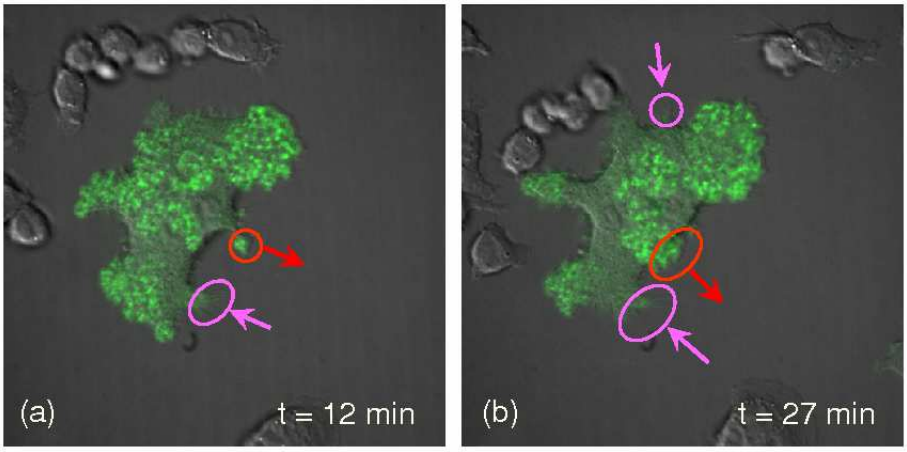

Figure 3.3: Podosome dynamics during osteoclast movement at (a): $t = 12$ min and (b): $t = 27$ min after the image acquisition starts. Podosomes are present in the spreading regions (red contour and arrow) whereas they are absent from the retracting regions (pink contour and arrow). Actin is revealed by fluorescence microscopy (in green), whereas images of the whole cell is obtained in the Nomarski-differential-contrast mode (in grey).

of osteoclast. From the series of slices along the vertical (z–axis), we reconstruct the three-dimensional (3D) image by using ImageJ software (Abramoff et al., 2004). We repeat this operation and obtain 3D images every 15 min, during 210 min.

In figure 3.4, we display a 3D image tilted 10° from vertical. This view makes it possible to observe both the shape of the cell and the podosomes in the substrate plane. At the beginning, in the base plane the podosomes are organized in two large clusters, the largest being on the left-hand-side (figures 3.4 a and b). When time increases, the left-hand-side cluster transforms into a podosome ring, whereas the right-hand-side cluster disappears (figures 3.4 c and d). In the meantime, one observes the cell spreading towards the left direction. Again, the reorganization of the podosomes is proven to result from or to drive the spreading process. Furthermore, the experiment reveals that rapid expansion and flattening of the cell are associated with the growth of a podosome ring (figures 3.4 b and c).

3.2.5 Discussion

Even if podosomes are widely investigated, their exact function still remains unknown (Block et al., 2008). It is commonly believed that they are involved in cell adhesion, in particular (Linder & Aepfelbacher, 2003; Linder & Kopp, 2005; Block et al., 2008). They are also surmised to have a role in cell migration and invasion (Linder & Kopp, 2005). In our experiments, we show that during early adhesion or retraction, osteoclasts are adherent but do not exhibit podosome cores. These observations lead us to propose that podosomes do not play a direct role in osteoclast adhesion.

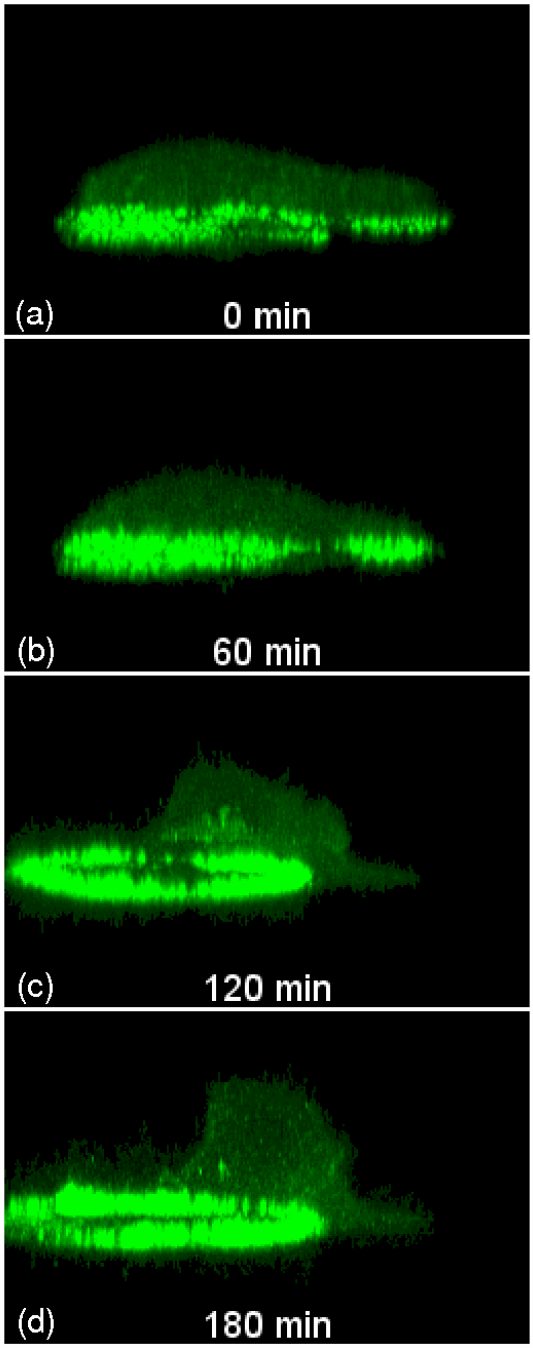

Figure 3.4: 3D imaging (tilted 10° from vertical) during osteoclast movement. Actin is revealed by green fluorescence. At the beginning, in the base plane the podosomes are organized in two large clusters, the largest one being on the left-hand-side (a and b). When time increases, the left-hand-side cluster transforms into a podosome ring, whereas the right-hand-side cluster disappears (c and d). Simultaneously, the cell expands toward the actin structure and flattens above the podosome structure (b and c).

During osteoclast movement, however, podosomes appear at the periphery of the spreading area whereas they disappear from the retracting regions. 3D images also show that there is a strong coupling between cell spreading and podosomes formation. This leads us to propose that podosomes might play a role in osteoclast motility. In order to investigate this hypothesis, we perform the following experiments: on the one hand, at short times, we focus on the tension applied by the osteoclast on the substrate; on the other hand, at long times, we examine the osteoclast migration. For these two processes, we analyse the coupling with podosome dynamics.

3.3 Cell tension measurement

In order to decipher the role played by the actin structures in the cell motility, we report the first experiments in which we assessed the force applied by the osteoclast onto the substrate. To do so, we observe the displacements induced by moving osteoclasts in a polyacrylamide hydrogel[3].

Polyacrylamide hydrogel is a good candidate for the study of cell-substrate mechanical interactions. Indeed, it shows a rapid and complete recovery on removal of the stress (Beningo et al., 2002; Y. Wang & Pelham, 1998). In addition, the rigidity of the gels can be easily controlled by varying the concentration of the bis-acrylamide crosslinker. Polyacrylamide hydrogels are nonfluorescent, but fluorescent beads can be seeded into the gels during the gel fabrication, which makes it possible to detect the movement of gel in the fluorescent microscope. Furthermore, it is possible to link proteins to help the cells adhesive on the gel surface.

Considering these advantages, in order to perform cell tension measurements, we produced the polyacrylamide hydrogel with the collaboration of E. Planus (Institut Albert Bonniot Centre de Recherche, Grenoble). We followed the procedure from Damljanovic et al. (2005). The stiffness of the gel depends on the percentage of acrylamide-bisacrylamide in solution (Collin et al., 2006). We varied this percentage, and measured the gels stiffness in Grenoble.

3.3.1 Polyacrylamide hydrogel

Here we detail the steps for polyacrylamide hydrogel fabrication, gel surface activation and conjugation of protein with gel surface.

[3]These experiments were performed in collaboration with E. Planus at Institut Albert Bonniot Centre de Recherche, Grenoble.

Gel fabrication

In order to observe the live cells on the polyacrylamide hydrogel surface, we produce a very thin layer of gel on the glass coverslip bottom (diameter 14 mm) of MatTek plastic dish (diameter 35 mm). We first treat the glass surface to make it possible to covalently attach polyacrylamide gels, then fabricate and polymerize the gel on the glass coverslip surface with the following protocol:

- Treat the glass coverslip surface with Bind-Silane (g-methacryloxypropyltrimethoxysilane, GE life science), to covalently attach polyacrylamide gels to a glass surface.

  - Prepare 15 mL Bind-Silane solution:

  484 μL 10% acetic acid + 55.7 μL Bind-Silane + 15 mL ethanol.

  Put 500 μL solution on each dish glass coverslip surface, and let them dry under the hood.

  - At the same time, treat 12mm-diameter coverslips with 15 μL Sigmacote (Sigma), then remove quickly Sigmacote from the coverslips. Let coverslips dry under the hood.

- Prepare the polyacrylamide solutions: We then prepare polyacrylamide gels with or without fluorescent beads (diameters 200 nm), by using a 40% acrylamide solution and a 2% bisacrylamide solution. Two different rigidities are obtained, according to the ratio 8% acrylamide/0.05% bis-acrylamide for very flexible gel (stiffness 0.5 kPa) or a 8% acrylamide/0.1% bis-acrylamide for flexible gel (stiffness 3 kPa).

  - For the gel of 3 kPa (8% acrylamide and 0.1 % bisacrylamide):

  500 μL acrylamide 40% + 125 μL bisacrylamide 2% + 25 μL Hepes 1 M (pH=8.5) + 1850 μL H_2O (+ 80 μL of the solution containing beads)

  - For the gel of 0.5 kPa (8% acrylamide and 0.05 % bisacrylamide):

  500 μL acrylamide 40% + 62.5 μL bisacrylamide 2% + 25 μL Hepes 1 M (pH=8.5) + 1913 μL H_2O (+ 80 μL of the solution containing beads)

- Gel polymerization:

  Add initiators 12.5 μL APS + 1.25 μL TEMED into the solution to generate polymerization.

  Then put 8 μL polyacrylamide solution on the Bind-Silane treated coverslip surface (14mm-diameter), cover a Sigmacote treated 12mm-diameter coverslip on top, and let the polyacrylamide polymerize for 20 min.

- Remove the top coverslip with a crochet, and rinse the gel with PBS. Conserve the gel into the PBS, and store it at 4°C before activating it.

Gel surface activation

In order to create a covalent link between the gel surface and the protein which will be next coated on the gel, we activate the gel surface with the following protocol:

- Immerse the gel in pure hydrazine hydrate (Sigma) for 2 h.
- Wash the gel in 5 % glacial acetic acid for 1 h, and then for 1 h in distilled water. Activated gel, kept in PBS at 4°C, can remain active for at least 2 months.

Conjugation of vitronectin with polyacrylamide gel

Vitronectin is an kind of protein which is proved to be a good extracellular matrix for oesteoclasts adhesion on the substrates. Here, we oxidate and conjugate the vitronectin with the actived polyacrylamide gel surface with the following protocol.

- Solubilize the vitronectin (BD Biosciences) in PBS with the concentration of 100 μg/mL.
- In order to enable oxidation, dilute the vitronectin solution in 50 mM sodium acetate buffer to 10 μg/mL with pH=4.
- Oxidation is achieved by adding 3.6 mg/mL sodium periodate crystals (Sigma) and incubating at room temperature for 30 min.
- Add 500 μL oxidized protein on the gel surface, incubate at room temperature for 1 h, then wash it in PBS.

3.3.2 Displacement field of polyacrylamide gel substrate

We differentiate the actin-GFP osteoclasts and seed them on the polyacrylamide gel substrate (stiffness 3 kPa), as described in section 3.1.1 and 3.1.2. The cells are incubated (37°C, 5% CO_2) for 4 h, and, then, are imaged by time-lapse video in an inverted microscope every 1 minute during 46 minutes. We observed the displacements induced by moving osteoclasts in the polyacrylamide gel. The gel is seeded with red fluorescent beads whose displacement field is observed by PIV technique (see below). The actin in the cell and the beads are revealed by using two different emission filters (respectively, GFP and Rhodamine).

Particle Image Velocimetry (PIV)

This technique makes it posssible to determine the displacement field by introducing particles (tracers) in the system (here, the polyacrylamide gel). By cross-correlation

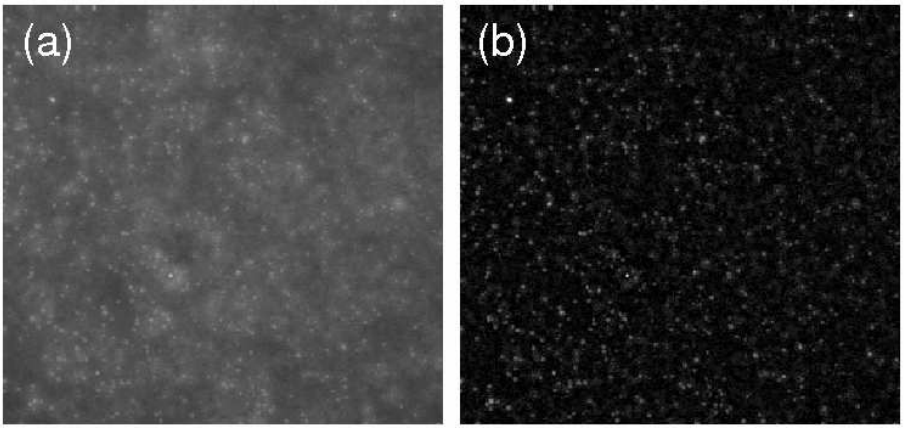

Figure 3.5: (a): Raw beads fluorescent image. Note the strong contrast variations of the background. (b): Beads fluorescent image after background removal.

analysis of successive images, one can quantify the displacement (or velocity) field. PIV methods have been widely developed for the last ten years, bring many improvements on particle detection and image analysis (Raffel et al., 1998; Okamoto et al., 2000). We use an open software package JPIV[4] for PIV calculation, and determine the displacements of the fluorescent beads in the (X, Y) plane with respect to their initial positions.

Analysis of displacement field

In the raw fluorescence images (e.g. figure 3.5 a), we can clearly distinguish the beads. However, the background presents strong variations in contrast, which introduces bias or errors in the PIV calculation. The images are thus first processed by software ImageJ (Abramoff et al., 2004) to remove the background (figure 3.5 b). Moreover, during the image acquisition, we observe global fluctuations of the images, unrelated to the beads motion. These fluctuations may be due to temperature fluctuations and subsequent dilation and contraction of the stage. They were removed from the images by using the plugin Stabilizer (K. Li, 2008).

We then merge the beads displacement fields and the corresponding cell fluorescent images by using Matlab software (The MathWorks). The experiment points out that the displacements are concentrated around the podosomal structure (ring) whereas no displacement is observed in absence of podosomes (figure 3.6). Furthermore, when the structure grows and spreads, the substrate displacements are mainly oriented outward the ring. Thus, the podosomal structure is subjected to an internal tension which tends to extend the ring. In turn, the ring is subjected to a compressive force from the substrate which tends to reduce its size.

[4]http:/www.jpiv.vennemann-online.de/

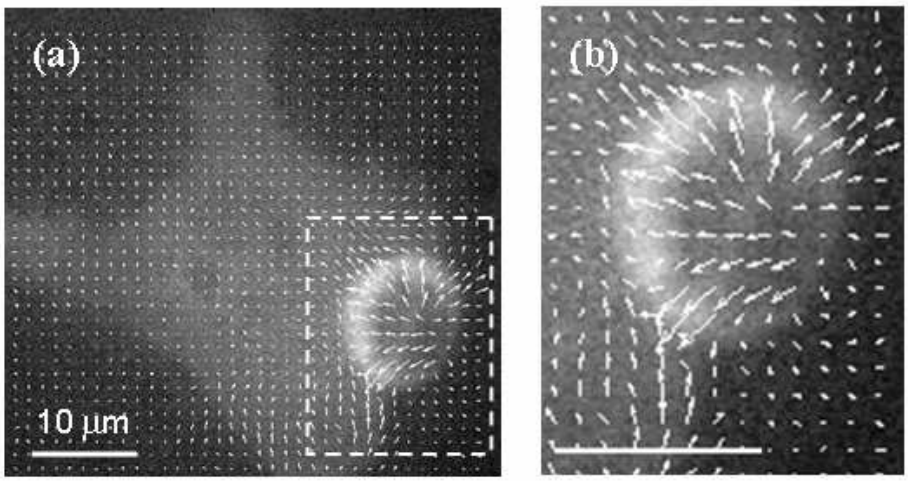

Figure 3.6: Substrate displacement field. (a): The superposition of the cell image and the displacement field (white arrows) shows that the displacements are significant only around the podosomal structure (ring). (b): Enlargement of the podosomal structure. The displacement of the beads clearly points outward the ring. Scale bar is 10 μm.

3.4 Osteoclast migration

In order to assess the role played by the actin structures in the cells motility, we observe, in the spinning disk confocal microscope, the migration of actin-GFP osteoclasts, on the polyacrylamide gel substrate[5]. In this experiment, we use a substrate of 3 kPa stiffness, without fluorescent beads. Actin-GFP osteoclasts are differentiated (section 3.1.1), then detached and seeded on the polyacrylamide gel substrate (section 3.1.2). The cells are incubated (37°C, 5% CO_2) for 4 h. We then image the osteoclasts in the time-lapse spinning disk confocal microscope every 5 minutes during 8 hours (figure 3.7). Images from the microscope and associated data are analyzed using the image processing and analysis software ImageJ (Abramoff et al., 2004) and the technical graphing and data analysis software Igor Pro (WaveMetrics, Inc.).

In figure 3.7, we observe interesting features in the cell migration dynamics. The formation of actin rings inside the cell accompanies the elongation of the cell in one given direction. Here, we define the cell length L as the longest segment among its two main axis at every instant. When L reaches about two times the cell typical size, we observe that the cell jumps in the direction in which it is elongated (figure 3.7, $t = 120$ to 180 min). After this jump, the cell starts elongating in the (almost) perpendicular direction, due to the growth of new actin rings.

In order to provide a quantified description of this process, we do as following. For each image, we determine G, the center of mass of the cell in the sample plane denoted (X, Y). Then, in order to account for the potential coupling between the motility of the

[5]The migration experiments were performed in collaboration with C. Place at the Laboratoire de Physique, École Normale Supérieure de Lyon.

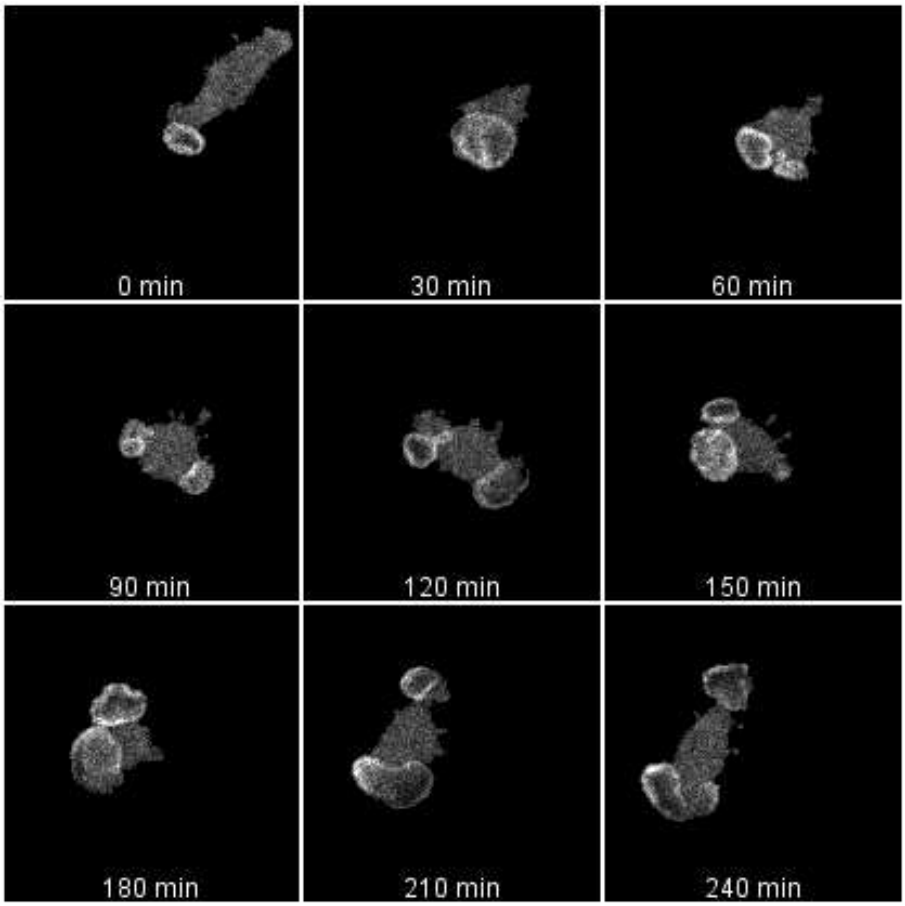

Figure 3.7: Nine instants of fluorescence image extracted from osteoclast migration. The formation of actin rings inside the cell accompanies the elongation of the cell in one given direction. When the length L is about twice its typical size (t = 120 min), we observe a 'jump' of the cell in the corresponding direction (t = 150–180 min). Subsequently, the cell elongates in the (almost) perpendicular direction due to the growth of two new actin rings (t = 210 min).

cell and the dynamics of the actin inside, we define the position P, characterizing the distribution of the actin inside the cell. We detail these two definitions in the following section.

3.4.1 Fluorescence image analysis

We denote M and N, the dimensions of the image in the directions m and n, respectively. We determine:

- the position (m_G, n_G) of the center of mass of a cell, G: From one raw fluorescence image I_{mn}, using an intensity threshold, we obtain a binary image B_{mn} of the cell such that $B_{mn} = 1$ if the indices m and n correspond to a point inside the cell and $B_{mn} = 0$

otherwise. By definition, we have

$$m_G = \frac{1}{NM} \sum_{n=1}^{N} \sum_{m=1}^{M} m.B_{mn} \tag{3.1}$$

and

$$n_G = \frac{1}{NM} \sum_{n=1}^{N} \sum_{m=1}^{M} n.B_{mn} \,. \tag{3.2}$$

- the position (m_P, n_P) of the actin structure, P, defined as following: From one raw fluorescence image, we define

$$m_P = \frac{1}{NM} \sum_{n=1}^{N} \sum_{m=1}^{M} m.I_{mn}^{\alpha} \tag{3.3}$$

and

$$n_P = \frac{1}{NM} \sum_{n=1}^{N} \sum_{m=1}^{M} n.I_{mn}^{\alpha} \,, \tag{3.4}$$

where the exponent α is introduced to increase the contrast. We checked that the experimental results do not depend significantly on α and report results obtained for $\alpha = 3$. Scaling factors are then applied to convert (m_G, n_G) and (m_P, n_P) to the positions (X_G, Y_G) and (X_P, Y_P) in the sample plane.

3.4.2 Cell and actin trajectories

From the center of mass of the cell G and the location of the actin P, we first define the vector $\vec{f} = \overrightarrow{GP}$, accounting for the distance and direction between G and P (figure 3.8).

Then, we report the trajectory of G during the whole experimental time (figure 3.9, diamonds and solid line). The first striking result is that the cell moves in a series of straight segments separated by spatially localized changes in direction. In order to get information about the dynamics, we report the velocity of the center of mass, V_G, as a function of time t (figure 3.10) and immediately note that V_G exhibits large peaks which repeat almost every 2 hours: the motion of cell occurs by almost periodic jumps during which the cell moves rapidly in a given direction. Note that each change in direction is associated with a jump event (figures 3.9 and 3.10).

3.4.3 Evolution of velocity of the center of mass V_G, distance f and cell length L

Reporting the trajectory of P in the (X, Y) plane (figure 3.9, squares and dashed line), we observe that G and P experience almost the same trajectories. To provide

information about the dynamics, we report the distance between G and P, $f = |\overrightarrow{GP}|$, as a function of time t (figure 3.10 b). We observe that f and the velocity of the cell V_G are also strongly correlated in time, a large peak in f preceding each large peak in V_G. The temporal correlation between V_G and f, and specially the delay τ between the peak in f and the peak in V_G can be assessed by calculating the cross-correlation function

$$\chi(t) = \int f(t' - t).V_G(t').dt' \,, \tag{3.5}$$

where the integral is estimated over the whole experimental time (figure 3.11). The cross-correlation $\chi(t)$ exhibits a maximum for $t = \tau \approx 10$ minutes whereas the oscillations point out the period of the cell motion, $T \approx 2$ hours: the cell jumps in a given direction every 2 hours, about 10 minutes after the distance f has reached a maximum, which proves the temporal correlation between $\vec{f}$ and $\vec{V}_G$.

In the same way, we report the cell length L as a function of time t (figure 3.10 c). We observe that the cell length L increases almost linearly between two successive jumps. The disappearance of one of the actin structures, on one side, leads to a peak in f (figure 3.10 b) when L is maximal. Thus, the displacements of the cell are strongly correlated to the dynamic of the actin inside the cell: the growth of actin rings in the contact region between the cell and the substrate induces an elongation of the cell. The disappearance of one of the structures, on one side, leads to a retraction of the cell toward the remaining structure which leads to a jump in the corresponding direction.

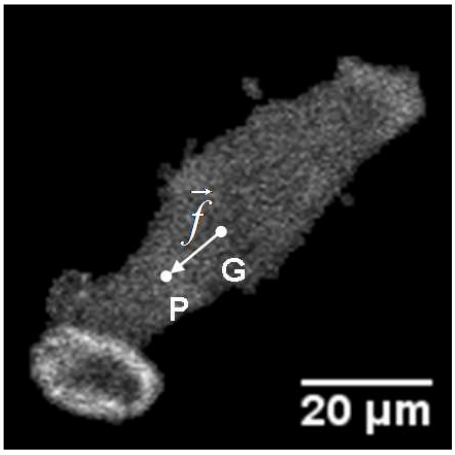

Figure 3.8: Fluorescence image of an osteoclast. The bright ring, on the left-hand side, corresponds to podosomes organized in a ring. From such images, we locate the center of mass of the cell, G, and the position of the actin structure, P, and define the vector $\vec{f} = \overrightarrow{GP}$.

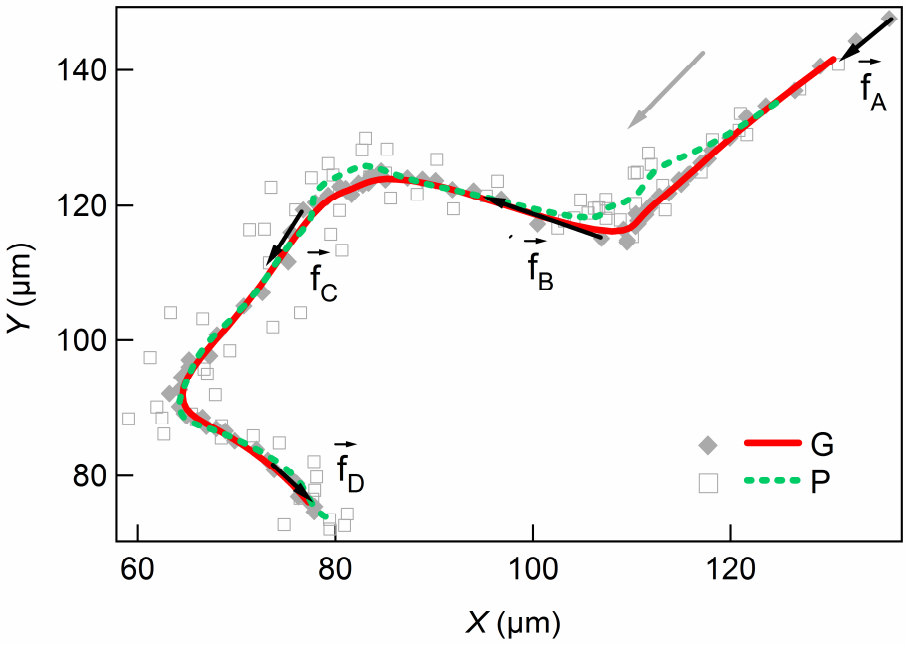

Figure 3.9: Cell and actin trajectories. Successive positions of the center of mass, G, and of the actin structure, P, in the sample plane (X, Y). The grey arrow indicates the direction of motion. The trajectories of G (full diamonds) and P (open squares) are strongly correlated. The continuous (resp. dashed) line corresponds to the trajectory of G (resp. P) averaged over 10 successive positions. The vectors $\vec{f}_A$, $\vec{f}_B$, $\vec{f}_C$ and $\vec{f}_D$ (black arrows) are associated with the events A, B, C and D (figure 3.10).

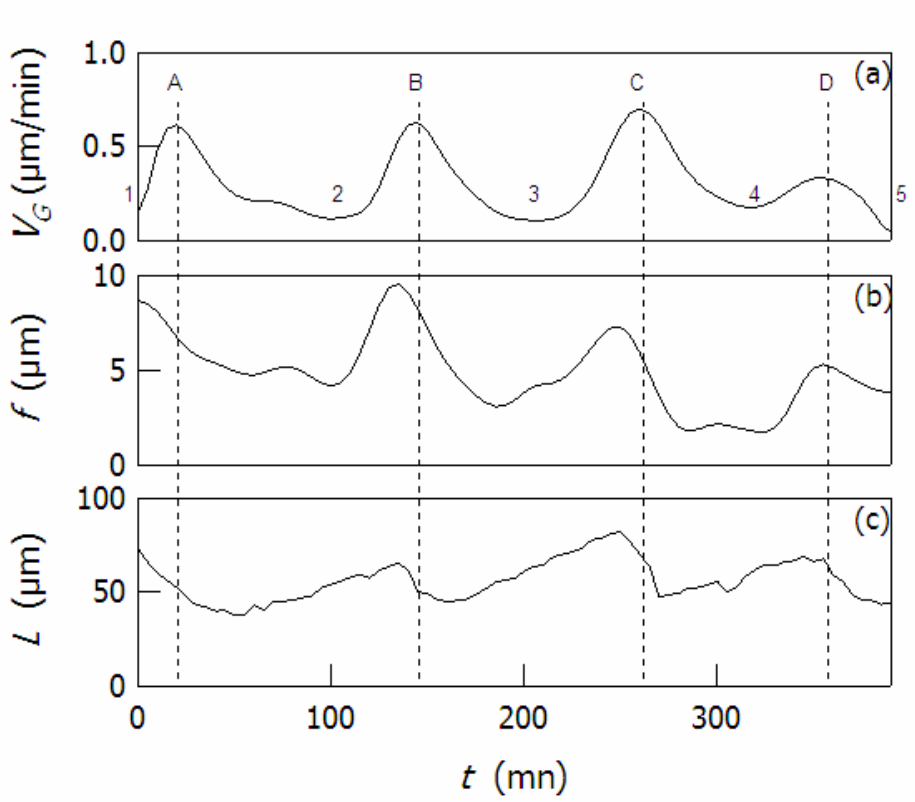

Figure 3.10: Velocity of the cell center of mass V_G, distance f and cell length L as a function of time t - (a): The velocity V_G exhibits peaks which correspond to the rapid motion of the cell in a given direction (jump). We number from 1 to 5 the minima in V_G. (b): The distance f interestingly exhibits the same type of temporal evolution. (c): The cell length L increases when the velocity of the cell is minimal and rapidly decreases during the jumps. One can notice that the cell jumps about 10 minutes after f or L have reached a maximum. We identify here 4 events, A, B, C and D. Successive jumps are separated by about 2 hours.

3.4.4 Direction of the jumps

Let us now consider the direction of the jumps. To do so, we identify the peaks A, B, C, and D, as defined in the figure 3.10, and the associated minima in the velocity numbered from 1 to 5 such that the peak A is associated with the jump from $G1$ to $G2$, etc. On the one hand, we denote $\vec{f}_A$, $\vec{f}_B$, $\vec{f}_C$ and $\vec{f}_D$, the values of $\vec{f}$ at the maximum in A, B, C and D. On the other hand, we denote $\Delta\vec{G}_{ij} = \overrightarrow{G_iG_j}$, the vector associated with the displacement of G during the jumps from i to j. Reporting the values of $\vec{f}$ at the maxima and the corresponding displacements $\Delta\vec{G}$ in the (X, Y) plane, we observe that these quantities are correlated in both length and direction (figure 3.12). In the inset (figure 3.12 a), we report the angle θ_P (resp. θ_G) between $\vec{f}$ (resp. $\Delta\vec{G}$) and the X–axis. We observe that $\theta_P \approx \theta_G$, which proves that the jumps occur in the direction of $\vec{f}$. In addition, considering the norms (figure 3.12 b), we observe that the amplitude $|\Delta\vec{G}|$ of the jumps is proportional to the length of $|\vec{f}|$: $|\Delta\vec{G}| \propto |\vec{f}|$. Note also that the directions of two successive jumps make an angle between them which is of about 90

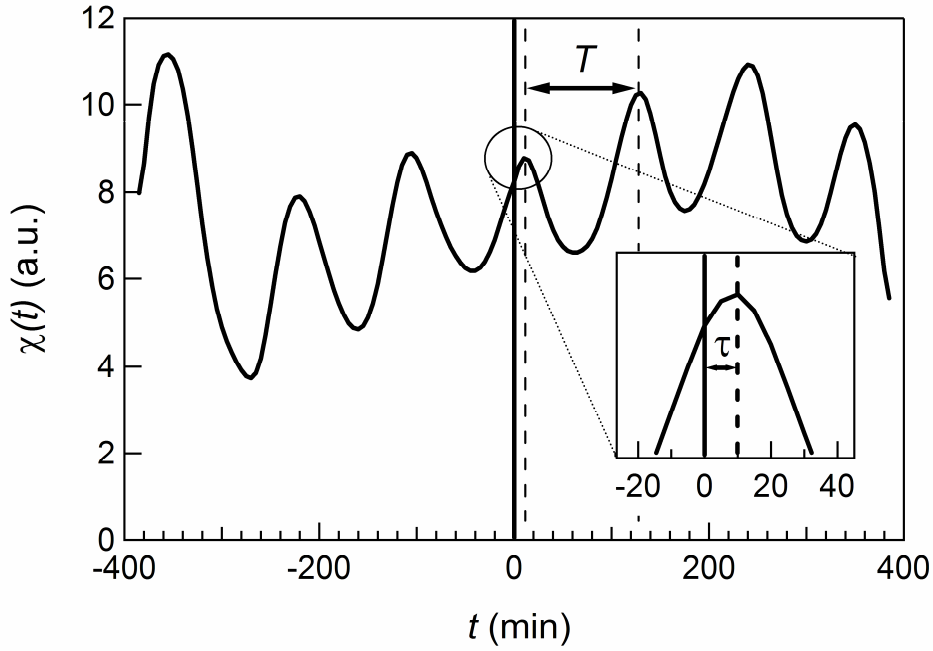

Figure 3.11: Temporal cross-correlation $\chi(t)$ between the cell velocity V_G and the distance f. The equally-spaced peaks confirm the almost periodic character of the jumps, with a period $T \approx 2$ hours. Inset: Enlargement of the highest peak. The correlation $\chi(t)$ is maximum for $t = \tau \approx 10$ minutes, which shows that the cell jumps about 10 minutes after f has reached a maximum.

degrees.

3.4.5 Discussion

This last experiment shows that the osteoclast 'jumps' follow the internal organization of the actin: the growth of actin rings induces the cell elongation. When the length L of the cell in the given direction is about twice its initial size, one of the actin structures disappears at one end. Subsequently, the cell retracts toward the remaining structure, which leads to a 'jump' of the cell in the given direction about 10 minutes after f (or L) has reached a maximum. The process repeats almost periodically every two hours. Thus, the cell motion occurs by almost periodic jumps, of the order of the cell size, during which the cell moves rapidly in a given direction. We also notice that the successive jumps make angles of about 90 degrees between them. The osteoclast exhibits a diffusion-like movement onto the substrate.

Considering that the cell jumps every 2 hours, 10 minutes after the distance between the actin structure and the center of mass of the cell has reached a maximum, in the direction pointed by $\vec{f}$, over a distance $|\Delta\vec{G}|$ proportional to $\vec{f}$, we can conclude that the actin dynamics does not only correlate with the cell migration, but drives it.

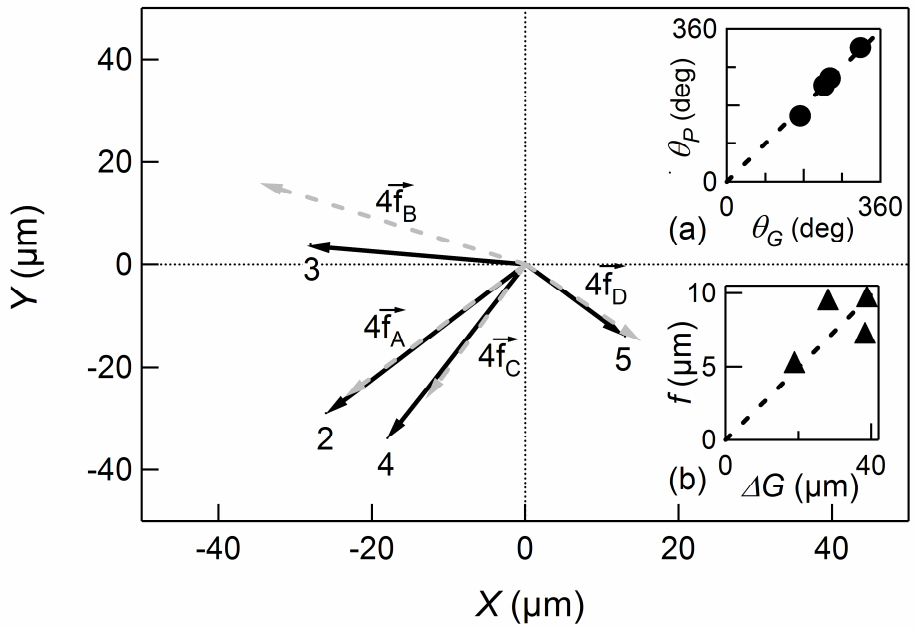

Figure 3.12: Vectors $\vec{f}_A$, $\vec{f}_B$, $\vec{f}_C$, $\vec{f}_D$ and associated displacements $\Delta\vec{G}$. The cell clearly jumps in the direction of P as pointed out by the strong correlation between $\vec{f}$ at the maximum (dashed grey arrows) and the associated $\Delta\vec{G}$ (full black arrows). (a): Angle θ_G vs angle θ_P (see text). The dashed line corresponds to the slope 1 showing that $\theta_G \approx \theta_P$. (b): Jump length ΔG vs. maximum distance f. The cell moves over a larger distance when the distance f at the maximum is larger.

From the observation of the substrate displacements, we conclude that the podosomal structure is subjected to a force. These results are compatible with previous investigations on BHK-RSV cells (Collin et al., 2008). Here, we propose that the podosomal structure is subjected to an internal tension which tends to extend the ring. In an opposite way, the substrate applies on the podosome line a force oriented inwards.

The motion of the cell involves its elongation which seems to be induced by the growth of actin rings. The actin structure thus seems to push the cell membrane outwards as already observed during the early adhesion process. One can then try to understand the underlying mechanism. From the observation of the substrate displacements, we concluded that the podosomal structure is subjected to an internal tension which tends to extend the ring. Thus, the formation and the growth of a podosome ring can account for the spreading of the contact region. Indeed, a podosome ring that encounters the cell periphery pushes the membrane outwards. One can guess that the process can take place until the membrane has reached its maximal possible extension (the cell is then flat). If two rings are pushing the cell in two opposite directions, the cell length increases until the weakest podosomal structures looses its mechanical stability because of excessive stress. Then, the latter structure disappears and the cell jumps in the direction of the most stable ring.

Let us discuss the potential mechanism inducing the cell motion. Assume first

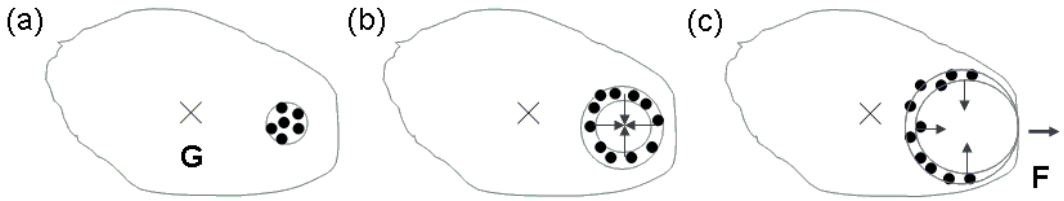

Figure 3.13: Sketch of podosomes evolution. The grey arrows indicate the force exerted by the podosome structure. (a): Podosomes cluster (b): Closed podosomes ring, the net force is zero. (c): Open ring, the net force F is oriented outward the cell. G indicates the cell center of mass.

that a podosome cluster nucleates randomly in the contact region between the cell and the substrate (figure 3.13 a). The cluster grows and then, after a few tens of minutes, forms a ring. As long as the ring is closed, the net force (integrated over the whole circumference) is zero (figure 3.13 b). After a given time, which depends on the growth velocity of the ring and of the distance from the nucleation site to the periphery of the contact region, the podosomes structure looses partly its stability in the region where the cell membrane is not in contact with the substrate. As a consequence, the net force F exerted by the structure onto the cell is non-zero, and oriented outward the cell (figure 3.13 c). The cell is therefore pushed in that direction, which releases the stress and leads to the disappearance of the podosomal structure. The whole process can then repeat again, leading to a subsequent motion of the cell in a random direction if the cluster nucleation is random.

Even if the proposed mechanism is based on many assumptions (the cell adheres to the substrate in the contact region, and the podosomal structure becomes unstable when the stress is released), it is compatible with the almost periodic, random in direction, motion of the cell in the direction of $\vec{f}$, the vector connecting the cell center of mass G and the position of the actin structure P: First, as explained above, the cell moves in the direction of $\vec{f}$; Second, the nucleation of the cluster occurring randomly in the contact region, one can estimate that the period T corresponds to the sum of the typical time T_n for a cluster to nucleate after the disappearance of the preceding ring, of the typical time T_c for the cluster to grow and form a ring, and of the time T_r needed for the ring to reach the periphery of the cell. From the experiments, we can estimate $T_n \approx 1$ hour, $T_c \approx 1/2$ hour whereas $T_r \approx 1/v \approx 25$ min where $l \approx 50$ μm is the typical distance between the nucleation site and the periphery of the cell (which compares to the typical size of the cell) and $v \approx 2$ μm/min the typical growth velocity of the ring.

Finally, let us discuss now the physical origin of the tension force. The individual podosomes are associated with a dense actin conical core formed by the cross-linked actin filaments, as demonstrated by SEM observation experiments (Luxenburg et al., 2007). However, the cores are dynamical structures growing from the base, the cell membrane. Considering the sketch in figure 3.14, one can easily see that, because of a

sterical frustration effect, the base of the cone tends to extend if the structure grows from the base and the filaments linked to each other. As a consequence, two neighboring podosomes tend to repel each other, which naturally leads to a negative tension force observed experimentally. In such a picture, podosomes induce the membrane tension.

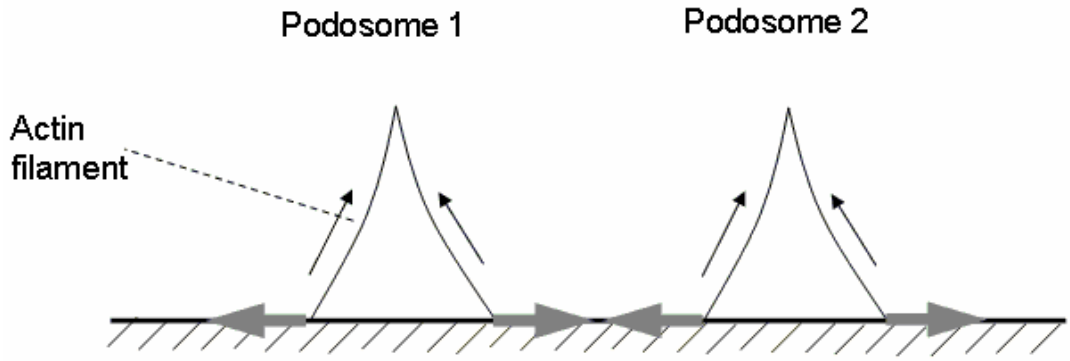

Figure 3.14: Growth and interaction of two neighboring podosomes. Black arrows denote the growth direction of actin filaments, while gray arrows represent the forces applied by the bind filaments on the substrate (see text).

Chapter 4

Internal dynamics of the actin in the podosome

Contents

Hu S., Biben T., Wang X., Jurdic P. & Géminard J.-C., Internal dynamics of actin structures involved in the cell motility and adhesion: modeling of the podosomes at the molecular level, *in revision at J. Theoretical Biol.* (August 2010).

4.1 Introduction

In the confocal microscope, the apparent shape of a podosome is a cone of typical height $h \simeq 0.5$ μm and base radius $r_p \simeq 0.15$ μm. It is made of a dense assembly of actin filaments, the *core*, preferably oriented along the perpendicular to the cell membrane (Luxenburg et al., 2007). Interestingly, FRAP (Fluorescence Recovery After Photobleaching) experiments have proven that podosomes are dynamical structures in spite of their stationary shape during their life-span which is about 2 min (Destaing et al., 2003): the podosomes grow during about 30 s before they reach an apparent steady-state during which the filaments continuously grow from the cellular membrane.

The mechanisms that regulate these structures are not known at present but probably involve actin regulators that are specifically found in podosomes, like cortactin and Wiskott-Aldrich syndrome protein (WASP), which localize directly underneath the podosome (Pfaff & Jurdic, 2001). Among them, the gelsolin, an actin severing agent, has been proven to be essential for the podosome regulation (Chellaiah et al., 2000; Akisaka et al., 2001; Kotadiya et al., 2008). Fluorescence experiments in which the actin and the gelsolin are marked by different fluorescent dyes show that the activity of the two molecules collocate: the concentration of the gelsolin is large in the podosome core as well as in the surrounding cloud (figure 4.1).

In a previous model, Biben et al. focused on the actin dynamics in the core and in the cloud (Biben et al., 2005). By reducing the complex biological system to a simplified model involving only the synthesis of actin filaments at the cell membrane and the severing, they accounted for the observed apparent shape of the single podosome and for experimental FRAP results, which proved that podosomes are dynamical structures (Biben et al., 2005). However, the previous model could not account for the colocalization of the gelsolin and actin fluorescence signals. In this study, we introduce, in addition to Biben et al.'s model, the equations governing the activity of the gelsolin molecule. We thus propose a far more complete model which explains why the concentration of the gelsolin is large in both the core and the cloud and we discuss the consequences for the dynamics of the podosomal structures.

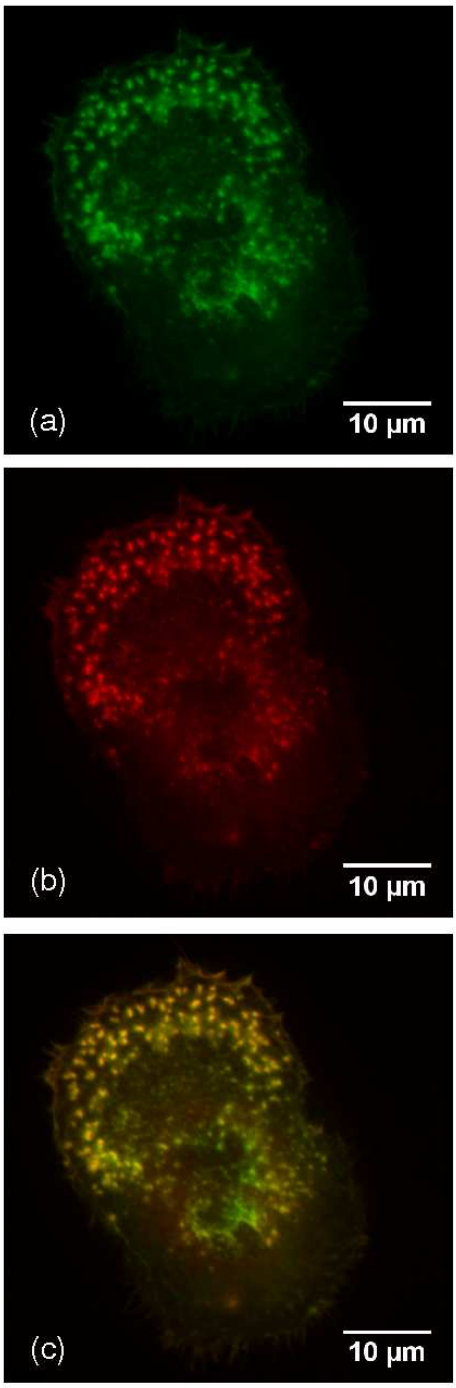

Figure 4.1: Colocalization of gelsolin and actin. The use of two dyes exhibiting different fluorescence wavelengths makes it possible to image separately the actin (a) and the gelsolin (b) in an osteoclast. (c): Overlap image of actin and gelsolin. Actin is in green, gelsolin is in red. The experiment clearly demonstrates the colocalization of the actin and gelsolin fluorescence signals in the podosome core [Fixed osteoclast observed in the Axioplan 2 Imaging fluorescence microscope (Zeiss): actin marked with Phalloidin (wavelength 488 nm) and gelsolin with Anti-Gelsolin binded with fluorescent second antibody (wavelength 562 nm)].

4.2 Model and definitions

Following the same idea as developed in Biben et al. (2005), we consider a podosome as a dense assembly of actin filaments, the *actin core*. The filaments are supposed to grow, from a nucleation site located at the cell membrane, by addition of monomers whereas their size is limited by the action of the severing molecule, the *gelsolin* (figure 4.2). The filaments that are released from the core diffuse freely in the *cytoplasm* (the intra cellular medium) and form the *actin cloud* (Destaing et al., 2003). In the cloud, the free filaments are subsequently cut by the gelsolin.

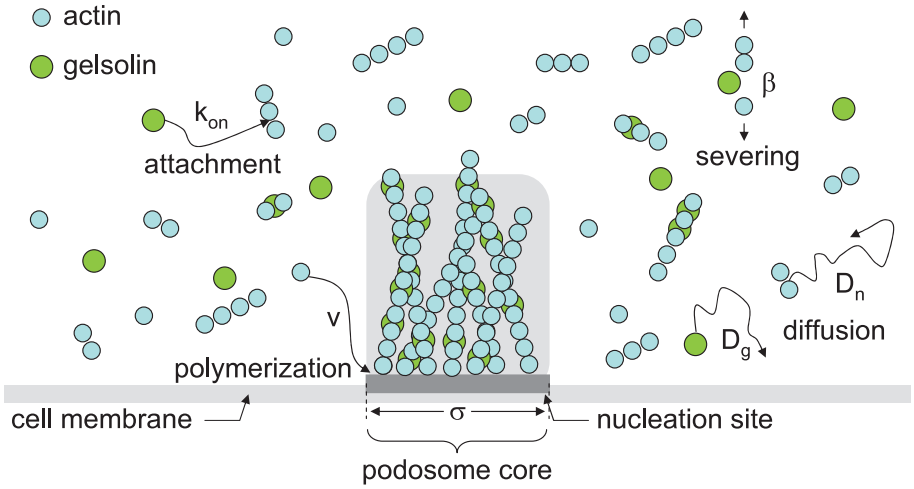

Figure 4.2: Sketch of the podosomal structure.

In order to account for the dynamics of the actin in the core, we consider the probability $b_n(t)$, at time t, for a filament attached to the nucleation site to consist of $(n+1)$ monomers, linked by n bonds. The number of filaments in the core is M and the typical radius of the structure at the membrane, σ (Note that no additional assumption about the geometrical arrangement of the filaments in the core is made). For the freely-diffusing filaments, we consider $c_n(\vec{r},t)$ the concentration, at time t and position $\vec{r}$, of the filaments which consist of $(n+1)$ monomers linked by n bonds. In accordance, $c_0(\vec{r},t)$ denotes the concentration of the freely-diffusing actin monomers.

In the core, the growth of the filaments is insured by the addition of actin monomers from a nucleation site with the frequency v. The growth velocity of the filaments is thus av, where a (~ 2.7 nm) denotes the diameter of the actin monomer. Seeking for simplicity, we will assume that the typical size σ of the nucleation site is small compared to the typical diffusion length so that the local concentration of the actin monomer, at time t, is $c_0(\vec{0},t)$, constant in the podosome core and, thus, that the polymerization frequency v, which might depend on c_0, is the same for all the filaments.

The severing of the actin filaments is due to the action of the gelsolin. The severing agent diffuses in the cytoplasm with the diffusion coefficient D_g and attaches to any

available bond between two actin monomers with the kinetic constant k_{on}. Once a bond is occupied by a gelsolin molecule, it is cut after the typical time $\tau \equiv 1/\beta$ and the gelsolin molecule is released in the cytoplasm. In order to account for the dynamics of the gelsolin, we consider its local concentration in the cytoplasm $g(\vec{r})$ and the probabilities $f_n(t)$, respectively $h_n(\vec{r},t)$, for one bond between two actin monomers in the core, respectively in the cytoplasm, to be occupied by a gelsolin molecule. For instance, with these notations, at time t and position $\vec{r}$, the total concentration of the gelsolin is $c_g \equiv g(\vec{r},t) + \sum_{n=1}^{\infty} n h_n(\vec{r},t) c_n(\vec{r},t)$.

The actin monomers and the filaments, when not attached to the core, diffuse in the cytoplasm. We denote D_0 the diffusion coefficient of the actin monomers. Following Einstein's prescription (Einstein, 1905), we can assume that the diffusion coefficient of an actin filament made of $(n+1)$ monomers, free of gelsolin molecule ($h_n = 0$), decreases with its molecular weight according to $D_n = D_0/(n+1)$. When gelsolin molecules are attached to the filament, we can accordingly assume that:

$$D_n \equiv \frac{D_0}{1 + n(1 + \alpha h_n)}, \tag{4.1}$$

where $\alpha \equiv m_g/m_a \simeq 2.1$ is the ratio of the mass $m_g \simeq 90$ kDa of the gelsolin molecule to the mass $m_a \simeq 43$ kDa of the actin monomer (Alberts et al., 1994).

4.3 Set of equations governing the dynamics

In the present section, we shall establish the set of equations governing the dynamics of the distribution b_n, diffusion fields, g and c_n, as well as of the probabilities, f_n and h_n, which account for the dynamics of the podosome core and surrounding cloud.

4.3.1 The core

The internal dynamics of the actin core is accounted for by the distribution $b_n(t)$ of the filament length and the probability f_n which describes the occupation of the bonds by the gelsolin molecule.

Taking into account the polymerization at the nucleation site and the severing, the equation governing the temporal evolution of the distribution $b_n(t)$ is given by:

$$\frac{db_n}{dt} = v(b_{n-1} - b_n) - \beta n f_n b_n + \beta \sum_{k=n+1}^{\infty} f_k b_k \tag{4.2}$$

The first term accounts for the growth of the filaments due to the polymerization which results in an advection of the distribution toward larger n with the frequency v. The two additional terms account for the severing: First, $b_n(t)$ is decreased because filaments of size n are cut at any of the nf_n occupied bonds with the characteristic

frequency β; second, $b_n(t)$ increases when any filament of size k, larger than n, whose $(n+1)^{\text{th}}$ bond (counted from the membrane) is occupied by a gelsolin molecule (which occurs with the probability f_k) is cut, at that specific position, after the time $1/\beta$.

The dynamics of the fraction f_n is more difficult to account for and, in order to make the result understandable, we shall detail the contributions of the various mechanisms. Consider the variation of the number, nf_nb_n, of gelsolin molecules attached to a filament having the size n. The addition of a monomer at the base does not change the number of gelsolin molecules so that the contribution of the polymerization is:

$$\frac{d}{dt}(nf_nb_n)\Big|_{pol.} = v(n-1)f_{n-1}b_{n-1} - vnf_nb_n \tag{4.3}$$

The severing of a filament having the size n, at any of its occupied bonds, leads to the loss of the number nf_n of gelsolin molecules for the considered population, so that the first contribution of the severing is:

$$\frac{d}{dt}(nf_nb_n)\Big|_{sev.1} = -(\beta nf_n)nf_nb_n \tag{4.4}$$

where the prefactor (βnf_n) takes into account that the filament is likely to be cut at nf_n bonds with the characteristic time $1/\beta$. The severing of a filament having the size k, larger than n, at the $(n+1)^{\text{th}}$ bond, leads to a filament of size n whose bonds are occupied by a gelsolin molecule with the probability f_k, so that the second contribution of the severing is:

$$\frac{d}{dt}(nf_nb_n)\Big|_{sev.2} = \sum_{k=n+1}^{\infty}(\beta f_k)nf_kb_k \tag{4.5}$$

where the prefactor (βf_k) accounts for the fact that the $(n+1)^{\text{th}}$ bond is occupied with the probability f_k and cut with the characteristic time $1/\beta$ if so. Finally, the gelsolin molecules that are in solution, in the vicinity of the core, attach to the available bonds [number $n(1-f_n)$] with the characteristic time $k_{on}g_0$, where g_0 is the local concentration of the gelsolin at the podosome core, which leads to:

$$\frac{d}{dt}(nf_nb_n)\Big|_{att.} = (k_{on}g)n(1-f_n)b_n \tag{4.6}$$

Summing all the contributions listed in the Eqs. (4.3) to (4.6), we get the equation governing the dynamics of f_nb_n

$$\frac{d}{dt}(nf_nb_n) = v[(n-1)f_{n-1}b_{n-1} - nf_nb_n] - \beta n^2f_n^2b_n + \beta n\sum_{k=n+1}^{\infty}f_k^2b_k + k_{on}g_0n(1-f_n)b_n \tag{4.7}$$

The coupled equations (4.2) and (4.7) govern the dynamics of the distribution b_n and of the fraction f_n. We point out that Eqs. (4.2) and (4.7) couple the internal dynamics of the core with that of the diffusion fields in the cloud through the local concentration of the gelsolin g_0 and the velocity v which might depend on the local concentration of the actin monomer c_0.

4.3.2 The cloud

The dynamics of the cloud can be accounted for by considering, in addition to the severing, the diffusion of the various species in solution. Before we establish the boundary conditions, we first consider the concentration of the gelsolin, g, the concentration of the actin monomers and filaments, c_n, and then the fraction of occupied bonds, h_n.

The gelsolin molecules, on the one hand, diffuse with the diffusion coefficient D_g, detach from the bond when a filament is cut and attach to the available bonds of the filaments in solution. Thus, because of the severing process, the diffusing filaments constitute volume sources and sinks and the field $g(\vec{r},t)$ is governed by:

$$\frac{\partial g}{\partial t} = D_g \Delta g + \beta \sum_{k=1}^{\infty} h_k k c_k - k_{on} g \sum_{k=1}^{\infty} [1-h_k] k c_k \tag{4.8}$$

where Δ denotes the Laplacian operator.

At the same time, the filaments diffuse in the cytoplasm, are cut with the characteristic time $1/\beta$ at any of the $nh_n(\vec{r},t)$ occupied bonds, so that:

$$\frac{\partial c_n}{\partial t} = \vec{\nabla}.[D_n \vec{\nabla} c_n] - \beta n h_n c_n + 2\beta \sum_{k=n+1}^{\infty} h_k c_k \tag{4.9}$$

Note that the diffusion coefficient depends on space. Indeed, D_n depends on the fraction of bonds occupied by the gelsolin (Eq. 4.1). The factor 2 in the last term is due to the fact that there are two possibilities for getting a filament of size n when cutting a larger filament. Finally, we mention that the equation (4.9) holds true for the monomer and that we get for $n = 0$:

$$\frac{\partial c_0}{\partial t} = D_0 \Delta c_0 + 2\beta \sum_{k=1}^{\infty} h_k c_k \tag{4.10}$$

The dynamics of the fraction h_n is again more difficult to account for and we shall detail the contributions of the various mechanisms. We consider the contributions of all the mechanisms that induce a variation of the number nh_nc_n, in the unit volume, of gelsolin molecules attached to the filaments of size n. The filaments diffuse and carry, each, a number $nh_n(\vec{r},t)$ molecules:

$$\frac{\partial}{\partial t}(nh_nc_n)\Big|_{diff.} = \vec{\nabla}.(nh_n D_n \vec{\nabla} c_n) \tag{4.11}$$

Again, the diffusion does not reduce to a simple Laplacian equation, not only because the diffusion coefficient depends on space and time but also because the number of gelsolin molecules on the filaments depends on space and time. In addition, the severing of the filaments having the length n leads, on the one hand, to the decrease of the local concentration of the gelsolin attached to the filaments of size n according to:

$$\frac{\partial}{\partial t}(nh_nc_n)\Big|_{sev.1} = -\beta n^2 h_n^2 c_n \tag{4.12}$$

Indeed, $nh_n(\vec{r},t)$ gelsolin molecules are attached to the filament which is thus cut with the frequency $\beta n h_n(\vec{r},t)$, $nh_n(\vec{r},t)$ gelsolin molecules being transfered to smaller filaments or released in solution. On the other hand, the severing of larger filaments ($k > n$), at two specific positions occupied with the probability $h_k(\vec{r},t)$, leads to a filament of size n and provides $nh_k(\vec{r},t)$ gelsolin molecules:

$$\frac{\partial}{\partial t}(nh_nc_n)\Big|_{sev.2} = \sum_{k=n+1}^{\infty} \beta(nh_k)(2h_k)c_k \tag{4.13}$$

Finally, free gelsolin molecules attach to the filaments at the available bonds:

$$\frac{\partial}{\partial t}(nh_nc_n)\Big|_{att.} = k_{on}gn(1-h_n)c_n \tag{4.14}$$

From the contributions Eqs. (4.11) to (4.14), we get the equation governing the product h_nc_n:

$$\frac{\partial}{\partial t}(nh_nc_n) = \vec{\nabla}.[nh_nD_n\vec{\nabla}c_n] - \beta n^2h_n^2c_n + 2\beta n\sum_{k=n+1}^{\infty} h_k^2c_k + k_{on}gn[1-h_n]c_n \tag{4.15}$$

The equations (4.2) and (4.7) govern the dynamics of the distribution $b_n(t)$ and of the fraction $f_n(t)$ in the core whereas the equations (4.8), (4.9) and (4.15) govern the dynamics of $c_n(\vec{r},t)$ and $g(\vec{r},t)$, the actin and gelsolin concentration fields, and the fraction $h_n(\vec{r},t)$ in the cloud.

4.3.3 The boundary conditions

Due to the polymerization, the core acts as a sink of monomeric actin whereas, due to the severing, it acts as a source of both actin monomers and filaments. In the same way, due to the attachment to the available bonds, the core acts as a sink of gelsolin molecules but, due to the severing process, is a source of gelsolin, free or attached to diffusing filaments. In order to account for these sources and sinks, we shall write the boundary conditions at the core, supposed to be centered in $\vec{r} = \vec{0}$.

Diffusing filaments are released in solution when filaments of the core are cut at the appropriate bond whereas, the total number of filaments in the core being M and v monomers being added per unit time, Mv monomers are consumed:

$$\int_S D_n(\vec{\nabla}c_n).d\vec{S} = Mv\,\delta(n) - M\beta\sum_{k=n+1}^{\infty} f_kb_k \tag{4.16}$$

where S is a surface enclosing the core and, $d\vec{S}$ the surface element oriented outwards. The diffusion coefficient, which depends on $h_n(\vec{r},t)$, is evaluated at the boundary. The first term on the right-hand side accounts for the consumption of monomers (δ stands for the Kronecker delta function) due to the polymerization.

The severing of a longer filament ($k > n$) in the core, after a time $1/\beta$ if the bond is occupied (which occurs with the probability f_k) releases in solution nf_k gelsolin molecules which then diffuse attached to the filament:

$$\int_S nh_n D_n(\vec{\nabla} c_n).d\vec{S} = -nM\beta \sum_{k=n+1}^{\infty} f_k^2 b_k. \tag{4.17}$$

Finally, per unit time, $k_{on}g_0$ gelsolin molecules attach to any available bond in the core [$g_0 \equiv g(0,t)$ stands for the gelsolin concentration at the core] whereas one molecule is released in solution each time a bond is cut:

$$D_g \int_S \vec{\nabla} g.d\vec{S} = -M\beta \sum_{n=1}^{\infty} nf_n^2 b_n + Mk_{on}g_0 \sum_{n=1}^{\infty} n(1-f_n)b_n \tag{4.18}$$

Far away from the core, the concentration of any filament vanishes, whereas the concentrations of the monomers and of the gelsolin tend respectively to the overall concentrations c_0^∞ and g^∞:

$$\lim_{r\to\infty} c_n(\vec{r},t) = c_0^\infty \delta(n) \tag{4.19}$$

$$\lim_{r\to\infty} g(\vec{r},t) = g^\infty \tag{4.20}$$

We mention also that, accordingly, the concentration of gelsolin molecules attached to filaments of size n also vanishes so that $\lim_{r\to\infty}(nh_n c_n) = 0$ $(\forall n)$.

4.4 Parameters of the problem

From now on, it is particularly interesting to consider the parameters of the problem. First, the equation governing the internal dynamics of the core [Eqs. (4.2) and (4.7)] suggest that the pertinent timescale is $\tau = 1/\beta$ whereas the equation governing the actin diffusion field [Eqs. (4.9) and (4.15)] suggest that the pertinent length-scale is $\sqrt{D_0/\beta}$. We shall thus report results expressed in terms of the dimensionless variables $\tilde{t} \equiv \beta t$ and $\tilde{r} \equiv r\sqrt{\beta/D_0}$. Second, one can consider that the pertinent concentration scale is the concentration of the actin far away from the core so that one can express all the concentrations relative to c_0^∞. We thus define, for instance, $\tilde{c}_n = c_n/c_0^\infty$ and $\tilde{g} = g/c_0^\infty$.

The remaining independent parameters of the problem are α, D_g, g^∞, M, σ, k_{on} and the function v. The parameter α is the ratio of the gelsolin and actin molecular weights which plays a role in the dependency of D_n on h_n. We define $d \equiv D_g/D_0$, $\gamma \equiv g^\infty/c_0^\infty$ and $\zeta \equiv k_{on}g^\infty/\beta$ in accordance with the choice of the dimensionless variables. The parameters M and σ account for the surface density of the actin filaments inside

the podosome core. Indeed, assuming that $\sigma \ll \sqrt{D_0/\beta}$ one can consider that the surface in the boundary conditions [Eqs. (4.16) to (4.18)] is a sphere of radius $\sigma/2$. Assuming then radial diffusion fields, one exhibits the dimensionless parameter $\Phi \equiv (2M/\pi\sigma^2)/(\sqrt{D_0/\beta}\, c_0^\infty)$ which compares the density of the filaments in the core with the surface density of the actin monomer in a layer of thickness $\sqrt{D_0/\beta}$.

4.5 Steady-state solution

We shall first study the steady-state solution to the problem and then discuss the characteristic time associated with the dynamics of the system. The solutions of the problem are calculated numerically.

4.5.1 The core

The internal dynamics of the core, governed by the equations (4.2) and (4.7), is coupled to the cloud only by the velocity v which might depend on the local concentration of the actin monomer and by the local concentration of the gelsolin, g_0. Thus, it is pertinent to consider the steady-state solution for given $v^* \equiv v/\beta$ and $\zeta_0 \equiv k_{on} g_0/\beta$. We define and report the podosome size, $\overline{n} \equiv \sum_{n=0}^{\infty}(n+1)b_n$, and the average fraction of gelsolin on the filaments in the core, $f_g \equiv (\sum_{n=0}^{\infty} n f_n b_n)/(\sum_{n=0}^{\infty} n b_n)$ (Fig. 4.3). We find numerically that f_g and $\overline{n}/\sqrt{\pi v^*/2}$ are functions of $\zeta_0/\sqrt{v^*}$ which can be understood as the product of the attachment characteristic frequency $k_{on} g_0$ and of the characteristic time of the core growth $\tau_{core} \equiv 1/\sqrt{\beta v}$ ($\propto \overline{n}/v^*$). For $\zeta_0/\sqrt{v^*} \gg 1$, the gelsolin tends to occupy all the bonds so that $f_g \simeq 1$ and $\overline{n} \simeq \sqrt{\pi v^*/2}$ as it was already demonstrated analytically by Biben et al. (2005). For smaller $\zeta_0/\sqrt{v^*}$, the concentration $f_g < 1$, which leads to a less effective severing process and, accordingly, to a larger typical core size $\overline{n}$.

Thus, the characteristics of the podosome core do not depend drastically on the local concentration of the gelsolin, g_0. Indeed, changing ζ_0 by a factor 10^4 (from 100 to 0.01) changes $\overline{n}$ by a factor 5 only. By contrast, $\overline{n} \propto v^{*1/2}$ and, thus, the characteristic time of the podosome growth, $\tilde{\tau}_{core} \sim v^{*-1/2}$ drastically depend on the polymerization velocity which might depend on the local concentration of the actin monomer.

4.5.2 The cloud

The dynamics of the actin and of the gelsolin in the surrounding core is governed by the equations (4.8), (4.9) and (4.15). The podosome core, assumed to be centered in $\vec{r} = \vec{0}$, is accounted for by the boundary conditions (4.16) to (4.20). We define and report the total concentration of the actin monomer, $c_a \equiv \sum_{n=0}^{\infty}(n+1)c_n$, and of the gelsolin, $c_g \equiv g + \sum_{n=0}^{\infty} n h_n c_n$, as functions of the distance r from the podosome core (Fig. 4.4). We note that both the actin and the gelsolin accumulate around the

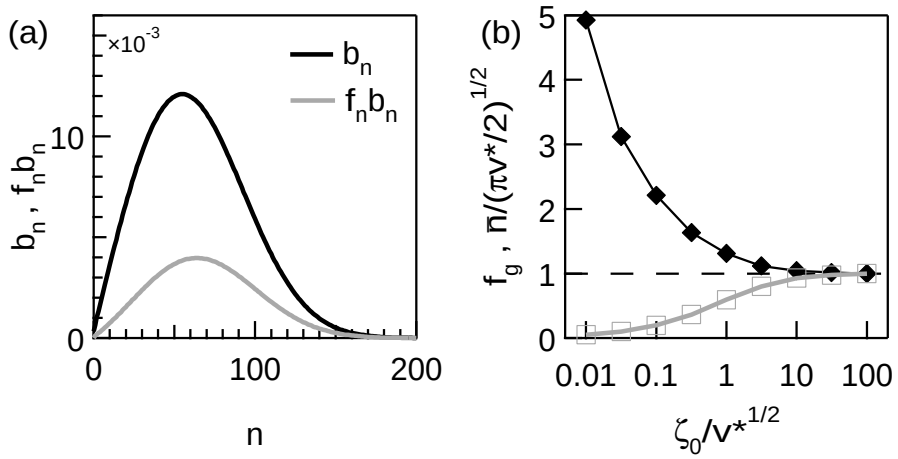

Figure 4.3: Typical solution for the podosome core - (a) Typical b_n and $f_n b_n$ ($v^* = 1000$, $\zeta_0 = 10$). (b) Fraction f_g (open squares) and normalized size $\overline{n}/\sqrt{\pi v^*/2}$ (full diamonds) vs. $\zeta_0/\sqrt{v^*}$.

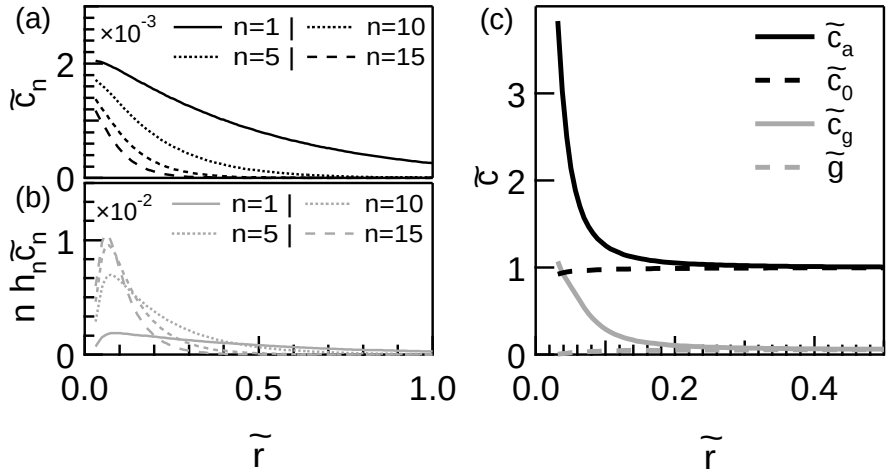

Figure 4.4: Typical solution for the cloud - (a) Concentration of the actin filaments $\tilde{c}_n$ in the cloud. (b) Concentration $nh_n\tilde{c}_n$ of gelsolin binded to the filaments of size n in the cloud. (c) Total concentrations of the gelsolin $\tilde{c}_g$ and of the actin $\tilde{c}_a$ in the cloud around the core. One can notice that, in spite of the small concentration of gelsolin far away from the podosome ($\gamma = 5.855\ 10^{-2}$), the concentrations of the actin and of the gelsolin in the core region are of the same order ($v^* = 1000$, $\zeta_0 = 10$, $\alpha = 0$, $d = 1$, $\phi = 2.516\ 10^{-3}$, $\zeta = 1.171\ 10^2$ and $\gamma = 5.855\ 10^{-2}$. These parameters insure $\zeta_0 = 10$ which corresponds to the core described in Fig. 4.3).

core in a region having a dimensionless radius, denoted $\tilde{r}_c$, which is governed by the competition between the diffusion and the severing: The typical diffusion-coefficient is of the order of $D_0/\overline{n}$ whereas the typical severing frequency is about $\overline{n}\beta$. Considering that r_c is of the order of the associated diffusion lengh $\sqrt{D_0/\beta}/\overline{n}$, we get $r_c \sim \sqrt{D_0/v}$

and, thus, $\tilde{r}_c \sim 1/\sqrt{v^*}$. Interestingly, considering the dynamics, one can estimate the time necessary to establish the steady-state diffusion field to be of the order of $\tau_{cloud} \sim r_c^2/(D_0/\overline{n})$ so that $\tilde{\tau}_{cloud} \sim \tilde{\tau}_{core}$. Thus, provided that the polymerization frequency v is given, the dynamics of the whole system involves a single characteristic time $\tau = 1/\sqrt{\beta v}$. We point out that, the typical number $\overline{n}$ being a slowly varying function of the the gelsolin concentration at the core, the typical size and, thus, the characteristic time associated with the cloud dynamics depend only slowly on the local concentration of the gelsolin.

4.6 Discussion

The model, which involves the polymerization of actin filaments at the cell membrane and the diffusion and attachment kinetics of the gelsolin, accounts for the observation of large concentrations of the actin and of the gelsolin in the podosome region, in both the core and the cloud. Moreover, the model predicts that the characteristics of the podosome, typical size and characteristic time, are not sensitive to the local concentration of the gelsolin. The system is mainly governed by the dynamics of the actin. The interplay between the gelsolin and actin concentration fields is accounted for by the model. The dependency of the polymerization frequency on the local concentration of actin at the core and the interaction between cores through the diffusion fields in the cloud might explain the collective dynamics of the system. The formation and the migration of podosome rings in the framework of the present model shall be investigated in the near future.

Conclusions and perspectives

The study of the osteoclast adhesion process requires information on the role played by the physical (rigidity, rugosity,...) or chemical properties of the substrate. In the first part (chapter 2), we performed kinetic measurements at the cell scale, measured the evolution of the number of nuclei K and the cell surface area A as a function of time for cells attaching to rigid substrates presenting different chemical properties (plastic, ITO, pure glass). We found that the surface area of the contact region between the cell and the substrate scales as $A \sim K^2$. This scaling indicates that the osteoclasts exhibit a flat morphology, which had been observed but, up to now, not quantified. The unusual exponent 2 is responsible for the partition of the cell population: at long times, a group of large cells appear. Defining quantities that account for the spatial distribution of the actin within the cell, we demonstrated that the podosome organization only depends on the time after differentiation and not on the number of nuclei K. We observed almost no dependence on the chemical properties of the substrates used for our experiments. In appendix A, we performed complementary experiments on substrates of different physical properties (different topographies). We did not observe any significant difference on the podosomes structure.

In the second part (chapter 3), we presented a series of experiments performed in order to decipher the role played by the podosomes during osteoclasts adhesion and motility. The observations that osteoclasts are adherent even if they do not exhibit podosomes lead us to propose that podosomes do not play a direct role in cell adhesion. During osteoclast movement, however, we observed a strong coupling between cell spreading and podosomes formation. It lead us to propose that podosomes might play a role in osteoclast motility. We therefore performed other experiments to deeply investigate the functions of podosomes in osteoclast motility. At short time, we investigated the force applied by the osteoclast onto the substrate. We conclude that the podosomal structure is subject to an internal tension which tends to extend the ring and push the cell membrane outwards. At longer time, the study of a single osteoclast migration points out that the motion of the cell is related to the collective organization of the actin. The osteoclast migrates by successive jumps, which follow the internal actin organization. The whole set of podosomes dynamics experimental results suggests that, even if the podosomes are not necessary for the cell to adhere to the substrate, the internal dynamics of the actin within the cell does not only correlate with cell migration, but drives it. During the migration, podosomes appear at the periphery of the spreading area whereas they disappear from the retracting regions. Podosomes are

present in area where tension forces are applied.

In the last part (chapter 4), we developed a model describing the internal dynamics of a single podosome, by taking into account the presence of gelsolin, an actin severing agent, present at large concentration in the podosome region. The model, which involves the polymerization of actin filaments as well as the diffusion and attachment kinetics of the gelsolin, predicts that the characteristics of the podosome, typical size and characteristic time, are not sensitive to the local concentration of the gelsolin. The system is mainly governed by the dynamics of the actin.

This work brought some informations on podosomes dynamics and functions, but many questions remain unanswered. It is commonly believed that podosomes are involved in osteoclast adhesion process. Our experimental results suggest the contrary. A deeper investigation of this process is necessary to solve the debate. More experiments on the role of podosomes in cell motility would also be required. One of the main conclusion of this study is that podosomes drive cell migration. In a recent study, however, Yang et al. (2009) suggested that the membrane deforms by its own mechanisms, and growing actin filaments just fill the space created by the protrusion, in order to stabilize it. We could only obtain few data on the deformation of soft (gel) substrate by podosomes. It would be interesting not only to perform more measurements, but also to access the force field generated by the podosomes.

Finally, we pointed out that the physical and chemical properties of the substrate did not seem to affect the podosomes structure. Preliminary results, however, show that the osteoclast morphology depends strongly on the substrate topography (appendix A). The investigation of osteoclasts migration on a patterned substrate will surely help to increase the knowledge of podosomes dynamics.

References

Abramoff, M., Magelhaes, P., & Ram, S. (2004). Image Processing with ImageJ. *Biophotonics Internationa*, *11*(7), 36–42.

Akisaka, T., Yoshida, H., Inoue, S., & Shimizu, K. (2001). Organization of cytoskeletal F-actin, G-actin, and gelsolin in the adhesion structures in cultured osteoclasts. *J. Bone Miner. Res.*, *16*, 1248–1255.

Alberts, B., Bray, D., Lewis, L., Raff, M., Roberts, K., & Watson, J. (1994). *Molecular Biology of the Cell, 3rd Ed.* New-York: Garland Publishing. (845 p.)

Alberts, B., Johnson, A., Lewis, J., Raff, M., Roberts, K., & Wlater, P. (2002). *Molecular Biology of the Cell, Fourth Edition.* New York: Garland Science. (p908, 931, 973-975.)

Astroem, P., Kumar, B., Vattulainen, I., & Karttunen, M. (2008). Strain hardening, avalanches, and strain softening in dense cross-linked actin networks. *Phys. Rev. E*, *77*, 051913.

Bacabac, R., Mizuno, D., Schmidt, C., MacKintosh, F., Van Loon, J., & J. Klein-Nulend, T. S. (2008). Round versus flat: Bone cell morphology, elasticity, and mechanosensing. *J. Biomech.*, *41*(7), 1590–1598.

Bausch, A., & Kroy, K. (2006). A bottom-up approach to cell mechanics. *Nat. Phys.*, *2*, 231–238.

Beningo, K., Lo, C., & Wang, Y. (2002). Flexible polyacrylamide substrata for the analysis of mechanical interactions at cell-substratum adhesions. *Methods Cell Biol.*, *69*, 325–339.

Bereiter-Hahn, J. (2005). Mechanics of crawling cells. *Med. Eng. Phys.*, *27*, 743–753.

Berro, J., Michelot, A., Blanchoin, L., Kovar, D., & Martiel, J.-L. (2007). Attachment conditions control actin filament buckling and the production of forces. *Biophys. J.*, *92*, 2546–2558.

Biben, T., Géminard, J.-C., & Melo, F. (2005). Dynamics of bio-polymeric brushes growing from a cellular membrane: tentative modelling of the actin turnover within an adhesion unit; the podosome. *J. Biol. Phys*, *31*, 87–120.

Block, M., Badowski, C., Millon-Fremillon, A., Bouvard, D., Bouin, A., Faurobert, E., et al. (2008). Podosome-type adhesions and focal adhesions, so alike yet so different. *J. Cell Biol.*, *87*, 491–506.

Boyle, W., Simonet, W., & Lacey, D. (2003). Osteoclast differentiation and activation. *Nature*, *423*, 337–342.

Brooks, F., & Carlsson, A. (2009). Non-equilibrium actin polymerization treated by a truncated rate-equation method. *Phys. Rev. E*, *79*, 031914.

Brooks, F., & Carlsson, A. (2010). Actin polymerization overshoots induced by plus-end capping. *Phys. Biol.*, *7*, 16008.

Burgess, T., Qian, Y., Kaufman, S., Ring, B., Van, G., Capparelli, C., et al. (1999). The ligand for osteoprotegerin (OPGL) directly activates mature osteoclasts. *J. Cell Biol.*, *145*, 527–538.

Chabadel, A. (2007). *Structures, stabilité et fonctions du cytosquelette d'actine dans les ostéoclastes mâtures.* Unpublished doctoral dissertation, Ecole Normale Supérieure de Lyon. (153 p.)

Chabadel, A., Rodríguez, I. non, Cluet, D., Rudkin, B., Wehrle-Haller, B., Genot, E., et al. (2007). D44 and β3 integrin organize two functionally distinct actin-based domains in osteoclasts. *Mol. Biol. Cell*, *18*(12), 4899–4910.

Chellaiah, M., Kizer, N., Silva, M., Alvarez, U., Kwiatkowski, D., & Hruska, K. (2000). Gelsolin deficiency blocks podosome assembly and produces increased bone mass and strength. *J. Cell Biol.*, *148*, 665–678.

Chen, W. (1989). Proteolytic activity of specialized surface protrusions formed at rosette contact sites of transformed cells. *J. Exp. Zool.*, *251*, 167–185.

Collin, O., Na, S., Chowdhury, F., Hong, M., Shin, M., Wang, F., et al. (2008). Self-organized podosomes are dynamic mechanosensors. *Curr. Biol.*, *18*, 1288–1294.

Collin, O., Tracqui, P., Stephanou, A., Usson, Y., Clément-Lacriox, J., & Planus, E. (2006). Spatiotemporal dynamics of actin-rich adhesion microdomains: influence of substrate flexibility. *J. Cell Sci.*, *119*, 1914–1925.

Conti, E., & MacKintosh, F. (2009). Cross-linked networks of stiff filaments exhibit negative normal stress. *Phys. Rev. Lett.*, *102*, 088102.

Cooper, J. (1987). Effects of cytochalasin and phalloidin on actin. *J. Cell Biol.*, *105*(4), 1473–1478.

Damljanovic, V., Lagerholm, B., & Jacobson, K. (2005). Bulk and micropatterned conjugation of extracellular matrix proteins to characterized polyacrylamide substrates for cell mechanotransduction assays. *Biotechniques*, *39*, 847–851.

David-Pfeuty, T., & Singer, S. (1980). Altered distributions of the cytoskeletal proteins vinculin and *alpha*-actinin in cultured fibroblasts transformed by Rous sarcoma virus. *Proc. Natl. Acad. Sci. USA*, *77*(11), 6687–6691.

DeFife, K., C.R.Jenney, Colton, E., & Anderson, J. (1999). Cytoskeletal and adhesive structural polarizations accompany IL-13induced human macrophage fusion. *J. Histochem. Cytochem.*, *47*, 4765–4774.

Destaing, O., Saltel, F., Géminard, J.-C., Jurdic, P., & Bard, F. (2003). Podosomes display actin turnover and dynamic self-organization in osteoclasts expressing actin-green fluorescent protein. *Mol. Biol. Cell*, *14*, 407–416.

Downey, P., & Siegel, M. (2006). Bone biology and the clinical implications for osteoporosis. *Phys. Ther.*, *86*, 77–91.

Einstein, A. (1905). Uber die von der molekularkinetischen Theorie der Warme geforderte Bewegung von in ruhenden Flssigkeiten suspendierten Teilchen. *Ann. Phys.*, *17*, 549.

Gavazzi, L., Nermut, M., & Marchisio, P. (1989). Ultrastructure and gold-immunolabelling of cell-substratum adhesions (podosomes) in RSV-transformed BHK cells. *J. Cell Sci.*, *94*, 85–99.

Geblinger, D., Addadi, L., & Geiger, B. (2010). Nano-topography sensing by osteo-

clasts. *J. Cell Sci.*, *123*, 1503–1510.

Gimona, M., Buccione, R., Courtneidge, S. A., & Linder, S. (2008). Assembly and biological role of podosomes and invadopodia. *Curr. Opin. Cell Biol.*, *20*, 235–241.

Gondran, C., & Michelson, D. (2006). Effect of probe tip size on atomic force microscopy roughness values for very smooth samples. *J. Vac. Sci. Technol. A*, *24*(4), 1185–1190.

Grano, M., Galimi, F., Zambonin, G., Colucci, S., Cottone, E., Zambonin Zallone, A., et al. (1996). Hepatocyte growth factor is a coupling factor for osteoclasts and osteoblasts *in vitro*. *Proc. Natl. Acad. Sci. USA*, *93*, 7644–7648.

Hatano, S., & Oosawa, F. (1966a). Extraction of an actin-like protein from the plasmodium of a myxomycete and its interaction with myosin A from rabbit striated muscle. *J. Cell Physiol.*, *68*, 197–202.

Hatano, S., & Oosawa, F. (1966b). Isolation and characterization of plasmodium actin. *Biochim. Biophys. Acta*, *127*, 488–498.

Hawley, T., & Hawley, R. (2004). *Methods in Molecular Biology, Vol.263, Flow Cytometry Protocols*. London: Humana Press. (2nd Ed.)

He, G., & George, A. (2004). Dentin matrix protein 1 immobilized on type I collagen fibrils facilitates apatite deposition in vitro. *J. Biol. Chem.*, *279*, 11649–11656.

Head, D., Levine, A., & MacKintosh, F. (2003). Deformation of cross-linked semiflexible polymer networks. *Phys. Rev. Lett.*, *91*, 108102.

Helfrich, M., Nesbitt, S., Lakkakorpi, P., Bames, M., Bodary, S., Shankar, G., et al. (1996). β1 integrins and osteodast function: involvement in collagen recognition and bone resorption. *Bone*, *19*, 317–328.

Heussinger, C., Schaefer, B., & Frey, E. (2007). Nonaffine rubber elasticity for stiff polymer networks. *Phys. Rev. E*, *76*, 031906.

Hofmann, W., & de Lanerolle, P. (2006). Nuclear actin: to polymerize or not to polymerize. *J. Cell Biol.*, *172*(4), 495–496.

Hu, S. (2007). *Influence of surface characterizations on the adhesion and proliferation properties of the endothelial cells*. Unpublished doctoral dissertation, East China Normal University. (62 p.)

Hu, S., Wang, X., Liu, E., Shi, Q., & Yu, W. (2008). The preparation of the topographed-TiO_2 films and the influence on the adhesion behavior of endothelial cells. *Journal of Functional Materials and Devices*, *14*(3), 597–602.

Huisman, E., van Dillen, T., Onck, P., & Van der Giessen, E. (2007). Three-dimensional cross-linked F-actin networks: relation between network architecture and mechanical behavior. *Phys. Rev. E*, *99*, 208103.

Huxley, H. (1973). Muscular contraction and cell motility. *Nature*, *243*, 445–449.

Ingber, D. (2006). Cellular mechanotransduction: putting all the pieces together again. *FASEB J.*, *20*, 811–827.

Inoue, S., & Sato, H. (1967). Cell motility by labile association of molecules. The nature of mitotic spindle fibers and their role in chromosome movement. *J. Gen. Physiol.*, *50*, 259–292.

Janmey, P., & McCulloch, C. (2007). Cell mechanics: Integrating cell responses to mechanical stimuli. *Annu. Rev. Biomed. Eng.*, *9*, 1–34.

Jurdic, P., Saltel, F., Chabadel, A., & Destaing, O. (2006). Podosome and sealing

zone: specificity of the osteoclast model. *Eur. J. Cell Biol.*, *83*(3–4), 195–202.

Kölliker, A. (1873). *Die Normale Resorption des Knochengewebes und ihre Bedeutung für die Entstehung der typischen Knochenformen.* Oxford Univ.: F.C.W. Vogel.

Kotadiya, P., McMichael, B., & Lee, B. (2008). High molecular weight tropomyosins regulate osteoclast cytoskeletal morphology. *Bone*, *43*, 951–960.

Kueh, H., & Mitchison, T. (2009). Structural plasticity in actin and tubulin polymer dynamics. *Science*, *325*, 960–963.

Kuhn, J., & Pollard, T. (2005). Real-time measurements of actin filament polymerization by total internal reflection fluorescence microscopy. *Biophys. J.*, *88*, 1387–1402.

Lakkakorpi, P., & Vaananen, H. (1991). Kinetics of the osteoclast cytoskeleton during the resorption cycle in vitro. *J. Bone Miner. Res.*, *6*, 817–826.

Lakkakorpi, P., & Vaananen, H. (1996). Cytoskeletal changes in osteoclasts during the resorption cycle. *Microsc. Res. Tech.*, *33*, 171–181.

Lane, N. (1969). Intranuclear fibrillar bodies in actinomycin D-treated oocytes. *J. Cell Biol.*, *40*, 286–291.

Lauffenburger, D., & Horwitz, A. (1996). Cell migration: a physically integrated molecular process. *Cell*, *84*, 359–369.

Li, K. (2008, February). *The image stabilizer plugin for ImageJ.* `http://www.kangli.org/page6.html`.

Li, Z., Kong, K., & Qi, W. (2006). Osteoclast and its roles in calcium metabolism and bone development and remodeling. *Biochem. Biophys. Res. Commun.*, *343*, 345–350.

Linder, S. (2007). The matrix corroded: podosomes and invadopodia in extracellular matrix degradation. *Trends in Cell Biology*, *17*, 107–117.

Linder, S. (2009). Invadosomes at a glance. *J. Cell Biol.*, *122*, 3009–3013.

Linder, S., & Aepfelbacher, M. (2003). Podosomes: adhesion hotspots of invasive cells. *Trends in Cell Biology*, *13*, 376–385.

Linder, S., & Kopp, P. (2005). Podosomes at a glance. *J. Cell Sci.*, *118*, 2079–2082.

Linder, S., Nelson, D., Weiss, M., & Aepfelbacher, M. (1999). Wiskott-Aldrich syndrome protein regulates podosomes in primary human macrophages. *Proc. Natl. Acad. Sci. USA*, *96*, 9648–9653.

Liu, A., Richmond, D., Maibaum, L., Pronk, S., Geissler, P., & Fletcher, D. (2008). Membrane-induced bundling of actin filaments. *Nat. Phys.*, *4*, 789–793.

Lodish, H. (2008). *Molecular cell biology.* New York: W.H. Freeman. (Vol. 6th)

Loitto, V., Forslund, T., Sundqvist, T., Magnusson, K., & Gustafsson, M. (2002). Neutrophil leukocyte motility requires directed water influx. *J. Leukoc. Biol.*, *71*, 212–222.

Luxenburg, C., Geblinger, D., Klein, E., Anderson, K., Hanein, D., Geiger, B., et al. (2007). The architecture of the adhesive apparatus of cultured osteoclasts: from podosome formation to sealing zone assembly. *PLoS ONE*, *2*(1), e179.

Makihira, S., Mine, Y., Kosaka, E., & Nikawa, H. (2007). Titanium surface roughness accelerates RANKL-dependent differentiation in the osteoclat precursor cell line, RAW264.7. *Dent. Mater. J.*, *26*(5), 739–745.

Marchisio, M., Di Carmine, M., Pagone, R., Piattelli, A., & Miscia, S. (2005). Implant surface roughness influences osteoclast proliferation and differentiation. *J.*

Biomed. Mater. Res. B, *75*(2), 251–256.

Marchisio, P., Bergui, L., Corbascio, G., Cremona, O., D'Urso, N., Schena, M., et al. (1988). Vinculin, talin, and integrins are localized at specific adhesion sites of malignant B lymphocytes. *Blood*, *72*, 830–833.

Marks, Jr., S., & Popoff, S. (1988). Bone cell biology: The regulation of development, structure, and function in the skeleton. *Am. J. Anatomy*, *183*, 1–44.

Miyamoto, T., & Suda, T. (2003). Differentiation and function of osteoclasts. *Keio J Med.*, *52*(1), 1–7.

Mulari, M., Vaaraniemi, J., & Vaananen, H. (2003). Intracellular membrane trafficking in bone resorbing osteoclasts. *Microsc. Res. Tech.*, *61*, 496–503.

Mulari, M., Zhao, H., Lakkakorpi, P., & Vaananen, H. (2003). Osteoclast ruffled border has distinct subdomains for secretion and degraded matrix uptake. *Traffic*, *4*, 113–125.

Nakamura, L., Pilkington, M., Lakkakorpi, P., Lipfert, L., Sims, S., Dixon, S., et al. (1999). Role of αvβ3 integrin in osteodast migration and formation of the sealing zone. *J. Cell Sci.*, *112*, 3985–3993.

Nesbitt, S., & Horton, M. (1997). Trafficking of matrix collagens through bone-resorbing osteoclasts. . *Science*, *276*, 266–269.

Nicholson-Dykstra, S., Higgs, H., & Harris, E. (2005). Actin dynamics: growth from dendritic branches . *Curr. Biol.*, *15*(9), R346–357.

Okamoto, K., Nishio, S., Saga, T., & Kobayashi, T. (2000). Standard images for particle-image velocimetry. *Meas. Sci. Technol.*, *11*, 685–691.

Oosawa, F., & Asakura, S. (1975). *Thermodynamics of the polymerization of proteins.* New York: Academic Press.

Pfaff, M., & Jurdic, P. (2001). Podosomes in osteoclast-like cells: structural analysis and cooperative roles of paxillin, proline-rich tyrosine kinase 2 (Pyk2) and integrin αVβ3. *J. Cell Sci.*, *114*(15), 2775–2786.

Pollard, T. (1986). Rate constants for the reactions of ATP- and ADP-actin with the ends of actin filaments. *J. Cell Biol.*, *103*, 2747–2754.

Pollard, T., Blanchoin, L., & Mullins, R. (2000). Molecular mechanisms controlling actin filament dynamics in nonmuscle cells. *Annu. Rev. Biophys. Biomol. Struct.*, *29*, 545–576.

Pollard, T., & Borisy, G. (2003). Cellular motility driven by assembly and disassembly of actin filaments. *Cell*, *112*, 453–465.

Pollard, T., & Earnshaw, W. (2004). *Cell Biology.* Philadelphia, PA: Saunders.

Pollard, T., & Weihing, R. (1974). Actin and myosin and cell movement. *CRC Crit. Rev. Biochem.*, *2*, 1–65.

Raffel, M., Willert, C., & Kompenhans, J. (1998). *Particle Image Velocimetry.* Springer, Berlin.

Roodman, G. (1999). Cell biology of the osteoclast. *Exp Hematol.*, *27*, 1229–1241.

Roodman, G. (2006). Regulation of osteoclast differentiation. *Ann N Y Acad Sci.*, *1068*, 100–109.

Salo, J., P., L., Mulari, M., Metsikko, K., & Vaananen, H. (1997). Removal of osteoclast bone resorption products by transcytosis. *Science*, *276*, 270– 273.

Saltel, F., Chabadel, A., Bonnelye, E., & Jurdic, P. (2008). Actin cytoskeletal organisation in osteoclasts: A model to decipher transmigration and matrix degradation.

Eur. J. Cell Biol., *87*(8–9), 459–468.

Saltel, F., Destaing, O., Bard, F., Eichert, D., & Jurdic, P. (2004). Apatite-mediated actin dynamics in resorbing osteoclasts. *Mol. Biol. Cell*, *15*, 5231–5241.

Schleicher, M., & Jockusch, B. (2008). Actin: its cumbersome pilgrimage through cellular compartments. *Histochem. Cell Biol.*, *129*, 695–704.

Schmoller, K., Lieleg, O., & Bausch, A. (2009). Structural and viscoelastic properties of actin/filamin networks: cross-linked versus bundled networks. *Biophys. J.*, *97*, 83–89.

Shevde, N., Bendiexen, A., Dienger, K., & Pike, J. (2000). Estrogens suppress RANK ligand-induced osteoclast differentiation via a stromal cell independent mechanism involving c-Jun repression. *Proc. Natl. Acad. Sci. USA*, *97*, 7829–7834.

Shin, J., Gardel, M., Mahadevan, L., Matsudaira, P., & Weitz, D. (2004). Relating microstructure to rheology of a bundled and cross-linked F-actin network in vitro. *Proc. Natl. Acad. Sci. USA*, *101*, 9636–9641.

Small, J. (1988). The actin cytoskeleton. *Electron Microsc. Rev.*, *1*, 155–174.

Small, J., Isenberg, G., & Celis, J. (1978). Polarity of actin at the leading edge of cultured cells. *Nature*, *272*, 638–639.

Small, J., Stradall, T., Vignal, E., & Rottner, K. (2002). The lamellipodium: where motility begins. *Trends in Cell Biology*, *12*(3), 112–120.

Stossel, T. (1993). On the crawling of living animals. *Science*, *260*, 1086–1094.

Taeyoon, K., Hwang, W., Lee, H., & Kamm, R. (2009). Computational analysis of viscoelastic properties of crosslinked actin networks. *PLoS Comput. Biol.*, *5*(7), e1000439.

Teitelbaum, S. (2000). Bone resorption by osteoclasts. *Science*, *289*, 1504–1508.

Tilney, L. (1975). The role of actin in nonmuscle cell motility. *Soc. Gen. Physiol. Ser.*, *30*, 339–388.

Trepat, X., Lenormand, G., & Fredberg, J. (2008). Universality in cell mechanics. *Soft Matter*, *4*, 1750–1759.

Vaananen, H., Zhao, H., Mulari, M., & Halleen, J. (2000). The cell biology of osteoclast function. *J. Cell Sci.*, *113*, 377–381.

Visegrady, B., Lorinczy, D., Hild, G., Somogyi, B., & Nyitrai, M. (2005). A simple model for the cooperative stabilisation of actin filaments by phalloidin and jasplakinolide. *FEBS Lett.*, *579*, 6–10.

Wagner, B., Tharmann, R., Haase, I., Fischer, M., & Bausch, A. R. (2006). Cytoskeletal polymer networks: molecular structure of crosslinkers determine macroscopic properties. *Proc. Natl. Acad. Sci. USA*, *103*, 13974–13978.

Walsh, M., Kim, N., Kadono, Y., Rho, J., Lee, S., Lorenzo, J., et al. (2006). Osteoimmunology: interplay between the immune system and bone metabolism. *Annu. Rev. Immunol.*, *24*, 33–63.

Wang, S., Arellano-Santoyo, H., Combs, P., & Shaevitz, J. (2010). Actin-like cytoskeleton filaments contribute to cell mechanics in bacteria. *Proc. Natl. Acad. Sci. USA*, *107*(20), 9182–9185.

Wang, Y. (1985). Exchange of actin subunits at the leading edge of living fibroblasts: possible role of treadmilling. *J. Cell Biol.*, *101*, 597–602.

Wang, Y., & Pelham, R. (1998). Preparation of a flexible, porous polyacrylamide substrate for mechanical studies of cultured cells. *Methods Enzymol.*, *298*, 486–

496.

Wang, Z., Myles, G., Brandt, C., Lioubin, M., & Rohrschneider, L. (1993). Identification of the ligand-binding regions in the macrophage colony-stimulating factor receptor extracellular domain. *Mol. Cell. Biol.*, *13*, 5348–5359.

Wilhelm, J., & Frey, E. (2003). Elasticity of stiff polymer networks. *Phys. Rev. Lett.*, *91*, 108103.

Wright, H., McCarthy, H., Middleton, J., & Marshall, M. (2009). RANK, RANKL and osteoprotegerin in bone biology and disease. *Curr. Rev. Musculoskelet. Med.*, *2*, 56–64.

Yang, C., Hoelze, M., Disanza, A., Scita, G., & Svitkina, T. (2009). Coordination of membrane and actin cytoskeleton dynamics during filopodia protrusion. *PLoS ONE*, *4*(5), e5678.

Zambonin-Zallone, A., Teti, A., Gaboli, M., & Marchisio, P. (1989). β 3 subunit of vitronectin receptor is present in osteoclast adhesion structures and not in other monocyte-macrophage derived cells. *Connect Tissue Res.*, *20*, 143–149.

Zamir, E., & Geiger, B. (2001). Molecular complexity and dynamics of cellmatrix adhesions. *J. Cell Sci.*, *114*, 3583–3590.

Zhu, J., & Carlsson, A. (2010). Effects of molecular-scale processes on observable growth properties of actin networks. *Phys. Rev. E*, *81*, 031914.

Appendix A

Complementary experiments

In chapter 2, we demonstrated that the podosome organization does not depend on the chemical properties of the substrate. It has been previously pointed out, in the literature, that some biological processes are sensitive to surface topography – in particular, osteoclasts differentiation (M. Marchisio et al., 2005; Makihira et al., 2007) or the formation and stability of the sealing zone (Geblinger et al., 2010). In order to check if the substrate topography has an influence on the podosomes organization, we performed the following series of complementary experiments. We used three different types of substrate: a rough glass substrate (section A.1), a silicon substrate with 5 to 50 μm patterns (section A.2) and a zirconium oxide substrate with a 0.3 μm (section A.3).

A.1 Rough glass substrate

We first observe the mature osteoclasts on hard substrates of different roughness. The osteoclasts were differentiated during 6 days, then seeded on the different substrates (section 2.1.3). After 4 hours incubation, they are fixed and stained by Phalloidin Alexa 488 (section 2.1.4), and observed by fluorescence microscopy (section subsec:microscopy). We use three different kinds of substrates:

- Low roughness glass: the rough part of a commercial glass slide.

- High roughness glass: produced in our laboratory by sand blast on a commercial glass slide.

- Control: normal smooth glass slide.

In order to quantify the roughness of the substrates, we scan the surfaces with an atomic force microscope (AFM)[1]. The AFM images of the low and high roughness glasses are displayed in figures A.1 a and A.1 b, respectively.

Green fluorescence images (actin) and Nomarski differential interference contrast optics images are acquired with 40x object in Axioplan 2 Imaging fluorescence microscope (Zeiss) (figure A.2). The observations indicate that podosomes organization does not seem to depend on the substrate roughness. Indeed, the podosomes organize in belt on the low roughness and high roughness glass substrates, in a similar way than on the control smooth glass substrate.

It is difficult, however, to bring out a clear conclusion from this experiment. In particular, we do not know how accurate is the roughness measurement by AFM. Surface sand blasting can create very abrupt and precipitous surfaces. The AFM tip might not be able to measure such sharp structures (Gondran & Michelson, 2006). Unfortunately, we could not repeat the experiments. Indeed, due to the rigidity of the substrate, and its steep topography, the AFM tip breaks easily.

[1]The AFM experiments were performed at the Laboratoire de Physique de la Matière Condensée et Nanostructures (LPMCN), Université Lyon 1.

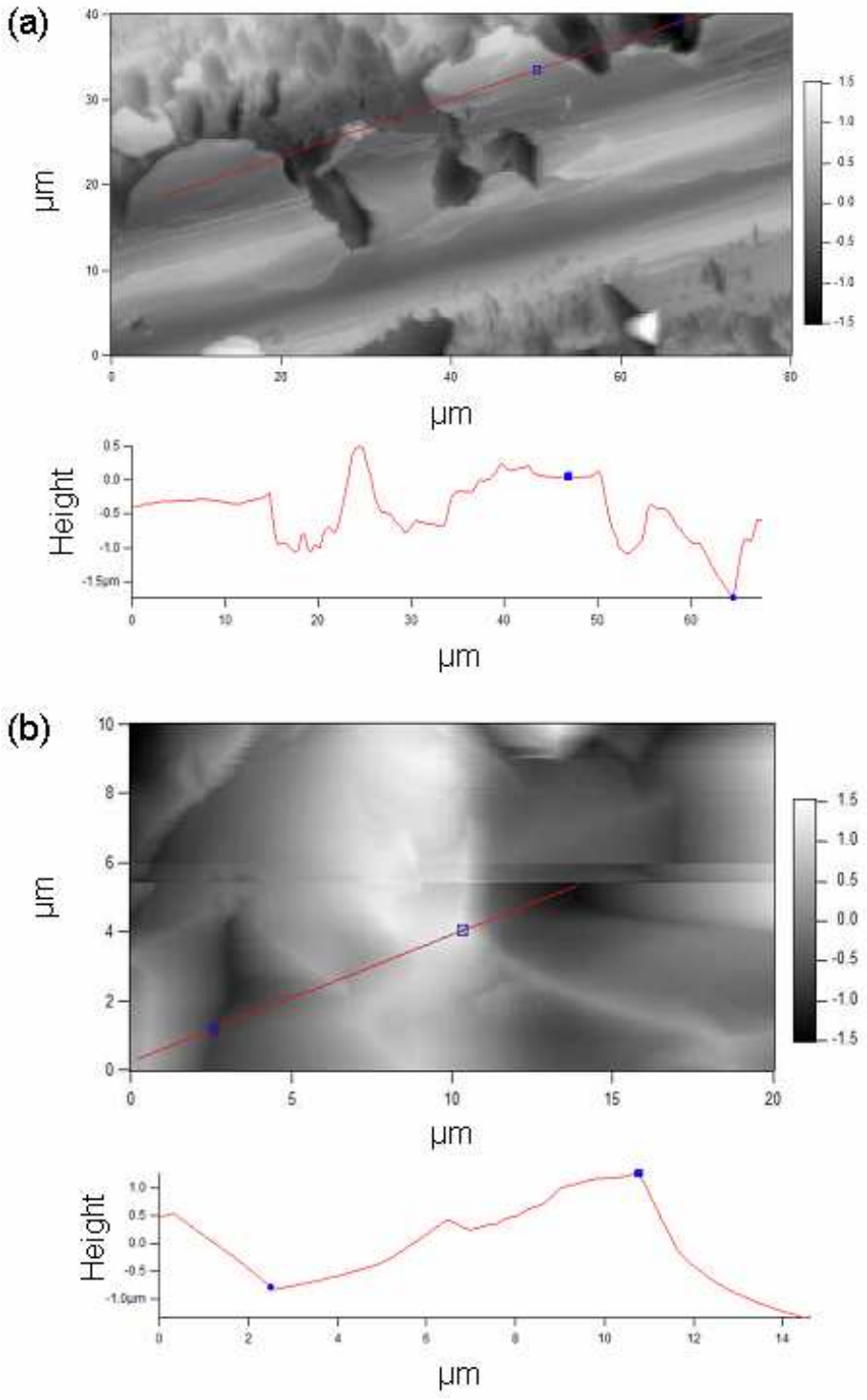

Figure A.1: Substrate roughness measured by AFM for (a) the low roughness and (b) the high roughness glass substratre. *Top images*: map of the surface topography. Grey scale bar is in microns. *Bottom images*: examples of roughness variations along the red profiles indicated in the above images. The blue dots reported on the red profile point out a high and low topography.

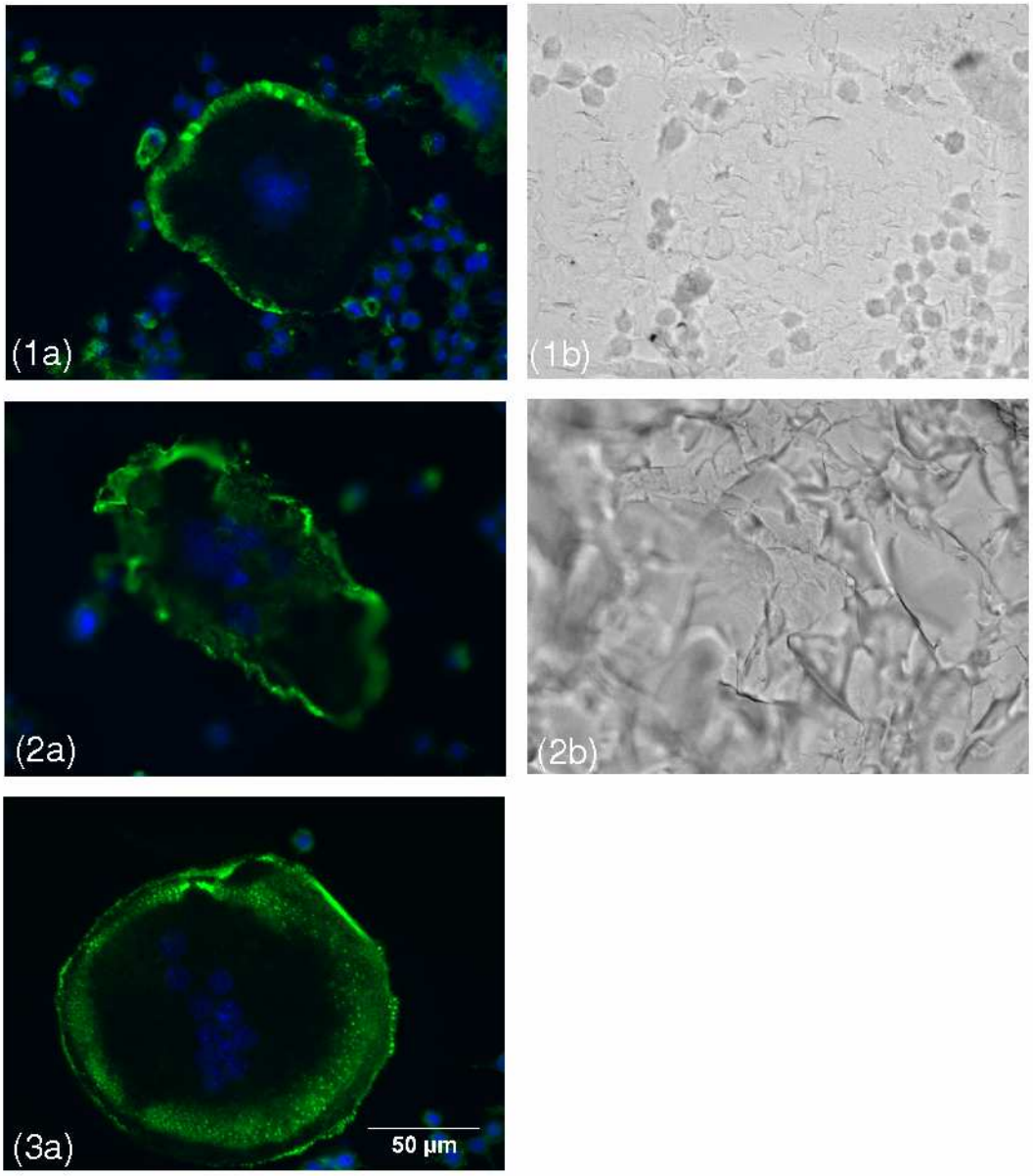

Figure A.2: Osteoclasts on different glass roughness. (1a), (2a) and (3a) are the fluorescence images of actin on the low roughness glass, high roughness glass, and control smooth glass, respectively. The Nomarski differential interference contrast optics images in (1b) and (2b) give a rough idea of the topography corresponding to (1a) and (2a), respectively. The scale bar (50 μm) is the same for all the images.

A.2 Micron-patterned silicon substrate

In the previous experiment, we were not able to control or measure precisely the substrate roughness. In order to perform more accurate investigations, we did the same experiments on patterned substrates.

The patterned surfaces were microfabricated on a silicon wafer[2] by using successively photolithography and reactive ion etching (RIE) methods[3]. Photolithography and RIE methods are commonly used in microfabrication to selectively remove parts of a substrate. We detail these methods in the following sections. We produced six types of patterned surface, with a square pattern size of 10 μm, 20 μm or 50 μm. The pattern can be either a positive (bumps) or negative (holes) topography. The distance between the square patterns (bumps or holes) is constant, and equal to 10 μm.

A.2.1 Photolithography method

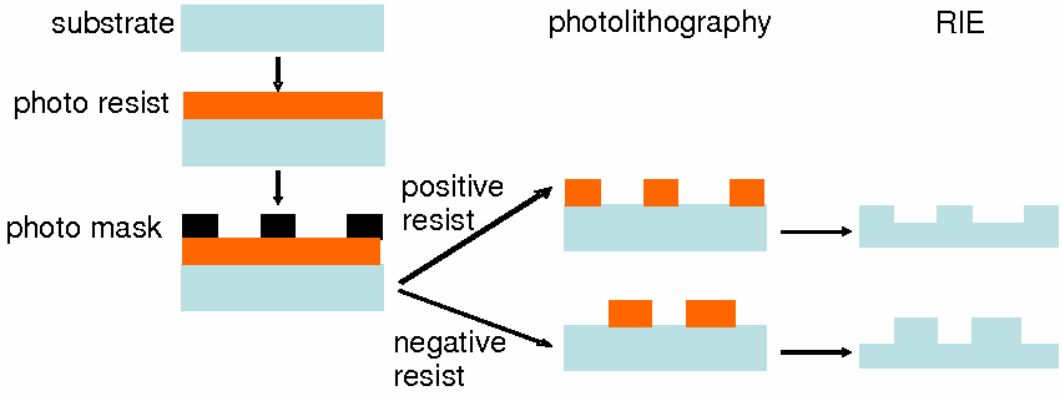

Figure A.3: Sketch of surface pattern microfabrication. The silicon wafer is coated with a photo resist layer, then put under an ultraviolet light to transfer a pattern from a photo mask to the photo resist. Positive or negative photo resists can generate negative or positive topography, respectively (see text). Then with RIE methods, the patterns are transfered from the photo resist onto the silicon substrate.

Photolithography consists in transfering, by exposion to an ultraviolet light, a geometric pattern from a photo mask to a light-sensitive chemical photo resist, initially deposited on the substrate. Successive chemical applications make it possible to transfer the pattern to the substrate underneath. Two types of photo resist can be applied: positive photo resist, soluble in the chemical developer, creates a negative topography; whereas negative photo resist, insoluble in the developer, creates a positive topography (figure A.3). By using designed photo masks (coated cadmium on a glass surface with

[2]Silicon wafer n type, electrical resistance $4 \sim 8$ Ω.cm, purchased at Xiang Jing Shanghai Electronic Technology Co., Ltd.

[3]The micron-patterned sufaces were produced at East China Normal University, Shanghai.

square patterns 10×10 μm, 20×20 μm or 50×50 μm), we followed the protocol described in Hu (2007); Hu et al. (2008). For each pattern size, we produced both a positive and negative topography onto the photo resist layer (figure A.3). We then applied the following RIE method, to transfer the patterns from the photo resist onto the silicon substrate.

A.2.2 RIE method

Reactive ion etching (RIE) is a process to use chemically reactive plasma to remove material deposited on a substrate. The plasma is generated under low pressure (vacuum) by an electromagnetic field. High-energy ions from the plasma attack the substrate surface and react with it. We used the gas SF_6 to create a plasma (F) which sublimates the exposed silicon surface (not protected by the photo resist) into SiF_4. The reaction equations are the following:

$$SF_6 + e \longrightarrow SF_5 + 2F + 2e \quad (A.1)$$

$$Si + 4F \longrightarrow SiF_4 \quad (A.2)$$

All the silicon substrates were etched by the plasma (F) for 4 minutes. The etching speed is around 1.3 μm/min, so the pattern depth is around 5μm. We then removed the photo resist from the micron-patterned silicon substrate by using an oxygen plasma which oxidizes it. The detailed procotol of the RIE method can be found in Hu (2007).

A.2.3 Results

The fluorescence images, acquired with a 63x objective in the Axioplan 2 Imaging fluorescence microscope (Zeiss), are displayed in figure A.4. The osteoclasts present podosomes on all the patterned surfaces. However, we observe that the shape of the osteoclast is strongly related to the pattern. On the one hand, osteoclasts try to avoid the small size bumps and spread on the surface between the bumps (figures A.4 a and b); for large size bumps (50 μm), most osteoclasts (in particular, the larger ones) stay on the bumps (figure A.4 c). On the other hand, osteoclasts ignore the small holes and step over them (figures A.4 d and f); for the large size holes (50 μm), the osteoclasts get trapped inside the hole. We will discuss these observation in section A.4.

For all the patterned substrates, we do not observe a clear difference between the podosome organization. The images reported in figure A.4 show that the podosomes are more or less homogeneously spreading over the osteoclast. It is interesting to note, however, that in the case where the osteoclasts avoid the substrate patterns, the podosomes are more concentrated around the pattern boundary (figures A.4 a, A.4 b, A.4 c, A.4 d).

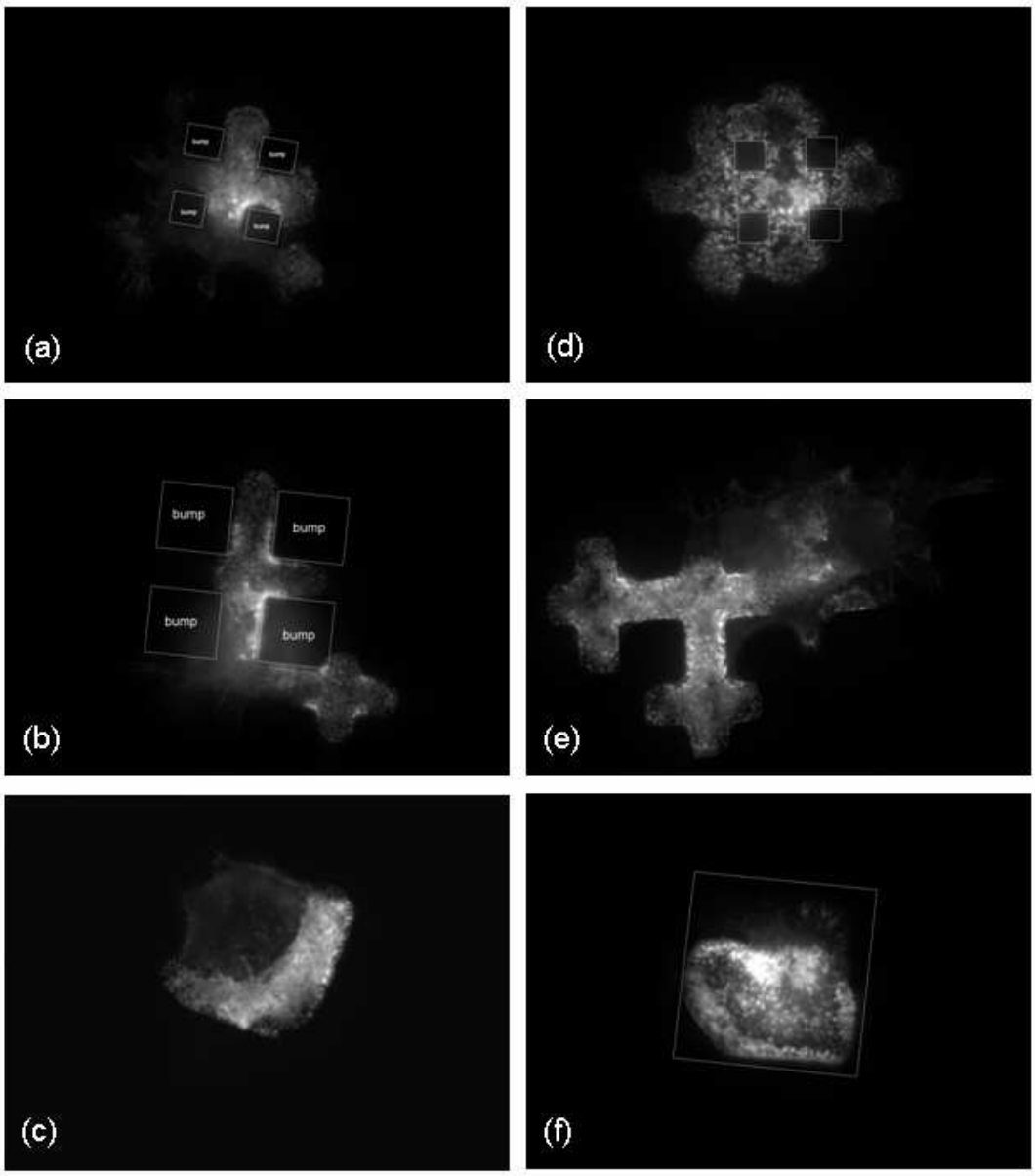

Figure A.4: Osteoclasts on the micron-patterned silicon substrates. Actin is stained by Phalloidin to be visible in the fluorescence images. (a): 10 μm square bump; (b): 20 μm square bump; (c): 50 μm square bump; (d): 10 μm square hole; (e): 20 μm square hole; (f): 50 μm square hole. All patterns are separated by a constant distance of 10 μm.

A.3 Submicron-patterned ZrO_2 substrate

In a last experiment, we investigated the effect of a patterned substrate when the pattern size is of the order of the size of a podosome (~ 0.5 μm). To this purpose, we used a submicron-patterned zirconium oxide substrate (ZrO_2). This type of substrate, made from fine powder aggregation, presents a characteristic topographic size of 0.3 μm[4]. Note that in this case, the substrate surface does not present a sharp topography, but rather looks like a paving composed of half spheres.

The experimental conditions and visualization techniques are the same than in the above sections. The fluorescence image of an osteoclast on the submicron-patterned ZrO_2 substrate is displayed in figure A.5. The podosomes seem to ignore the underlying pattern. In this particular case, we observe a belt organization.

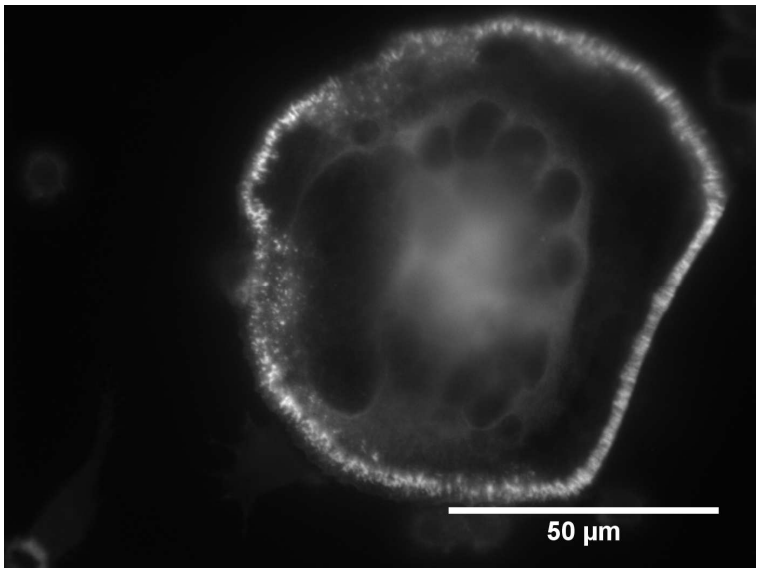

Figure A.5: Osteoclasts on the submicron-patterned ZrO_2 substrate (typical pattern length of 0.3 μm). Actin is stained by Phalloidin to be visible in the fluorescence image. We observe a belt organization. Note that the submicron-pattern is too small to be visible on the fluorescence image.

A.4 Discussion

The series of experiments presented above show that the podosomes presence and organization in an osteoclast does not seem to depend on the surface topography. They are not affected by the change of surface physical properties, in a similar way than the results we found for the change of chemical surface properties (chapter 2).

[4]These substrates were kindly provided by L. Gremillard, from MATEIS laboratory (Matériaux : Ingénierie et Science) at INSA (Institut National des Sciences Appliquées), Lyon.

The osteoclast morphology, however, strongly depends on the shape and size of the pattern. From the images presented in figure A.4, we infer that the osteoclasts prefer to spread over a flat surface. If the characteristic pattern size is too small ($\leq$20 μm), they avoid the pattern and spread on the space in-between, regardless of the nature of the topography (bumps or holes). If the characteristic pattern size is large enough ($\geq$50 μm), the osteoclasts stand on the flat part of the pattern itself (upon a bump or inside a hole). This higher podosomes concentration along the bump boundaries could reflect the bending of actin filaments and the subsequent pushing against the obstacle, as proposed in a theoretical model (Zhu & Carlsson, 2010). We are not able to explain, at this time, the slightly higher podosomes concentration along the hole boundaries.

These experiments are preliminary results, and the features described above should be further investigated. For instance, it would be interesting to study the effect of the pattern height or depth, or the size of the space separating the patterns, on the osteoclast spreading. Finally, these experiments were performed with fixed cells; analysing the osteoclast motility on such substrates for live cells could bring new informations on podosomes dynamics.

Abstract

Osteoclasts are large, multinucleated cells, which resorb mineralized bone. When an osteoclast encounters a substrate, dot-like actin-rich structures, the podosomes, appear and assemble into clusters, rings or a belt. We experimentally investigate, from a cell population to a single podosome, their function and dynamics. Over a cell population, kinetic measurements show that the cell surface area A scales as $A \sim K^2$, where K is the number of nuclei, indicating a flat morphology. By defining quantities that account for the spatial distribution of the actin within the cell, we demonstrate that the podosomes organization only depends on the time after differentiation, and not on K. In a single osteoclast, the observation of a strong coupling between cell spreading and podosomes formation lead us to propose that podosomes play an important role in osteoclast motility. Analysis of osteoclast migration, and the forces it applies on the substrate, demonstrates that the internal dynamics of the actin within the cell does not only correlate with cell migration, but drives it. Finally, in order to understand the internal dynamics of a single podosome, we improved the model of Biben et al. (2005) by considering on the one hand, actin polymerization, and on the other hand, diffusion and attachment kinetics of the gelsolin, an actin severing protein. We find that podosomes are mainly governed by the actin dynamics, regardless of gelsolin concentration.

Resumé

Les ostéoclastes sont des cellules multinucléées, responsables de la résorption osseuse. Quand ils sont déposés sur un substrat, des structures ponctuelles riches en actine, les podosomes, apparaissent et s'assemblent en clusters, anneaux ou ceinture. Nous avons étudié expérimentalement leur fonction et leur dynamique, depuis une population entière jusqu'à l'échelle d'un unique podosome. Sur une population de cellules, des mesures cinétiques montrent que la surface de la cellule A varie comme $A \sim K^2$, où K est le nombre de noyaux ; ce résultat indique une forme aplatie. Par ailleurs, la mesure de quantités qui prennent en compte l'organisation spatiale de l'actine dans la cellule montre que l'organisation des podosomes ne dépend que du temps écoulé après différentiation, et non de K. Dans un seul ostéoclaste, l'observation d'un fort couplage entre l'étalement d'une cellule et la formation des podosomes nous a conduit à suggérer que les podosomes jouent un rôle important dans la mobilité des ostéoclastes. L'analyse de la migration d'ostéoclastes, ainsi que des forces appliquées sur le substrat, montre que la dynamique interne de l'actine dans la cellule est non seulement corrélée avec la migration cellulaire, mais la gouverne. Enfin, afin de comprendre la dynamique interne d'un podosome, nous avons amélioré le modèle de Biben et al. (2005), en prenant en compte d'une part, la polymérisation de l'actine, et d'autre part, la diffusion et la cinétique d'attachement de la gelsoline, une protéine responsable de la coupe des filaments d'actine. Nous montrons que les podosomes sont principalement gouvernés par la dynamique de l'actine, indépendamment de la concentration en gelsoline.